

Revealing Planet Formation: Technique, Observation, and Analysis

by

Michael Patrick Fitzgerald

BS (California Institute of Technology) June, 2000

MA (University of California, Berkeley) Dec, 2002

A dissertation submitted in partial satisfaction of the
requirements for the degree of

Doctor of Philosophy

in

Astrophysics

in the

GRADUATE DIVISION

of the

UNIVERSITY OF CALIFORNIA, BERKELEY

Committee in charge:

Professor James R. Graham, Chair

Professor Geoffrey W. Marcy

Professor Reinhard Genzel

Fall 2007

The dissertation of Michael Patrick Fitzgerald is approved:

Chair Date

Date

Date

University of California, Berkeley

Fall 2007

Revealing Planet Formation: Technique, Observation, and Analysis

Copyright 2007

by

Michael Patrick Fitzgerald

Abstract

Revealing Planet Formation: Technique, Observation, and Analysis

by

Michael Patrick Fitzgerald

Doctor of Philosophy in Astrophysics

University of California, Berkeley

Professor James R. Graham, Chair

Our understanding of planet formation rests on the observation of planetary systems over their lifetimes. The majority of known extrasolar planets are expected to have formed through a process of core accretion, by which solid planetesimals grow into embryos which sweep up gas in circumstellar disks. Observations of circumstellar disks provide a window into these processes. In particular, dusty debris produced by the destruction of primitive planetesimals can trace the characteristics and spatial distribution of these planetesimals, as well as test for the presence of planets. Debris disks are faint relative to their host stars, and advanced techniques are required to directly image the light scattered by the dust. I examine some of the challenges to high-contrast observations of circumstellar debris disks. I investigate the formation and statistics of stellar “speckles” in adaptively corrected images, which constitute a limiting noise source in high-contrast imaging. The ability for adaptive optics coronagraphy to image debris disks is examined in the context of understanding the processes of planet formation. I present an investigation using adaptive optics coronagraphy of the debris disk around AU Microscopii, a young low-mass star whose disk can be directly compared with that of the archetypal β Pictoris. I also present the discovery of a ring of warm dust around HD 32297, investigate the range of disk architectures allowed by my observations, and probe the processes responsible for the distribution of dust around this star.

PUT YOUR DEDICATION HERE

Contents

List of Figures	iv
List of Tables	v
Acknowledgments	vi
1 Introduction	1
2 The Challenge of High-Contrast Imaging	5
2.1 Limitations to Contrast	6
2.1.1 Diffraction and Image Formation	6
2.1.2 Limitations with a Stable PSF	11
2.1.3 Instrumental Limitations	11
2.1.4 Atmospheric Limitations	12
2.1.5 Point Sources and Extended Emission	15
2.2 Coronagraphy	17
2.3 The Promise of Adaptive Optics	20
3 Statistics of Adaptively Corrected Speckles	23
3.1 Introduction	23
3.2 Probabilistic Description of Intensity	25
3.2.1 Intensity in the Image Plane	25
3.2.2 The Distribution of Intensity	27
3.3 Observations	28
3.3.1 Measurements and Data Processing	28
3.3.2 Temporal Characteristics	30
3.4 Analysis	34
3.4.1 Testing the Distribution	34
3.4.2 Coherent PSF Extraction	38
3.5 Conclusions	40

4	Circumstellar Debris Disks	41
4.1	Debris Disk Architectures	42
4.2	Observations of Debris Disks	49
4.2.1	Unresolved Imaging	49
4.2.2	Scattered Light Imaging	51
4.2.3	Thermal Imaging	53
4.2.4	The Need for Multiple Wavelengths	53
4.3	Adaptive Optics Coronagraphy for Circumstellar Debris	57
5	The AU Microscopii Debris Disk	62
5.1	Introduction	62
5.2	Observations & Reduction	66
5.2.1	Near Infrared Imaging	66
5.2.2	PSF Subtraction Technique	68
5.2.3	Calibration	73
5.2.4	HST Imaging	76
5.3	Results	77
5.3.1	Disk Morphology	77
5.3.2	Surface Brightness Profiles	81
5.3.3	Disk Color Variation	84
5.3.4	Disk Substructure	86
5.3.5	Point Source Detection Sensitivity	92
5.4	Analysis	95
5.4.1	Dust Modeling	96
5.4.2	Birth Ring Examination	106
5.5	Discussion & Conclusions	113
6	A Ring of Warm Dust in the HD 32297 Debris Disk	119
6.1	Introduction	119
6.2	Observations	120
6.3	Results & Analysis	121
6.3.1	Stellar Properties	121
6.3.2	PSF Subtraction	125
6.3.3	Modeling	127
6.4	Discussion	136
6.4.1	Grain Dynamics	137
6.4.2	Conclusions	140
	Bibliography	141

List of Figures

2.1	Imaging system	9
2.2	Geometry of Lyot coronagraph.	18
3.1	Speckle intensity time series	31
3.2	Speckle autocovariance sequences	33
3.3	Best-fit intensity distributions	35
3.4	PSF decomposition	39
5.1	Roll subtraction process	69
5.2	Roll subtraction comparison	74
5.3	AU Mic images	78
5.4	AU Mic composite image	79
5.5	Vertical structure in the AU Mic disk	80
5.6	AU Mic midplane surface brightness profiles	82
5.7	AU Mic midplane colors	87
5.8	AU Mic substructure	88
5.9	AU Mic substructure profiles	89
5.10	AU Mic point source detection sensitivity	93
5.11	AU Mic model fit (V , H bands, SED)	103
5.12	AU Mic model fit (J , K' bands, polarization)	104
6.1	HD 32297 image	122
6.2	HD 32297 SED	123
6.3	PSF-subtracted images of HD 32297	126
6.4	Model parameter marginal posterior distributions	134

List of Tables

3.1	Hypothesis Test Results	37
4.1	Debris disks resolved in scattered light by space-based coronagraphs.	52
4.2	Debris disks resolved in scattered light by adaptive optics coronagraphs.	52
4.3	Debris disks resolved in thermal emission.	54
5.1	Observations of AU Mic	67
5.2	Midplane Surface Brightness Power-Law Indices	85
5.3	Comparison of Disk Features	91
5.4	Best-Fit Model Parameters	101
5.5	Best-Fit Model Avg. Scattering Parameters	102
6.1	Best-Fit Model Parameters	132

Acknowledgments

People helped me.

Chapter 1

Introduction

The dominant mechanism for planets that have been discovered to date is the growth of solid material into cores that accrete gas in a circumstellar disk (Ida & Lin 2005). The detailed mechanisms by which these processes occur are current subjects of theoretical and observational scrutiny. The expansion of the number of indirectly detected extrasolar planets in the past decade (Marcy et al. 2005) has framed debates over the processes governing the growth of solids into cores and the interaction between these larger bodies and the remaining circumstellar material.

There are many observational avenues for investigating planets and their formation. Focusing on their likely birth sites, optically thick gas and dust disks around pre-main-sequence stars, is one course. Though images are rare, it is also rewarding to study the tenuous, gas-poor dust disks around stars on the main sequence — the archetypal example being β Pictoris. In these systems, removal mechanisms ensure that small grains in these optically thin disks are removed on timescales shorter than the stellar age (i.e. $\lesssim 10$ Myr). Such grains are not primordial; rather, the debris is replenished by the collisional attrition of larger bodies or ejection from sublimating comets — processes responsible for the dust populations in the Solar System. The key points are: (1) these fresh grains trace an underlying population of primitive planetesimals, which encode the coagulation history of planets' solids; (2) the grains and the parent bodies reveal gravitational signatures of unseen planets; and (3) young stars with debris disks are attractive targets for directly detecting young

jupiters. In the larger sense, debris disks around young stars bridge the gap between protoplanetary disks and mature systems like our own, and thus signify a transitional phase in the evolution of circumstellar material (Backman & Paresce 1993; Zuckerman 2001; Meyer et al. 2007).

Addressing fundamental questions in planet formation requires characterization of debris disks architectures at high spatial resolution. These observations are challenging, as they must be made in the face of a large contrast between the starlight and the light scattered by the dust grains. The observations of disk structure can be used to infer the nature and distribution of planetesimals and planets, as well as the dynamical processes responsible for disk structures and evolution. I will review the foundations of imaging at high contrast in Chapter 2.

Such imaging observations are generally affected by a fluctuating background of speckles, a particular problem when detecting faint circumstellar material at small angular separations. These speckles can be created by both short-lived atmospheric aberrations and slowly changing distortions in the optical system. Over the course of a long-exposure image, the combination of many realizations of speckle patterns forms a halo in the point spread function (PSF) of characteristic angular scale $\Delta\theta \sim \lambda/r_0$ (where r_0 is the length scale of electromagnetic waves' spatial coherence in the pupil). While adaptive optics can increase the achievable image contrast, speckle noise remains a major source of random error, which decreases the sensitivity of observations near the angular diffraction limit, with scale of order λ/D (where D is the telescope diameter).

In Chapter 3, I investigate the behavior of the speckle intensity distribution in the image plane when using an adaptive optics system. This distribution is fundamental for understanding the noise limits affecting high-contrast observations. I show, for various locations in the image plane, that the observed distribution of speckle intensities is consistent with its predicted form. Additionally, I demonstrate a method by which the PSF of the telescope free of random atmospheric aberrations can be mapped over the image plane. This method can be used for PSF calibration and reconstruction.

While Chapters 2 and 3 concentrate on the processes affecting the limits to

imaging faint circumstellar material, high-contrast observations are one thrust in the larger context of investigation into debris disks and planet formation. Chapter 4 will give an overview of debris disk science, with a review of the physical processes affecting the distribution of dust grains in debris disks. I present a brief review of debris disk imaging in the available literature, and examine how adaptive optics coronagraphy can impact debris disk science. The need for observations at multiple wavelengths is discussed, as is the value of resolved imaging of the disks in both scattered light and thermal emission.

In Chapter 5, I present a detailed investigation into the debris disk around AU Microscopii (GJ 803) using adaptive optics coronagraphy. AU Mic is a compelling object to study in the context of disk evolution across different spectral types, as it is an M dwarf whose near edge-on disk may be directly compared to that of its A5V sibling β Pic. I resolve the disk from 8–60 AU in the near-IR JHK' bands at high resolution with the Keck II telescope and adaptive optics, and develop a novel data reduction technique for the removal of the stellar PSF. I measure a blue color across the near-IR bands, and confirm the presence of substructure in the inner disk. Some of the structural features exhibit wavelength-dependent positions. The disk architecture and characteristics of grain composition are inferred through modeling. The model confirms that the large-scale architecture of the disk is consistent with detailed models of steady-state grain dynamics. Here, a belt of parent bodies from 35–40 AU is responsible for producing dust that is then swept outward by the stellar wind and radiation pressures. I infer the presence of very small grains in the outer region, down to sizes of $\sim 0.05 \mu\text{m}$. These sizes are consistent with stellar mass-loss rates $\dot{M}_* \ll 10^2 \dot{M}_\odot$.

I report the detection of a ring of warm dust in the edge-on disk surrounding HD 32297 with the Gemini-N/MICHELLE mid-infrared imager in Chapter 6. The N' -band image shows elongated structure consistent with the orientation of the previously detected scattered-light disk. The measured flux is significantly above that arising from the stellar photosphere. Subtraction of the stellar PSF reveals a bilobed structure with peaks $0''.5$ – $0''.6$ from the star. I fit three-dimensional, single-size grain models of an optically thin dust ring to our image and the SED using a Markov

chain Monte Carlo algorithm in a Bayesian framework. The best-fit effective grain sizes are submicron, suggesting the same dust population is responsible for the bulk of the scattered light. Although the interpretation of the system is uncertain due to the unknown stellar age, previous indirect estimates (~ 30 Myr) indicate the dust is composed of debris. The peak vertical optical depths in the models ($\sim 0.3\text{--}1 \times 10^{-2}$) imply that grain-grain collisions likely play a significant role in dust dynamics and evolution. Submicron grains can survive radiation pressure blow-out if they are icy and porous. Similarly, the inferred warm temperatures (130–200 K) suggest that ice sublimation may play a role in truncating the inner disk.

Chapter 2

The Challenge of High-Contrast Imaging

In the optical and near infrared, planets and circumstellar debris are very faint relative to their parent stars. The challenge to imaging such circumstellar material stems from the fact that images of stars do not resemble points of light; rather, diffraction from the telescope and aberrations in the electromagnetic wavefronts from these systems smear out the starlight. In uncompensated imaging from the ground, the long-exposure image of the star forms a “seeing disk” with angular scale of $\sim 1''$. If one were to view the Solar System from a distance of 10 pc, a $0''.5$ separation from the star corresponds to Jupiter’s orbit, while the Kuiper Belt (and its associated dust disk) are at $\sim 4''$ separation (~ 40 AU). At a given brightness, it is generally easier to detect planets and dust belts in the outermost reaches of nearby stellar systems where the angular separation from the star is greatest. The brightest planets we hope to image are 10^7 – 10^9 times fainter than the star. While the total fraction of starlight scattered by dust disks can be brighter ($\lesssim 10^{-3}$ of the starlight), the light from such disks tends to be distributed over a larger area on the sky. It is the goal of this section to describe some of the detailed processes limiting our ability to detect circumstellar material, and to give an overview of technological solutions to increasing the achievable contrast for the study of planet formation.

2.1 Limitations to Contrast

2.1.1 Diffraction and Image Formation

A camera on an astronomical telescope constitutes an imaging system, and the process of image formation is governed by the diffraction of the incoming wave. The phenomena associated with astronomical imaging can generally be described within the framework of Fourier Optics [e.g. Goodman (2005), Mansuripur (2002) Chap. 2, Born & Wolf (1999) Chap. 8]. Fourier principles are applicable to astronomical cameras because the images are formed in the Fraunhofer diffraction regime. There is a Fourier relationship between the transverse electric field in the exit pupil of the imaging system (hereafter “pupil plane”), $\Psi_1(\mathbf{u})$, to the resulting field in the image plane, $\Psi_2(\mathbf{x})$. In an astronomical camera, the detector is placed at the image plane.

There are a few assumptions on which this framework rests. (I refer the reader to Goodman 2005 for a more complete treatment of the key points presented in this section.) The light propagating through the system consists of electromagnetic waves. The polarization state is ignored, and the electric field is treated as a scalar. This scalar diffraction theory is valid as long as the optical elements are large compared to the wavelength of light, which ensures negligible coupling between electric field components in the wave equation. In a given plane, the “field” denotes the amplitude and phase of the rapidly oscillating electric field. Here, $\Psi_{1,2}$ are complex phasors describing this quantity as a function of position. Finally, we require that Ψ_2 lie in the “far field” of the diffracting aperture. While diffraction from an aperture typically requires large distances to reach the far-field Fraunhofer regime (e.g. $> 2D^2/\lambda$, where D is the aperture diameter), the optics of the imaging system place the far-field pattern arising from the pupil at the image plane.

The two-dimensional Fourier transform is fundamental to our discussion. It is defined here as

$$g(\nu_x, \nu_y) = \iint_{-\infty}^{\infty} f(x, y) \exp[-2\pi i(x\nu_x + y\nu_y)] dx dy, \quad (2.1)$$

$$= \mathcal{F}[f(x, y)]_{\nu_x, \nu_y}. \quad (2.2)$$

The inverse transform is

$$f(x, y) = \iint_{-\infty}^{\infty} g(\nu_x, \nu_y) \exp [2\pi i(x\nu_x + y\nu_y)] d\nu_x d\nu_y, \quad (2.3)$$

$$= \mathcal{F}^{-1} [g(\nu_x, \nu_y)]_{\nu_x, \nu_y}. \quad (2.4)$$

Here, ν_x and ν_y are spatial frequencies, in units of length^{-1} . With these definitions, the normalizing constants for both transforms is simply unity.

For the case of an unresolved source (like most main-sequence stars in single-aperture optical/IR telescopes), the amplitude of the field in the image plane is given by the Fraunhofer diffraction pattern of the pupil plane field. The amplitude in the image plane is simply related to the Fourier transform of the amplitude in the pupil plane,

$$\Psi_2(\mathbf{u}) = \frac{e^{\pi i|\mathbf{u}|^2/\lambda f}}{\lambda f} \int \Psi_1(\mathbf{x}) \exp(-2\pi i\mathbf{x} \cdot \mathbf{u}/\lambda f) d\mathbf{x}, \quad (2.5)$$

$$= \frac{e^{\pi i|\mathbf{u}|^2/\lambda f}}{\lambda f} \mathcal{F} [\Psi_1(\mathbf{x})]_{\mathbf{u}/\lambda f}. \quad (2.6)$$

Here, $\mathbf{x} \equiv (x, y)$ and $\mathbf{u} \equiv (u, v)$ are the locations in the pupil and image planes, respectively, f is the focal length of the imaging system, and λ is the wavelength of light. Apart from a leading multiplicative term, the similarity of Eqs. 2.5–2.6 to the Fourier transform in Eqs. 2.1–2.2 is apparent through the correspondence of the amplitude in the image field at position \mathbf{u} with the spatial frequencies of the pupil field $\nu_{\mathbf{x}} \equiv (\nu_x, \nu_y) = \mathbf{u}/\lambda f$. The *intensity* in the image plane is

$$I(\mathbf{u}) = |\Psi_2(\mathbf{u})|^2. \quad (2.7)$$

The intensity as defined here is for monochromatic electromagnetic waves, although for quasi-monochromatic waves (i.e. narrow-band), it can be regarded as the time-average of the squared modulus of the transverse electric field. Note that this definition is not equivalent to that of *specific intensity* typical in astronomy. Instead, the intensity defined here is proportional to the power per unit area per unit frequency.

For an unresolved source, this function, when normalized to unity, gives the point spread function (PSF),

$$S(\mathbf{u}) = \frac{I(\mathbf{u})}{\int I(\mathbf{u}) d\mathbf{u}}. \quad (2.8)$$

This is the impulse response of the optical system. Indeed, the imaging process is well-described in the context of linear systems theory in general, and frequency analysis in particular. The Fourier transform of the PSF is the optical transfer function (OTF),

$$\tilde{S}(\mathbf{f}) \equiv \mathcal{F}[S(\mathbf{u})]. \quad (2.9)$$

It gives the response of the image to perturbations in the pupil (input) field as a function of spatial frequency.

With a few exceptions (e.g. masers), astronomical sources are generally incoherent emitters. Mathematically, the intensity distribution in an image of a resolved source is described by the sum of image intensities calculated by decomposing the resolved source into a distribution of unresolved point sources. In high-contrast imaging, the unresolved star dominates the intensity in the image plane, and we can largely restrict our consideration of the imaging system to its PSF.

As an example, consider the image of an unresolved source in an idealized system consisting of a circular pupil. The pupil function $P(\mathbf{x}) = \Pi(|\mathbf{x}|/D)$, where D is the diameter of the pupil, and $\Pi(x)$ is the tophat function:

$$\Pi(x) \equiv \begin{cases} 1 & |x| \leq \frac{1}{2}, \\ 0 & |x| > \frac{1}{2}. \end{cases} \quad (2.10)$$

For unit amplitude, the field in the pupil plane is just $\Psi_1(\mathbf{x}) = P(\mathbf{x})$, and the corresponding field in the image plane is

$$\Psi_2(\mathbf{u}) = \frac{D}{2i\rho} J_1(\pi D\rho/\lambda f), \quad (2.11)$$

where $\rho^2 = u^2 + v^2$ and J_1 is the first-order Bessel function of the first kind. The resulting intensity distribution is the familiar Airy pattern,

$$I(\mathbf{u}) = \frac{D^2}{4\rho^2} J_1^2(\pi D\rho/\lambda f). \quad (2.12)$$

Static (time-independent) errors in the wavefront alter the resulting PSF. Propagated to the pupil plane, such errors can be deviations from a field with a flat phase, deviations from uniform amplitude, or a combination of both. In such a case, $\Psi_1(\mathbf{x}) \neq P(\mathbf{x})$.

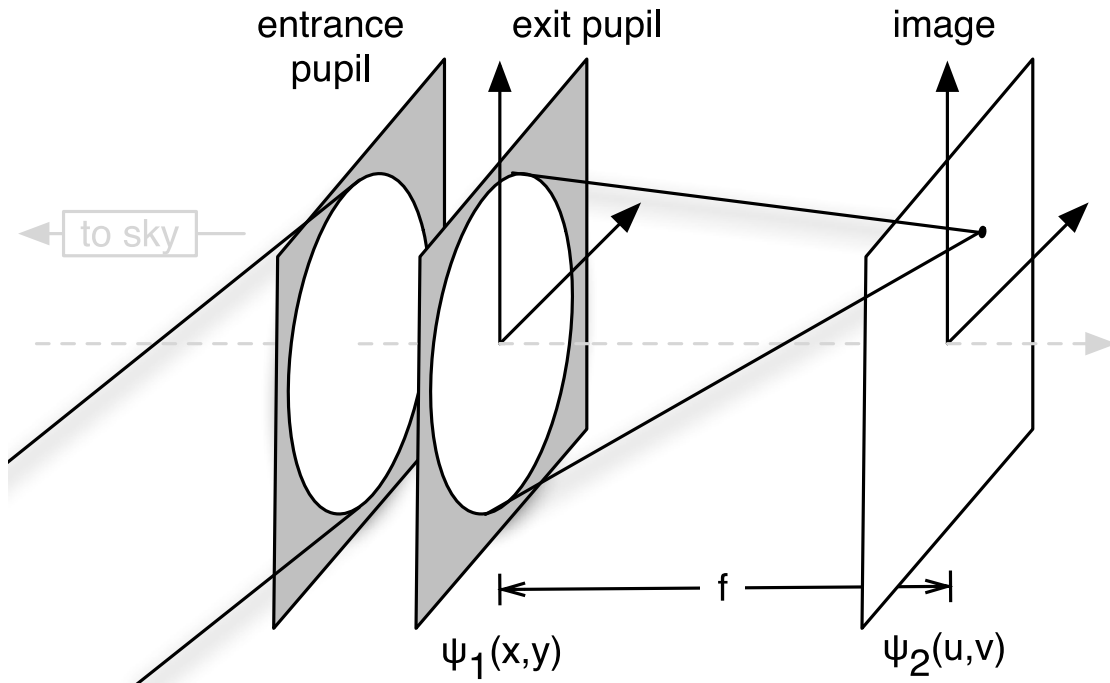


Figure 2.1 Layout of a generic astronomical imaging system. Waves from an unresolved source enter the imaging systems from the left. The optics between the entrance and exit pupils are treated as a “black box,” and can be assumed to propagate in the geometrical optics regime. The complex amplitude of the wave in the exit pupil, $\Psi_1(\mathbf{x}) \equiv \Psi_1(x, y)$, propagates to the image plane via Fraunhofer diffraction. The resulting complex amplitude in the image plane is $\Psi_2(\mathbf{u}) \equiv \Psi_2(u, v)$. Given f , the focal length, $\theta = u/f$ and $\phi = v/f$ are angles corresponding to the direction of the source on the sky.

The scale of the diffraction pattern in the image plane is a function of the wavelength. For a given pupil plane amplitude, the spatial scale of the image plane intensity distribution is proportional to λ . In broadband imaging, the total intensity is the integral over the intensity patterns at each wavelength.

In most scenarios we will consider, the measured quantity is the time-integrated intensity (as opposed to the instantaneous intensity I). For an exposure of time T , we define

$$W(t) \equiv \int_{-T/2}^{T/2} I(t) dt. \quad (2.13)$$

The average instantaneous intensity is simply $\langle I \rangle_t = \langle W \rangle_t / T$.

The variance of the integrated intensity, the fundamental consideration in contrast calculations, is less straightforward. In general, the wavefront errors will be functions of time. The instantaneous intensity in the image plane constitutes a random process, which we assume to be ergodic (and as a consequence wide-sense stationary). The variance of the integrated intensity is then (Goodman 1985, §6.1.1)

$$\sigma_W^2 = T \int_{-T}^T \Lambda\left(\frac{\tau}{T}\right) \mathcal{C}_I(\tau) d\tau, \quad (2.14)$$

where $\Lambda(x)$ is the triangle function

$$\Lambda(x) \equiv \begin{cases} 1 - |x| & |x| \leq 1, \\ 0 & \text{otherwise,} \end{cases} \quad (2.15)$$

and $\mathcal{C}_I(\tau)$ is the autocovariance function of the instantaneous intensity,

$$\mathcal{C}_I(\tau) \equiv \lim_{T \rightarrow \infty} \frac{1}{T} \int_{-T/2}^{T/2} I(t) I(t + \tau) dt - \langle I(t) \rangle_t^2. \quad (2.16)$$

Note that $\mathcal{C}_I(0) = \sigma_I^2$, and that the autocovariance is simply related to the temporal power spectral density of the instantaneous intensity via the Wiener-Kinchin theorem. If there are long-timescale correlations (power in low temporal frequencies) that are on the order of the integration time T , the integral in Eq. 2.14 will be large, as will the uncertainty in the mean integrated intensity. This limits the achievable contrast.

2.1.2 Limitations with a Stable PSF

The essential problem of high-contrast imaging rests on our ability to know the stellar PSF, which is used to distinguish the light from the stellar PSF from the faint circumstellar material in the image. In general, we do not know *a priori* the form of the PSF. A common approach to estimating this PSF is to image a different star with similar properties (i.e. brightness and color) nearby in time, and hope that nothing changes. If the ratio of the target stellar flux to that of the reference star is known or can be estimated, then the reference PSF can be scaled and subtracted from the target image. This depends on the temporal stability of the wavefront errors and on the availability of suitable reference stars. The best reference stars are nearby on the sky, to minimize differences in wavefront error, are spectrally well-matched over the observing band(s), and are observed as contemporaneously as possible. Because errors arising from atmospheric turbulence do not affect spacecraft, wavefront errors can be much more stable when the imaging system is outside the atmosphere (I will discuss the effects of atmospheric turbulence and the origin of “seeing” in §2.1.4). However, space-based optical systems can still be perturbed by vibrations and thermal fluctuations.

In the ideal case of perfect temporal stability of wavefront errors, the fundamental limits to achievable contrast arise from Poisson fluctuations in the photons of the stellar PSF (either the target or reference), and therefore the contrast is limited only by the exposure time.

2.1.3 Instrumental Limitations

The instrumental limits to contrast arise because so-called “static” wavefront errors slowly fluctuate, introducing time-dependence to quasi-static speckles in the image. In space-based imaging, these slow fluctuations in the wavefront error are largely caused by thermal perturbations to the optics and metering structure arising from variability in the spacecraft insolation. Changes in the thermal conditions affect both the telescope and instrument, as their materials usually have nonzero coefficients of thermal expansion. In the case of *HST*, the telescope “breathing” is

related to periodic occultation the Earth as the spacecraft moves in its orbit (Hartig et al. 2003). Fluctuations in wavefront error can also arise within instrumentation by other means. For example, instruments at the prime or Cassegrain foci of a telescope are subject to changing direction of the gravitational force. Such changes in gravity also induce flexure in the telescope structure, which can cause time-variability in the wavefront errors entering the instrument. The specific timescales of quasi-static aberrations are unique to each instrumental configuration.

2.1.4 Atmospheric Limitations

In ground-based observing, the atmosphere introduces random, time-variable aberrations into the plane waves arriving from distant point sources. In a long-exposure image, the resulting fluctuations in the instantaneous PSFs average out into a smooth “seeing disk,” which limits both spatial resolution and contrast. This subsection will review the effects of atmospheric turbulence on image formation and achievable contrast. A more detailed review of the statistical properties of images formed through atmospheric turbulence can be found in the classic monograph by Roddier (1981), from which key points are recapitulated here.

When light waves propagate through the atmosphere, deviations in the complex amplitude arise from fluctuations in the temperature and relative humidity, which create inhomogeneity in the spatial distribution of the air’s refractive index. In turbulence, it has been shown that the spatial statistics of such passive scalars follow Kolmogorov’s law from small to large scales (Obukhov 1949). Under Kolmogorov statistics, the three dimensional power spectra of turbulent fluctuations are $\propto \kappa^{-5/3}$, where κ is the wavenumber. The statistical properties of Kolmogorov turbulence are by definition homogenous and isotropic. However, the properties of atmospheric turbulence vary both spatially and temporally. In examining the effects of atmospheric turbulence through a cylinder whose base is the aperture of a telescope, we assume that Kolmogorov turbulence holds locally in a series of thin layers, each at different altitude. The turbulent aberrations from a given layer primarily affect the phase of the wave’s complex amplitude as it propagates through the layer. The effect of these aberrations on the field at a given height h and thickness δh can be described by the

second order moment $B_h(\boldsymbol{\xi})$,

$$B_h(\boldsymbol{\xi}) \equiv \langle \Psi_h(\mathbf{x}) \Psi_h^*(\mathbf{x} + \boldsymbol{\xi}) \rangle_{\mathbf{x}}, \quad (2.17)$$

$$= \exp \left[-\frac{1}{2} \left(2.91 \frac{4\pi^2}{\lambda^2} C_n^2(h) \delta h |\boldsymbol{\xi}|^{5/3} \right) \right], \quad (2.18)$$

$$= \exp \left[-\frac{1}{2} D_\phi(\boldsymbol{\xi}) \right]. \quad (2.19)$$

Here, $C_n^2(h)$ parameterizes the strength of the turbulent fluctuations in the air's refractive index as a function of height. The moment $B_h(\boldsymbol{\xi})$ is referred to as the coherence function, as it describes the degree of spatial coherence in the wave. The quantity $D_\phi(\boldsymbol{\xi})$ is the phase structure function of the turbulent aberrations. The 5/3 power-law index arises from the Kolmogorov spectrum. These aberrated waves undergo diffraction as they propagate to the entrance pupil of the telescope, and they are further aberrated by each layer of turbulence. A striking property of the coherence function $B_h(\boldsymbol{\xi})$ is that it is invariant under Fresnel propagation. This gives a straightforward relationship between the turbulence profile $C_n^2(h)$ and the coherence function at the entrance pupil of the telescope:

$$B_0(\boldsymbol{\xi}) = \exp \left[-\frac{1}{2} \left(2.91 \frac{4\pi^2 |\boldsymbol{\xi}|^{5/3}}{\lambda^2 \cos \gamma} \int C_n^2(h) dh \right) \right]. \quad (2.20)$$

The angle from zenith is denoted γ .

In the image plane, the time evolution of speckles is governed by the both the changes in refractive index in each layer, and the spatial translation of the different layers. An approximately valid assumption in astronomical imaging is that of Taylor's frozen flow, in which the index fluctuations in a given layer are fixed, and the speckle evolution arises from the velocity structure of the turbulent layers, $\mathbf{v}(h)$.

In the long-exposure PSF observed through the atmosphere, the fluctuations of the wavefront error due to turbulence overwhelm the static errors present in the telescope and camera. We can decompose the field in the pupil in terms of the contribution from both sources of error,

$$\Psi_1(\mathbf{x}) = \Psi_{\text{atm}}(\mathbf{x}) \Psi_{\text{sta}}(\mathbf{x}). \quad (2.21)$$

As such, we can lump these static errors into the pupil function,

$$P'(\mathbf{x}) \equiv P(\mathbf{x}) \Psi_{\text{sta}}(\mathbf{x}). \quad (2.22)$$

The long-exposure OTF is then (Hufnagel & Stanley 1964)

$$\langle \tilde{S}(\mathbf{f}) \rangle_t \propto \int \langle \Psi_1(\mathbf{x}) \Psi_1^*(\mathbf{x} + \mathbf{f}) \rangle_t P(\mathbf{x}) P^*(\mathbf{x} + \mathbf{f}) d\mathbf{x}, \quad (2.23)$$

$$= \int \langle \Psi_{\text{atm}}(\mathbf{x}) \Psi_{\text{atm}}^*(\mathbf{x} + \mathbf{f}) \rangle_t P'(\mathbf{x}) P'^*(\mathbf{x} + \mathbf{f}) d\mathbf{x}. \quad (2.24)$$

We can relate the terms involving Ψ_{atm} to the coherence function B_0 . Since $B_0(\mathbf{f}) = \langle \Psi_{\text{atm}}(\mathbf{x}) \Psi_{\text{atm}}(\mathbf{x} + \mathbf{f}) \rangle_{\mathbf{x},t}$ is only a function of spatial frequency \mathbf{f} , we can rewrite Eq. 2.24 as

$$\langle \tilde{S}(\mathbf{f}) \rangle_t \propto B_0(\mathbf{f}) \int P'(\mathbf{x}) P'^*(\mathbf{x} + \mathbf{f}) d\mathbf{x}. \quad (2.25)$$

This OTF determines the PSF arising from observations through a turbulent atmosphere. A convenient parameterization of the turbulence profile was introduced by Fried (1966). His parameter r_0 characterizes the effect of the turbulence profile on the resolution of the PSF. This parameter is the diameter of an atmosphere-free telescope whose resolving power matches that of an infinitely large telescope that is subject to atmospheric turbulence. The parameter

$$r_0 = \left[0.423 \frac{4\pi^2}{\lambda^2 \cos \gamma} \int C_n^2(h) dh \right]^{-3/5}, \quad (2.26)$$

which gives the simple expression

$$B_0(\boldsymbol{\xi}) = \exp \left[-3.44 (\boldsymbol{\xi}/r_0)^{5/3} \right]. \quad (2.27)$$

In the “seeing-limited” case, $D \gg r_0$, and the atmospheric coherence function dominates the structure of the OTF:

$$\langle \tilde{S}(\mathbf{f}) \rangle_t \propto B_0(\mathbf{f}). \quad (2.28)$$

The PSF then has characteristic width $\lambda f/r_0$. As the exponent of 5/3 appearing in Eq. 2.27 is close to 6/3 = 2, we find $B_0(\mathbf{f})$ is close to a Gaussian. The PSF is $\mathcal{F}\{B_0(\mathbf{f})\}$, the form of the long-exposure seeing-limited PSF is commonly approximated by a Gaussian. This gives reasonable accuracy inward of 1–2”, but severely under-predicts the wings of the PSF (King 1971). Ad-hoc equations have been devised to fit the slower PSF fall-off in seeing-limited images, such as that of Moffat (1969). In general, models based on the power-spectrum of turbulent fluctuations

produce a better fit out to several arcseconds. Beyond this distance, in the PSF aureole, the structure is probably formed by high-spatial-frequency errors from telescope optics or small-particle scattering (Roddier 1981, §4.5).

The contrast limits are set by the fluctuations of the speckles in the image plane. In particular, at a given location in the image plane, speckle intensity fluctuates according to the strength $C_n^2(h)$ and velocity $\mathbf{v}(h)$ of the Taylor flow (Roddier et al. 1982). This assumes that the turbulent fluctuations constitute a temporally stationary random process, which not the case in practice (since the C_n^2 and \mathbf{v} profiles change with time). Assuming stationarity, the timescales for speckle fluctuation can be set by the mean pupil-crossing time, $D/\langle v \rangle$, and the dispersion in velocities, $r_0/\Delta v$. The former quantity is independent of wavelength, while the latter, sometimes called the “boiling” time, follows the wavelength dependence of r_0 . Experimental measurements of speckle fluctuation timescales in seeing-limited measurements have shown that the boiling timescale is dominant (e.g. Aime et al. 1986). Furthermore, quasi-static speckles can still play a role in setting the limits to contrast in uncompensated observations through atmospheric turbulence. For example, the secondary mirror supports (“spiders”) create diffraction spikes, which can slowly fluctuate in time (with seeing changes and flexure).

More severe are the temporal fluctuations in the strength of the turbulence. In general, the temporal power spectrum $r_0(t)$ is significant over a broad range of frequencies, and it must be measured to accurately quantify the contrast limits of seeing-limited observations (Racine 1996; Avila et al. 2004).

2.1.5 Point Sources and Extended Emission

For a given time-varying PSF, the detectability of circumstellar emission depends on its spatial frequency content. Stellar and substellar companions to the target star are point sources, and the power spectra of their images have the same spatial frequency content as the target star. For circumstellar disks, the primary variables affecting their spatial frequency content are the angular size of the disk and the viewing inclination. The power spectra of extended face-on disks concentrate most of the power in low spatial frequencies. In contrast, edge-on disks have

asymmetric 2-d power spectra. In the direction along the midplane, low frequencies dominate as in the face-on case. Perpendicular to the midplane, however, they resemble point sources in that the spatial frequency content more closely resembles that of the OTF.

The primary difficulty in detecting faint point sources stems from the fact that they have similar appearance to residual speckles in the stellar image (PSF). It is usually possible to remove the global structure of the stellar PSF such that only residual speckles remain (i.e. by subtracting an azimuthally symmetric radial profile). If the observations are diffraction-limited (as in space-based or adaptive optics imaging), the residual fluctuations have size $\sim \lambda f/D$, which is the same approximate scale as the central core of the PSF of both the target star and companion. Note that in general, speckles have different spatial structures compared to diffraction-limited cores (in sufficiently narrow or broad bands), and image processing techniques exist to filter the image based on these differences (Masciadri & Raga 2004). The contrast limit is set by the local speckle noise in the time-integrated exposure. At a given location, this depends on both the variance of speckle intensity and the timescale for decorrelation of the speckles.

The temporal non-stationarity of turbulence affects the global structure of the PSF. This is most clearly illustrated by considering $r_0(t)$. The characteristic width of the stellar PSF's seeing halo, $\lambda f/r_0(t)$, is now a function of time. In a long-exposure image, the average of the instantaneous PSFs is still a radially smooth function. Thus, the global stellar PSF structure can be subtracted from the long-exposure image. This can reveal the images of point sources, as long as they are located beyond $\lambda/r_0(t)$ on the sky. However, for face-on disks, which are centered on the star, the smooth radial structure of the disk is covariant with the structure of the PSF. We then require a sufficiently precise estimate of PSF structure, which cannot come from non-contemporaneous reference star observations due to the temporal non-stationarity of the turbulence. Therefore, the contrast limits for extended emission are strongly affected by the stability of global PSF structure and depend on the atmospheric conditions at the time of observation.

2.2 Coronagraphy

A coronagraph is a device that suppresses the diffraction of on-axis starlight into the image plane, while still allowing off-axis light from other sources to propagate through the system. Its primary purpose is for high-contrast imaging. It was invented by Bernard Lyot in order to study the solar corona without the need of an eclipse by the Moon (Lyot 1939).

A Lyot coronagraph is similar to a normal imaging system, but with the addition of a few optics which allow manipulation of the electric field in the focal and pupil planes. In addition to the lenses or reflective surfaces for additional focal and pupil planes, the essential components of a Lyot coronagraph are the focal and Lyot masks.

The focal mask is placed at the location of the star in the focal plane, and is responsible for occulting its light. By suppressing the core of the PSF, the focal mask suppresses the starlight across all spatial frequencies in the pupil. Considering the Airy pattern arising from a circular pupil, the focal mask transmits power in the Airy rings falling outside the focal mask. These rings contain high spatial frequencies in the image plane, which roughly correspond to locations near the edge of the aperture in the pupil plane. The Lyot mask is placed in a subsequent pupil plane (the “Lyot plane”). This then suppresses the diffraction of the starlight from the focal mask, reducing power in the Airy wings. The geometry of the Lyot coronagraph is shown in Figure 2.2. A pedagogical treatment including expressions for the propagation of the complex amplitude through the system is given in Sivaramakrishnan et al. (2001).

There are other schemes for increasing contrast. These either suppressing the image of the on-axis starlight, or alter the spatial distribution of incoming starlight such that it does not fall in the regions of interest. Arguably the most well-known of these schemes is the technique of apodization, which suppresses the strength of the PSF Airy rings at the expense of a slightly wider core. It is possible to combine apodization and traditional Lyot coronagraphy, as in the Apodized Pupil Lyot Coronagraph (APLC) technique (e.g. Soummer 2005). Other schemes seek to manipulate the phase of the incident radiation to cancel out the starlight, as in Phase

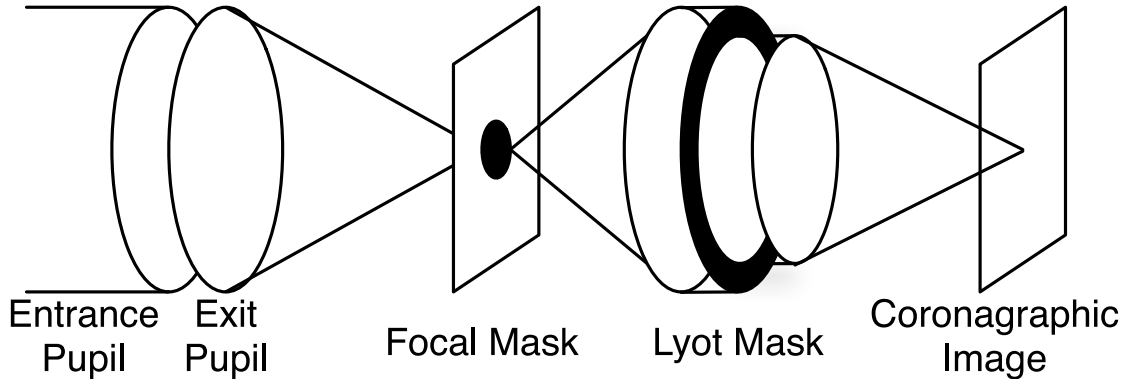


Figure 2.2 Geometry of a Lyot coronagraph. Incoming light is imaged in the first focal plane. The focal mask occults the central portion of the on-axis diffraction pattern. The pupil is then re-imaged in the Lyot plane. The Lyot mask removes the high-spatial-frequency content of the occulted image (e.g. Airy rings). The resulting field is then imaged onto the science camera.

Induced Amplitude Apodization (e.g. Guyon et al. 2005) and nulling coronagraphs like the Four Quadrant Phase Mask (Rouan et al. 2000) and Optical Vortex Coronagraphs (Foo et al. 2005).

The use of coronagraphy improves contrast by suppressing the on-axis PSF. However, the contrast can still be limited by the leakage of wavefront errors through the coronagraph. Consider the case of a speckle that falls outside the mask in the first focal plane. This speckle corresponds to energy of an error with mid-range spatial frequency in the entrance pupil of the telescope. In the Lyot plane, the effect of the narrow focal mask is to convolve the mid-frequency error with a broad function (of characteristic width given by the inverse of the focal mask size). This spreads the energy throughout the Lyot plane while maintaining the same periodicity of the original error. However, some of the energy in this error now falls outside the Lyot mask. In the final image, the speckle will still exist at the same location because the pupil-plane frequency is unchanged, however it has a diminished amplitude that depends on the Lyot mask size. The Lyot coronagraph suppresses speckles falling outside the focal plane mask, however it also suppresses off-axis sources by the same

amount. Airy rings, on the other hand, are periodic, and their power in the Lyot plane is concentrated near the edges. The Lyot stop effectively masks the power in the Airy rings, improving contrast. Therefore we see that the coronagraph suppresses the structure in the Airy rings of the PSF, however the quasi-static speckles are not strongly suppressed.

Lyot coronagraphs in space have demonstrated contrast gains in comparison to traditional unocculted imaging. For example, the Advanced Camera for Surveys aboard the *Hubble Space Telescope* has demonstrated coronagraphic gains in point source sensitivity of ~ 2 mag at separations of $2''$ relative to direct imaging (Krist 2004). The subtraction of reference PSFs provides further gains still. Reference PSF subtraction for direct images shows a gain of ~ 2 mag relative to an unsubtracted direct image, while reference PSF subtraction in coronagraphic images shows a gain of ~ 4 mag relative to unsubtracted coronagraphic images. Thus, the combination of reference PSF subtraction and coronagraphic imaging increases the sensitivity to point sources by ~ 6 mag relative to unsubtracted direct imaging. The achievable contrast is limited by quasi-static wavefront errors.

In seeing-limited imaging, the atmosphere imposes severe limitations to the ability of coronagraphs to achieve high contrast. Like the case of quasi-static speckles, the coronagraph does little to suppress speckles arising from atmospheric turbulence (Sivaramakrishnan et al. 2001; Guyon 2005). The coronagraph is only capable of suppressing the Airy rings, and not quasi-static or atmospheric speckles (since these are diminished by about the same amount as the off-axis sources we are trying to detect). Thus, coronagraphs are only useful where the Airy rings dominate the seeing-disk halo. (Though they may be used to prevent detector saturation.) This points to the need for active wavefront correction, to remove static and atmospheric wavefront errors from the unocculted PSF so that the coronagraph can suppress the resulting Airy pattern.

2.3 The Promise of Adaptive Optics

In §2.1, I showed that the structure and variability of the PSF strongly affects the achievable contrast and sensitivity to circumstellar material. In §2.2, it became clear that Lyot coronagraphs are most successful at suppressing aberration-free PSFs, while residual wavefront errors can propagate through the instrument and limit contrast. With the advent of adaptive optics (AO), telescopes are now equipped with technology to reduce instrumental and atmospheric aberrations and therefore have the potential to significantly improve our ability to detect faint material near bright stars. In this section, I will give an overview of AO for ground-based high-contrast imaging.

Astronomical adaptive optics systems usually operate in a closed loop. The incoming wavefronts are corrected by one or more deformable mirrors (DMs). The light is then split into two paths; one path is sent to the wavefront sensor (WFS; possibly more than one), while the other is sent to the science camera. Currently, the most popular form of wavefront sensor is the Shack-Hartmann lenslet array. A computer system uses the wavefront sensor measurements to actuate the DMs. A typical ground-based, single-conjugate adaptive optics system consists of a single DM, a visible wavefront sensor, and an infrared science camera. The closed-loop bandwidths are sufficiently great to time-resolve the changes in the turbulent phase screens above the telescope, typically in the 1 kHz range.

The action of closed-loop AO control removes power in low-spatial-frequency phase errors. This alters the structure of the long-exposure PSF from the seeing disk typical in uncompensated imaging. Under low to moderate AO correction on moderate to large telescopes (where $D \gg r_0$), the PSF can be simply approximated (Racine et al. 1999). The core of the PSF is proportional to the diffraction pattern of the telescope and imaging system in the absence of atmospheric turbulence. The halo is related to the seeing disk, which is the PSF of an uncompensated imaging system. In this decomposition, the PSF is simply

$$I = SI_{\text{core}} + (1 - S)I_{\text{halo}}. \quad (2.29)$$

Here, S is the Strehl ratio, which is unity for an unaberrated system (neglecting

static aberrations). For increasing AO performance, S approaches unity — the halo intensity decreases, while the power in the unaberrated portion of the PSF increases. Alternately, one may think of the OTF increasing at higher spatial frequencies (less information is attenuated). However, under increasing correction, the approximation breaks down. The decomposition in Eq. 2.29 should be used for conceptual purposes only, as the structure of the PSF in the high-Strehl regime is more complicated (e.g. Perrin et al. 2003). The AO system can only produce a PSF dominated by the turbulence-free diffraction pattern out to a certain angular scale, θ_{AO} . This is because the DM, having an array of actuators, can only correct spatial frequencies up to the Nyquist limit as determined by the interactuator spacing. For a DM with N_{act} actuators across the pupil, we have (Sivaramakrishnan et al. 2001),

$$\theta_{\text{AO}} = \frac{N_{\text{act}}\lambda}{2D}. \quad (2.30)$$

Thus Airy rings will only be prominent in the PSF out to θ_{AO} , assuming $r_0 \ll D$.

Adaptive optics correction improves the achievable contrast relative to uncompensated ground-based imaging. First, because the AO system reduces the energy in the halo, the variance of the PSF in this zone is reduced (by a factor $\propto 1 - S$ in the above model). Thus, it is easier to detect faint emission in this region. Second, the AO system alters the companion PSF, potentially sharpening it to have a diffraction-limited core. This raises the peak intensity of a companion or emission from circumstellar dust (by a factor $\propto S$), making it easier to detect. Together, we see that the AO system can have a strong effect on sensitivity: these effects combined increase sensitivity by a factor $\propto S/(1 - S)$.

The addition of an AO system to a high-contrast imager can complicate the presence of quasi-static speckles, which will dominate the PSF variation in the well-corrected region inward of θ_{AO} . An AO system introduces several optical elements in the path to the science camera. The flexure changes due to thermal and gravity variation can introduce more quasi-static speckles, and decrease the timescales of their variation (complicating PSF subtraction). Additionally, the AO system is dependent on two separate paths for the light (the WFS path and science path). It is common practice for non-common-path aberrations to be calibrated by setting

reference centroid positions for the Shack-Hartmann spots. The DM is driven so that the observed centroids match the reference positions, rather than zero. Both flexure and seeing changes (which change the WFS spot size) can cause variation in the optimal reference centroid positions, introducing time-variable errors of spatial frequencies that correspond to speckles in the region inward of θ_{AO} — essentially, introducing quasi-static speckles. The level and timescales of quasi-static speckles have been measured in a high-Strehl AO coronagraph by Hinkley et al. (2007), and the effects of residual atmospheric speckles and slowly varying quasi-static speckles on the achievable contrast of an AO coronagraph have been studied by Soummer et al. (2007).

The use of adaptive optics can significantly enhance the ability of a coronagraph to suppress on-axis starlight. Under good AO correction, the non-coronagraphic PSF will show Airy rings inward of θ_{AO} . A coronagraph can suppress the PSF structure in this region (Sivaramakrishnan et al. 2001; Guyon 2005). This advantage, coupled with the increase in peak signal due to the sharper off-axis PSF, greatly increases the sensitivity to faint circumstellar material relative to uncompensated ground-based imaging. Further, for space-based imaging, future AO systems will be able to control the appearance of quasi-static speckles. Such speckle suppression techniques will further improve coronagraphic sensitivity (e.g. Give'On et al. 2006; Bordé et al. 2006). The theoretical limits to coronagraph performance have been studied by Guyon (2005). He finds that with space-based coronagraphs with AO wavefront control to the sub- \AA level, the theoretical limit to the “useful throughput” of a coronagraph is given by one minus the unaberrated, non-coronagraphic stellar PSF.

I will describe the use of AO and space-based coronagraphs to image the scattered light of circumstellar debris in Chapter 4, and in Chap. 5 I will describe my algorithm for using AO coronagraphy to image the debris disk around AU Mic.

Chapter 3

Statistics of Adaptively Corrected Speckles

3.1 Introduction

Wavefronts from astronomical sources are invariably distorted before being imaged by the observer, resulting spatio-temporally fluctuating “speckles” of image plane intensity. Speckle noise limits the dynamic range of long exposures in the vicinity of a bright source (Roddier 1981; Racine et al. 1999), hampering observational goals like direct detection of close-in extrasolar planetary systems.

Speckle interferometry (Labeyrie 1970) and adaptive optics (AO) have succeeded in achieving diffraction-limited spatial resolution in the presence of atmospheric turbulence. However, contrast levels achievable with these techniques are limited by speckles and are generally orders of magnitude below the dynamic range required for planet detection. Additional strategies exist to remove speckle noise and increase contrast. If the speckles are long-lived as in space telescopes, reference PSF subtraction and roll subtraction can be used (Fraquelli et al. 2004). More advanced techniques exist for speckles varying on shorter timescales, such as multiwavelength Simultaneous Differential Imaging (Racine et al. 1999; Marois et al. 2000, 2004, 2005; Lenzen et al. 2004; Biller et al. 2004), “dark” speckle (Labeyrie 1995; Boccaletti et al. 1998), and Synchronous Interferometric Speckle Subtraction (Guyon 2004).

We study the fundamental properties of speckles to illuminate both the limits and design of future instrumentation and observational methodology, in particular high-order adaptive optics coronagraphy (e.g. Sivaramakrishnan et al. 2001; Ford et al. 2003; Trauger et al. 2003; Macintosh et al. 2004).

Several authors have developed statistical descriptions of stellar speckles in ground-based images. In the uncompensated case of the visible and near-IR, speckle interferometry is the main driver of these theoretical and observational studies. This method uses sequences of short-exposure, spatially well-sampled images to retrieve a single high-resolution image. The focus of previous statistical studies lies in short-exposure images' spatial power spectra and atmosphere/telescope optical transfer functions which are central to the technique (e.g. Fried 1966; Dainty 1974; Dainty et al. 1981; Roddier 1981; Aime et al. 1986; Vernin et al. 1991).

In contrast to techniques which increase resolution of uncompensated images through post-processing, AO images possess a diffraction-limited core formed by spatially coherent light in the pupil. The superposition of this coherent light with residual wave aberrations modifies the character of the speckle distribution from the uncompensated case. The description of speckle statistics in both regimes can be related to the study of laser speckles (Goodman 1975, 1985), the theoretical statistical formalisms of which have been previously applied to AO-corrected astronomical speckle patterns (Canales & Cagigal 1999b; Soummer & Aime 2004; Aime & Soummer 2004, hereafter AS04).

For companion detection, we are interested in the distribution of intensity in the image plane. In high-Strehl-ratio images, diffraction of wave aberrations results in amplification of speckles near Airy maxima, hence the phenomenon of “speckle pinning” (Bloemhof et al. 2001; Sivaramakrishnan et al. 2002; Bloemhof 2003; Perrin et al. 2003). As noted by AS04, this behavior is described by the theoretical distribution of intensity originally derived by Goodman (1975) (see also Goodman 1985). Cagigal & Canales (2001) observed this distribution in a laboratory setting, using a spatial light modulator to simultaneously simulate turbulence and partial correction with AO.

This chapter presents on-sky results consistent with predictions of the theoretic-

cal speckle statistics for compensated astronomical imaging through the atmosphere. Section 3.2 partially recapitulates the treatment of the intensity distribution given by AS04. Section 3.3 describes observations of short-exposure stellar images under moderate correction. Analysis and discussion of these results in light of direct imaging techniques follow in sections 3.4 and 3.5.

3.2 Probabilistic Description of Intensity

Here we characterize the probability distributions of image plane intensity in the case of an unresolved astronomical source subject to random wavefront aberrations. In this section, we follow the development of the probability density function presented by AS04, adopting their notation. The problem has been studied elsewhere to the same conclusions by Goodman (1975, 1985), Canales & Cagigal (1999b), and Soummer & Aime (2004).

3.2.1 Intensity in the Image Plane

We wish to study the properties of intensity in the image plane by considering an undistorted light wave from an astronomical source, as well as aberrations of the wave introduced by the atmosphere and telescope. Studying the superposition of the perfect wave and the aberrations allows us to conveniently express intensity statistics useful for companion detection. Here, we consider the case of a narrow-band wave ($\Delta\lambda/\lambda \ll 1$) which has entered the telescope, passed through any corrective optics (e.g. AO system), and further propagated into the entrance pupil of an imaging system. We ignore polarization and treat the light as a scalar wave. We represent the wave at a given location by a complex amplitude, which describes the envelope function of the oscillating (scalar) electric field.

At a given time t and position \mathbf{u} in the entrance pupil of the imaging system, the complex amplitude of the wave is represented by $\Psi_1(\mathbf{u}, t)$ and can be decomposed into the superposition of an undisturbed wave of amplitude A , which is constant in

space and time, and random wave aberrations $a(\mathbf{u}, t)$,

$$\Psi_1(\mathbf{u}, t) \equiv [A + a(\mathbf{u}, t)] P(\mathbf{u}). \quad (3.1)$$

The aberrations $a(\mathbf{u}, t)$ are time-varying fluctuations in the residual wave amplitude arising from the partially-corrected distortions. The pupil function (unity inside the pupil, zero outside) and static aberrations are encapsulated in $P(\mathbf{u})$. With this definition we may take A as a positive real number without loss of generality.

The wave in the image plane $\Psi_2(\mathbf{x})$ is the Fourier transform $\mathcal{F}\{\cdot\}$ of the wave in the pupil plane,

$$\begin{aligned} \Psi_2(\mathbf{x}, t) &= \mathcal{F}\{\Psi_1(\mathbf{u}, t)\} = A\mathcal{F}\{P(\mathbf{u})\} + \mathcal{F}\{a(\mathbf{u}, t)P(\mathbf{u})\}, \\ &= C(\mathbf{x}) + S(\mathbf{x}, t). \end{aligned} \quad (3.2)$$

The resulting image plane wave is represented as a superposition of two complex wave amplitudes. C represents the amplitude of the temporally static portion of the image plane wave, while S represents the amplitude arising from random aberrations.

The intensity is the squared modulus of $\Psi_2(\mathbf{x}, t)$,

$$I(\mathbf{x}, t) = |\Psi_2(\mathbf{x}, t)|^2 = |C(\mathbf{x})|^2 + |S(\mathbf{x}, t)|^2 + 2\text{Re}[C^*(\mathbf{x})S(\mathbf{x}, t)], \quad (3.3)$$

where $*$ represents the complex conjugate. Additionally, one can define I_c and I_s as the time-averaged intensities corresponding to the coherent and speckle wavefront amplitudes in the image plane:

$$\langle I(\mathbf{x}, t) \rangle = I_c(\mathbf{x}) + I_s(\mathbf{x}) \quad (3.4)$$

$$I_c(\mathbf{x}) \equiv |C(\mathbf{x})|^2 \quad (3.5)$$

$$I_s(\mathbf{x}) \equiv \langle |S(\mathbf{x}, t)|^2 \rangle \quad (3.6)$$

The final intensity term on the right of equation (3.3) is an interference term resulting from the superposition of the C and S waves, which has zero mean, and thus does not enter into equation (3.4).

Although $I_c(\mathbf{x})$ and $I_s(\mathbf{x})$ are positive definite quantities, we stress that energy is conserved when equation (3.4) is integrated over the image plane. Indeed, when

adding perturbations to the system, energy conservation constrains the value of A . Consider the case of pure phase perturbations,

$$\Psi_1(\mathbf{u}, t) = e^{i\phi(\mathbf{u}, t)} P(\mathbf{u}), \quad (3.7)$$

which have no effect on the spatially-integrated mean intensity. Qualitatively, as a direct result of the definition in equation (3.1) and energy conservation, an increase in the scale of $\phi(\mathbf{u}, t)$ decreases the value of A and the scale of $\int I_c(\mathbf{x}) d\mathbf{x}$.

In this chapter, probabilistic descriptions are formed of the intensity at a single location in space, $I(t)$, omitting \mathbf{x} for brevity. We describe the intensity as a stochastic process – a sample function $I(t)$ is observed, which is drawn from the overall ensemble of such functions. For simplicity, we assume that the aberrations driving the intensity fluctuations constitute an ergodic process, so that we may take ensemble averages $\langle \cdot \rangle$ in equations (3.4) and (3.6) to equivalently represent time averages. In reality, atmospheric fluctuations are not temporally stationary, and we could redefine A as a function of time, and I_c , I_s as the ensemble-averages of temporal functions.

3.2.2 The Distribution of Intensity

The behavior of speckles can be described via the probability distribution of intensity, characterized by $p(I)$, the probability density function (*pdf*). This is a first-order description of the stochastic process for I in which time is marginalized.

We assume that in equation (3.2), the image-plane amplitude Ψ_2 is formed by the linear combination of a large number of independent phasors from the pupil plane. From the central limit theorem, this addition results in Gaussian statistics for the real and imaginary parts of the image plane amplitude, regardless of the particular statistics governing the pupil plane phasors. The Gaussian *pdf* of the image plane phasors is used to compute the *pdf* of the intensity, $p(I)$.

The form of $p(I)$ follows from steps involving a change of variables from the phasor components. Originally derived by Goodman (1975), the resulting function

is the modified Rician (MR) distribution,

$$p_{\text{MR}}(I) = \frac{1}{I_s} \exp\left(-\frac{I + I_c}{I_s}\right) I_0\left(\frac{2\sqrt{II_c}}{I_s}\right), \quad (3.8)$$

where $I_0(x)$ denotes the zero-order modified Bessel function of the first kind. For $I_c = 0$, the distribution becomes the exponential statistics of ‘pure’ speckle, of primary interest in speckle interferometry.

Intensity fluctuations play a critical role in the signal-to-noise ratio of direct imaging observations. Goodman (1975) showed that the mean and variance of I are

$$\mu_I = I_c + I_s \quad (3.9)$$

$$\sigma_I^2 = I_s^2 + 2I_c I_s. \quad (3.10)$$

From equation (3.10), we see that the variance arising from pure speckle (the first term on the right-hand side of the expression) is augmented by the presence of the coherent wave.

We have expressions describing the statistics of image plane intensity in an idealized absence of photon and detector noise. The effect of photon noise on equations (3.8) and (3.10) has been studied elsewhere (Canales & Cagigal 1999a; Aime & Soummer 2004; Soummer & Aime 2004). The addition of incoherent light (e.g. from a planet) is addressed by AS04. Detector read noise can be a significant factor in short-exposure images. We can model read noise as the sum of a Gaussian random variable with the actual speckle intensity. We take the read noise distribution to be zero-mean with standard deviation σ_{rn} . Denoting this the MRG model, the *pdf* for the resulting observable is broader than the MR case, and is given by the convolution of equation (3.8) with a Gaussian *pdf*,

$$p_{\text{MRG}}(I) = p_{\text{MR}}(I) \star p_{\text{G}}(I). \quad (3.11)$$

3.3 Observations

3.3.1 Measurements and Data Processing

On 2004 July 31, we observed the star Sadalmelik (α Aqr, G2Ib), chosen for its apparent brightness in the K band ($m_K = 0.59$, 2.5×10^7 photons $\text{m}^{-2} \mu\text{m}^{-1} \text{s}^{-1}$).

We obtained compensated short-exposure images under good weather conditions using the AO system of UCO/Lick Observatory’s 3-meter Shane Telescope on Mt. Hamilton (Bauman et al. 2002). There are 61 actuators on the deformable mirror used for wavefront control. The AO system was run at 500 Hz in a closed feedback loop.

Rapid sequences of short-exposure images were obtained with IRCAL, the infrared camera which images the AO-corrected light onto a 256-by-256 Rockwell Semiconductor PICNIC array (Lloyd et al. 2000). Detector readout is driven by a digital signal processor within an Astronomical Readout Cameras, Inc. electronics system (Leach & Low 2000). The observations were made through a narrow-band Br γ filter (2.16 μm , $\Delta\lambda/\lambda \sim 1\%$), where the detector is Nyquist sampled by 75.6 mas pixels.

We developed an array readout mode optimized for minimal delay between exposures in order to accurately measure the spatial and temporal distribution of stellar speckle patterns. Typical mode parameters were for correlated-double-sampling (CDS) a 32×32 pixel ($2''.4 \times 2''.4$) subarray with 5 ms integration times. With these settings, exposures were obtained every $\Delta t = 14.5$ ms, and in 13 seconds a sequence of 900 images could be obtained before writing to disk. As demonstrated below, time spent in overhead between exposures (pixel ‘dead time’, about 9.5 ms) is unimportant, as it is shorter than the speckle decorrelation time ($t_{\text{dead}} < \tau_c$). The *rms* CDS read noise σ_{rn} is measured to be $45 e^-$ in this mode. Photon noise fluctuations do not strongly affect the statistics of these data.

The image sequences were processed before analysis, including bias-subtraction and flat-fielding. Tip/tilt error affects image plane intensity statistics, a fact illustrated by considering the extended Maréchal approximation: the Strehl ratio (and by extension, total coherent intensity) decreases exponentially with the phase variance. We removed the residual tip/tilt error, reducing phase variance, to maximize the range of I_c . After a centroid measurement, each image was shifted and resampled with a damped-sinc interpolator. The observed 2-D *rms* tip/tilt error was .43 pixels (32 mas).

In section 3.4, we will examine the distribution function for speckle intensities

at each pixel using the measured time series. Examples of these time series for three locations in the image plane are shown in Figure 3.1. The locations were chosen to highlight the diversity in intensity distribution as a function of location in the image plane. Large deviations from the mean intensity are visible at location (*a*), while the data in location (*c*), close to the PSF core, do not show such large excursions.

3.3.2 Temporal Characteristics

We wish to analyze our measurements in light of the probability distribution functions for the intensity random variable. The statistical tests we will employ in §3.4.1 require that the tested data be drawn from independent random variables. However, we observe the intensity as a realization of a temporal random process, and correlations exist between intensities at different times. In order to perform tests concerning the distribution of independent values of intensity, we must determine the timescale over which samples of $I(t)$ can be considered independent. We assume temporal stationarity for the duration of the observations, so that we may take the statistical properties to be constant in time.

At a single spatial location in the tip/tilt-removed image sequence, the number of independent samples can be characterized by the speckle decorrelation time, $\tau_c(\mathbf{x})$. Previous definitions of τ_c have been motivated by the the desire to compute optimal exposure times in speckle interferometry (Roddier et al. 1982, and references therein). The decorrelation time is derived from the temporal autocovariance function $\mathcal{C}_I(\tau)$. It can be the e-folding value of this function, as in Scaddan & Walker (1978), Roddier et al. (1982), and Vernin et al. (1991). It can also be defined by the equivalent width,

$$\tau_c = \sigma_I^{-2} \int_{-\infty}^{\infty} \mathcal{C}_I(\tau) d\tau, \quad (3.12)$$

following Aime et al. (1986), who found their empirical $\mathcal{C}_I(\tau)$ was fit by the sum of two Lorentzian functions. The equivalent-width definition assumes no prior knowledge about the shape of the autocovariance function, and has the advantage of using information contained in the function's tail. Decorrelation times τ_c computed from equation (3.12) are generally longer than those computed by *e*-folding (Aime et al.

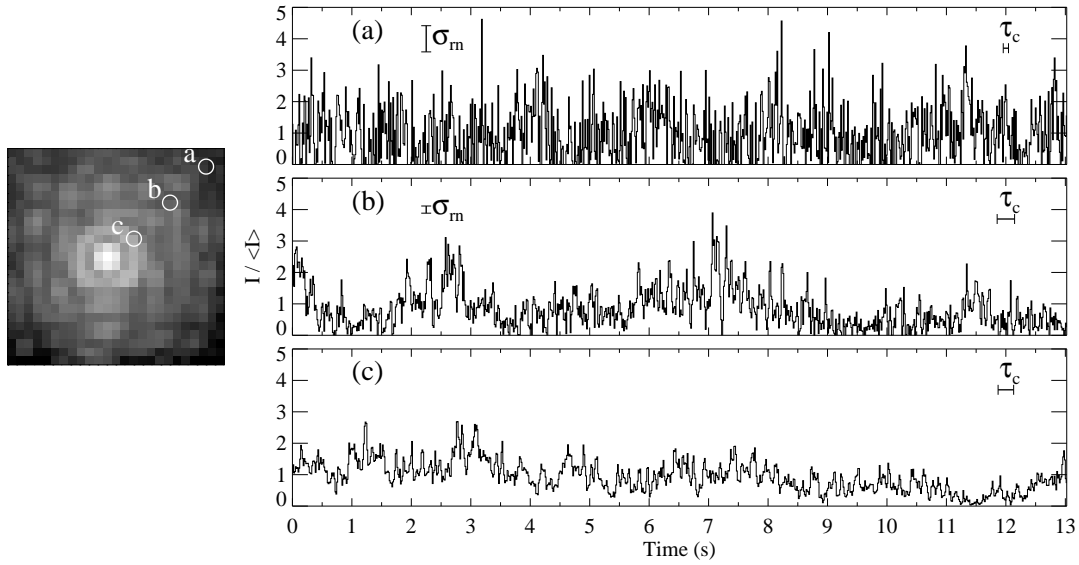


Figure 3.1 The long-exposure image (left, log scale), and a plot of observed intensity as a function of time for three selected pixels (right), the encircled locations (a), (b), and (c). The locations were chosen to highlight the diversity of speckle intensity distribution as a function of image plane position, moving from the PSF halo to the first Airy ring. For each pixel, 900 measurements are shown at a sampling period of 14.5 ms, which consists of 5 ms integration and 9.5 ms of dead time. To illustrate differences in speckle fluctuations with field position, the intensity for each location is normalized by its sample mean, which was 54, 200, and 1800 e^- respectively for (a), (b), and (c). The scale of fluctuations relative to the mean intensity decreases from locations (a) to (c). Read noise and decorrelation time are shown as scale bars. The read noise at location (c) is negligible.

1986). This definition also has the property that the variance of the intensity integrated over time $T \gg \tau_c$ is given by $\sigma_I^2 T \tau_c$.

In practice, we compute τ_c for each pixel, approximating the integral as the sum of an estimator for the autocovariance sequence (*acvs*) over the interval ± 35 samples (± 0.5 s). We restrict the summation domain because the *acvs* estimate becomes more uncertain with increasing lag τ . Estimating the error in τ_c is complicated by the large correlations between terms in the *acvs* estimate, and it suffices for the analysis in §3.4.1 to neglect its calculation. Limiting the summation domain in the calculation of τ_c generally results in an underestimate of the true decorrelation time. Finally, note that the effect of read noise is not removed from the *acvs* in the τ_c calculation. In this case, τ_c will be lower than the speckle-only decorrelation timescale in regions of significant detector noise.

Figure 3.2 shows the *acvs* estimates for the selected locations from Figure 3.1, along with the τ_c given by the aforementioned procedure. As shown in the inset of Figure 3.2, the τ_c are observed to vary with field position \mathbf{x} . Analysis of the spatial dependence of speckles' temporal decorrelation is deferred for future work.

The measured decorrelation times are generally many times the sampling rate Δt , which ensures that we may disregard the effect of finite integration time and pixel dead time on the analysis of the observed intensity distributions. The median decorrelation time was 175 ms, and the first and third quartiles of the measured $\tau_c(\mathbf{x})$ distribution are 95 ms and 270 ms, respectively.

As in Aime et al. (1986), the forms of the *acvs* estimates in Figure 3.2 are qualitatively consistent with the sum of two Lorentzian functions. A unique decorrelation timescale characterizes the width of each component Lorentzian. For locations (a)-(c), the fast timescale varies between 20 and 80 milliseconds while the slow timescale lies between .8 and 1.2 seconds.

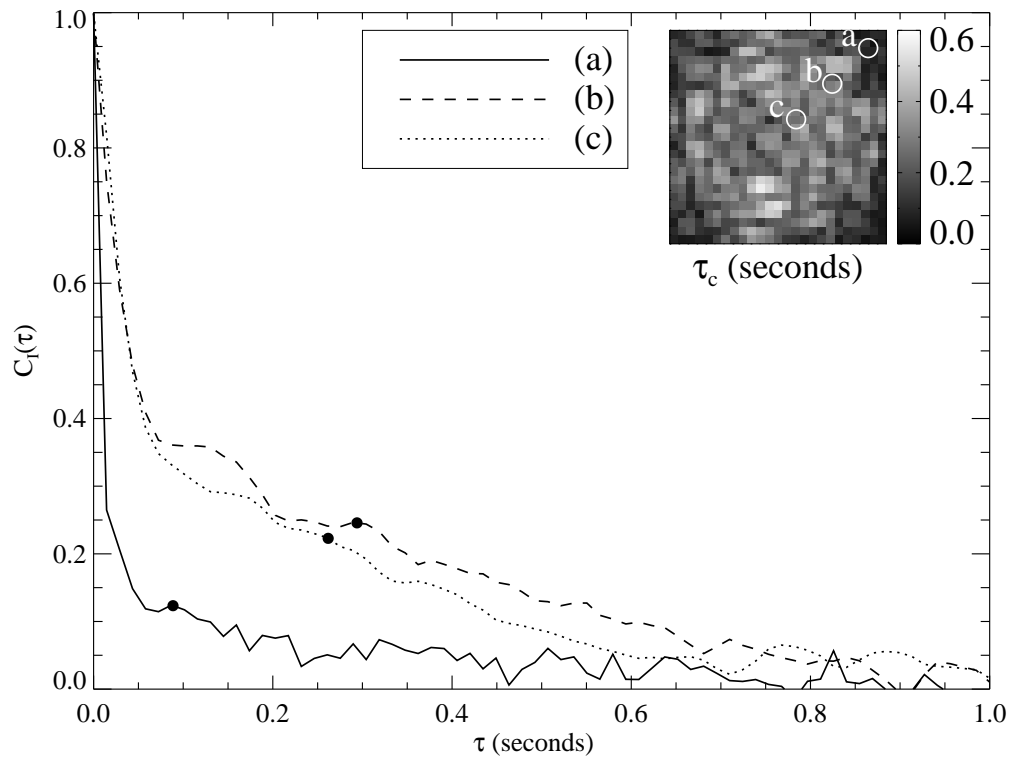


Figure 3.2 Autocovariance sequence (*acvs*) estimates for the time series intensity data from pixels (a)-(c) in Figure 3.1. The abscissae of the filled circles denote the decorrelation times τ_c computed from the *acvs* estimates. The τ_c characterize the number of independent speckle realizations in a given time period, and are observed to vary systematically with field position as illustrated by the inset map. Sampling effects are minimized with the short sampling period of 14.5 ms.

3.4 Analysis

3.4.1 Testing the Distribution

The observed distribution of speckle intensities can act as a consistency check against the modified Rician distribution, $p_{\text{MR}}(I)$ defined in equation (3.8). Neglecting photon counting fluctuations, we expect the observed intensities to be the sum of a modified Rician random variable and an independent Gaussian random variable for the read noise, with distribution $p_{\text{MRG}}(I)$ given by equation (3.11). We adopt as a null hypothesis that the distribution of intensities follows the model distribution, with parameters \hat{I}_c and \hat{I}_s estimated from the data (where the caret denotes an estimate).

For each pixel location, the observed sequence of images gives a measure of the intensity as a function of time. Data from five consecutive 900-exposure sequences were combined into the same histogram. Section 3.3.2 describes temporal correlations in the observed sequences, which arise from correlations in the perturbations $a(t, \mathbf{u})$. To mitigate the effect of temporally correlated data in hypothesis tests which assume independent measurements, we formed the histogram after decimating each intensity sequence at intervals of the pixel's decorrelation time, $\Delta t' = \tau_c$. The data in between these intervals were discarded, as were values falling below zero. Examples of the resulting histograms are shown in Figure 3.3 using the data for locations (a)-(c) from Figures 3.1 and 3.2.

An iterative least-squares fit of the model distribution to the histogram estimates the parameters \hat{I}_c and \hat{I}_s , holding the read noise σ_{rn} fixed. We perform this fit at each location in the image. Best-fit models for distributions of locations (a)-(c) are also shown in Figure 3.3. We choose the least-squares approach to parameter estimation for simplicity, though one might develop maximum-likelihood estimators. We briefly discuss potential bias in our estimators below.

The residuals of the fit are used in a χ^2 test to determine if the hypothetical model distribution function should be rejected. The number of degrees of freedom (nominally the number of histogram bins) is reduced to account for the estimation of distribution parameters from the data. We can calculate the p -value from the χ_n^2

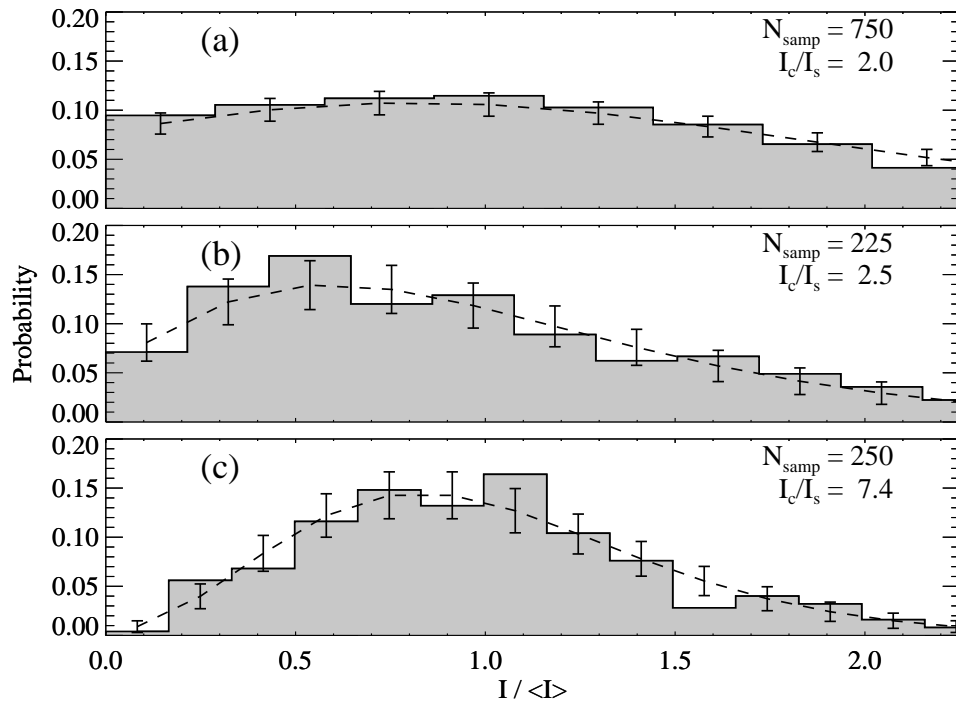


Figure 3.3 Histograms of intensity with best-fit model distribution function (dashed curve) for the data of locations (a)-(c) shown in Figures 3.1 and 3.2. Also shown are $1\text{-}\sigma$ errors for the model distribution. As in Figure 3.1, intensity is normalized by the sample mean. Inset are the number of samples in this histogram (after resampling the original timeseries by $\Delta t' = \tau_c$), and the ratio of parameters \hat{I}_c and \hat{I}_s characterizing the model distribution.

distribution and reject the hypothesized distribution if this measure falls below the significance level α (taken to be 5%).

In contrast to a generic χ^2 test, we can also use a hypothesis test based on the empirical cumulative distribution function like the Kolmogorov-Smirnov (K-S) test. While both tests determine a p -value for rejecting hypotheses, we expect the K-S test to be make fewer Type II errors (failing to reject false null hypotheses) because it avoids binning data. Disadvantages to the K-S test include a relative insensitivity to distribution tails and a much larger computation requirement: as we are using estimated parameters in the hypothesized distribution, it is necessary to determine the K-S test statistic's distribution function to find the p -value. This can be done with a bootstrap Monte Carlo method, where the parameters \hat{I}_c and \hat{I}_s (estimated from the observations) are used to simulate a random variable following the model distribution. For each trial i in the Monte Carlo simulation, distribution parameters are estimated from the simulated data (via the preceding least-squares fit procedure) and the K-S test statistic D_i is calculated. After the completion of 1,000 trials, the distribution of D_i is used to estimate the p -value. We restrict the use of this form of the K-S test to example pixel locations (a)-(c) because the requisite simulations cannot be calculated in a timely fashion given our computational resources. However, the χ^2 test is applicable to the entire field.

The results of the hypothesis tests for the example locations are shown in Table 3.1. We see that neither the χ^2 nor the K-S tests reject the hypothetical MRG model for these data. The table presents similar test results for the MR model, as well as a Gaussian (G) with free parameters μ and σ . We did not test a separate Poisson model because the data are not in the photon counting regime. As read noise significantly affects the observed distribution of location (a), the model distributions consistent with Gaussian read noise provide the best fits. However, the pure Gaussian model G is only marginally significant for locations (a) and (c), while the asymmetric distribution at (b) ensures rejection. The MRG model is not rejected by either test at all three locations.

When examining the results of the χ^2 hypothesis test over the image, we find that the MRG distribution hypothesis is not rejected for 90% of the pixels. This

Table 3.1. Hypothesis Test Results

Location	Model	χ^2/n_{dof}	p -value	
			χ^2 test	K-S test
(a)	G	1.61	0.051	0.26 ± 0.03
(a)	MR	2.10	<i>0.0087</i>	<i>0.001</i> \pm 0.001
(a)	MRG	0.90	0.46	0.11 ± 0.02
(b)	G	2.51	<i>0.0011</i>	<i>0.015</i> \pm 0.007
(b)	MR	0.51	0.87	<i>0.001</i> \pm 0.001
(b)	MRG	0.55	0.83	0.10 ± 0.02
(c)	G	1.44	0.096	0.17 ± 0.02
(c)	MR	0.85	0.51	0.52 ± 0.03
(c)	MRG	0.85	0.51	0.54 ± 0.03

Note. — Results of χ^2 and Kolmogorov-Smirnov hypothesis tests for fits to intensity data. G, MR, and MRG refer to the Gaussian, modified Rician, and modified Rician plus a (zero-mean, $\sigma = \sigma_{\text{rn}}$) Gaussian models for intensity distribution. Instances of distribution rejection are indicated in italics, and occur when the p -value falls below the significance level $\alpha = .05$. The mean and variance of the G model and parameters I_c , I_s of the MR and MRG models are estimated from the data, and n_{dof} is the number of histogram bins minus the number of estimated parameters. The quoted uncertainty in the K-S test p -values corresponds to 95% confidence.

is slightly lower than the expected rate of $(1 - \alpha) = 95\%$, which is indicative of marginally significant processes which alter the intensity distribution.

Several processes may bias the results of these tests. Read noise acts to broaden the density function, which limits the accuracy and precision of the \hat{I}_c and \hat{I}_s estimates in regions of low signal. Additionally, we have chosen to neglect photon noise, as generally $\sigma_I^2 \gg \langle I \rangle$. Finite pixel size also plays a role in altering the distribution from the ideal case, as the pixels' area is a significant fraction of a speckle. The spatially integrated speckle distribution has also been studied by Goodman (1975, 1985), though we do not consider that case here. Another caveat arises from the non-stationarity of the process governing the wavefront distortion term $a(\mathbf{u}, t)$ in the compensated imaging system, as this term is driven by the atmospheric turbulence (Roddiier 1981, and references therein). These fluctuations can bias the estimates \hat{I}_c and \hat{I}_s and therefore reduce goodness-of-fit. Finally, we expect second-order correlations in the sampled intensities arising from τ_c underestimates to cause Type I errors, an increase in the test rejection rate from α when the hypothesis is true.

3.4.2 Coherent PSF Extraction

The parameter estimation procedure above provides the spatial distributions of $\hat{I}_c(\mathbf{x})$ and $\hat{I}_s(\mathbf{x})$, the sum of which forms the long-exposure image via equation (3.4). Figure 3.4 shows the $\hat{I}_c(\mathbf{x})$ and $\hat{I}_s(\mathbf{x})$ extracted from the observations. As we obtain uncertainties of the estimates for these quantities via least-squares fitting, it is possible to make a crude calculation for the S/N in the estimated parameters. Neglecting systematic biases, the median S/N over all pixels are 7.6 and 4.8 for $\hat{I}_c(\mathbf{x})$ and $\hat{I}_s(\mathbf{x})$, respectively, in data gathered in 1 minute of observing time. It may be possible, through maximum-likelihood analysis, to develop improved estimators which avoid binning data before parameter estimation.

While $I_c(\mathbf{x})$ is a difficult quantity to measure, as it is proportional to the PSF of a system free of atmospheric turbulence, its knowledge can be valuable. It may have utility in calibrating methods which reconstruct the long-exposure PSF ($T \gg \tau_c$). With the technique of Véran et al. (1997a), data from the AO system are

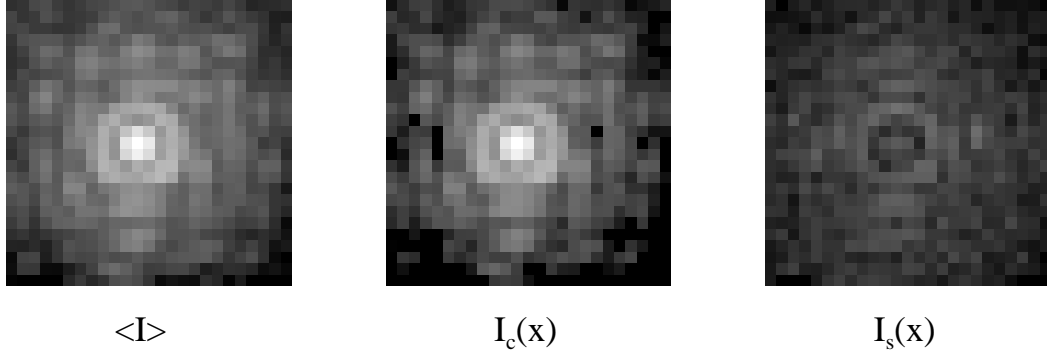


Figure 3.4 Decomposition of the long-exposure PSF $\sim \langle I(\mathbf{x}) \rangle$, reprised from Figure 3.1, into $\hat{I}_c(\mathbf{x})$ and $\hat{I}_s(\mathbf{x})$ as in equation (3.4). By definition, the quantity $I_c(\mathbf{x})$ is proportional to the static PSF. Images are displayed with the same logarithmic scale.

used to calculate a blurring kernel. This kernel is convolved with a static PSF ($\propto I_c$) to estimate the on-axis long-exposure PSF. This static PSF contains non-common path aberrations, and in standard practice is calibrated by an artificial point source or observations of a reference star (Véran et al. 1997b). A drawback in the artificial source case is that aberrations with high spatial frequency arising from the primary mirror are not sensed. When using a reference star, calibrating the static PSF requires an accurate construction of the blurring kernel during the reference observation. Obtaining $\hat{I}_c(\mathbf{x})$ by estimating the parameters of the speckle intensity distribution function (as in §3.4.1) can be used to calibrate the PSF reconstruction in a manner independent of a blurring kernel estimate, though errors such as those arising from temporal non-stationarity may limit the accuracy. Finally, we note that the reference star calibration method presented in Véran et al. (1997b) and the speckle distribution function method above require that the calibration target be a point source. If incoherent light is added as from a companion or extended emission, the speckle distribution will be altered from the MR. An analytical expression for the intensity distribution function in this case is given by AS04.

3.5 Conclusions

We have shown observations of speckle intensity over timescales of ~ 1 min are consistent with modified Rician statistics through χ^2 and Kolmogorov-Smirnov goodness-of-fit tests. In high-contrast imaging for planet detection, the variance of the integrated intensity at the location of the planet sets the noise level against which the signal must be detected. Central to understanding this noise level are the variance of intensity σ_I^2 and the speckle decorrelation time τ_c . AS04 highlight the efficacy of coronagraphs in reducing σ_I^2 by reducing terms containing I_c . For example, suppose $I_c = I_s = 1$. From equation (3.10), $\sigma_I^2 = 3$. With a coronagraph, $I_c = 0$ and $\sigma_I^2 = 1$, a reduction by a factor of 3 in variance. However, a complete understanding of speckle fluctuations in coronagraphic imaging experiments will require characterization of τ_c , as well as understanding the effects of non-stationarity in I_c and I_s due to changes in the atmosphere and quasi-static wavefront errors in the optical system. Analyses of observed intensity distributions over timescales longer than 1 min are left to future work.

We note that the dark speckle imaging technique relies on analysis of the observed intensity distribution at each location \mathbf{x} (Labeyrie 1995; Boccaletti et al. 1998), and has traditionally assumed exponential statistics for intensity. Here we have demonstrated that probability distributions related to the modified Rician are applicable in the case of moderate wavefront correction and thus may be incorporated into this technique. AS04 give speckle distributions for additive planet light and photon-counting conditions which can be used to this end.

Additionally, we have presented a technique where $I_c(\mathbf{x})$ and $I_s(\mathbf{x})$ are estimated from the observed distributions of intensity. Knowledge of the unaberrated PSF, proportional to $I_c(\mathbf{x})$, can be applied to the calibration of PSF reconstruction algorithms (Véran et al. 1997a). This application may spur the further development of estimators for I_c and I_s given an observed speckle intensity distribution.

Chapter 4

Circumstellar Debris Disks

Theoretical models for the accretion of solids into cores and planets have been developed to explain the formation of Solar and extrasolar planets (Greenberg et al. 1978; Stevenson 1982; Pollack et al. 1996; Weidenschilling et al. 1997; Goldreich et al. 2004; Alibert et al. 2005, and references therein). Although planet formation theory has advanced in conjunction with new observational capabilities, significant questions remain to be answered. For example, what are the timescales for the formation of planets, and how do these compare to the dissipation of primordial gas and dust? How do these timescales vary for stars of different mass and birth environments? The solids in circumstellar disks are dynamically linked to each other and the primordial gas disks, and they are heavily influenced by planetary embryos (e.g. Goldreich et al. 2004). A full accounting of the temporal evolution of planet-building material requires detailed analysis of planetesimal growth, and one of the largest areas of uncertainty is how they grow from cm to km sizes. Such questions are likely to be complicated by the migration of planets and planetary embryos through the disk, which can excite the orbits of the solids and cause collisions to be destructive, rather than constructive. The migration and subsequent interaction of planets have an effect on the diversity of orbits in planetary systems. These processes are naturally linked to those governing the dissipation of solid material in young circumstellar disks. However, there is still uncertainty as to how the dissipation of solids occurs over the lifetimes of stars. Are primordial planetesimals ground

to debris in steady state, or are dynamically catastrophic events such as the Late Heavy Bombardment (e.g. Tera et al. 1974; Hartmann et al. 2000) in our Solar System common? The processes affecting the dynamical behavior of planetesimals are fundamental to understanding the evolution of solid material in protoplanetary disks, and are essential for understanding the occurrence of planets around stars of differing type and environment.

The late stages in the evolution of circumstellar material are represented by debris disks, which are characterized by the presence of optically thin dust around stars. In such systems, the stars are old enough such that their primordial gas disks have dissipated (on timescales of 1–10 Myr; e.g. Zuckerman et al. 1995; Haisch et al. 2001). Dust removal mechanisms ensure that the dust in these systems is not primordial; rather it is replenished through the destruction of primitive planetesimals. The debris is freshly nourished by the sublimation, evaporation, and collisional destruction of orbiting parent bodies (for a recent review, cf. Meyer et al. 2007). Since a portion of these parent bodies may take part in the accretion of cores into planets — which may in turn gravitationally perturb the dust — circumstellar debris disks offer evidence for the presence of planets and insight into their formation.

This chapter will review how observations and inferences of debris disk architectures can illuminate the dynamical processes affecting the evolution of circumstellar material (§4.1). This is followed by an overview of the current state of debris disk observations, with a focus on direct imaging (§4.2). Finally, the application of adaptive optics coronagraphy to the study of circumstellar debris disks will be discussed (§4.3).

4.1 Debris Disk Architectures

The architectures of debris disks reflect both the underlying distribution of parent planetesimals and physical processes acting on the grains. The measurement of disk architectures an important observational tool for informing theories of the formation of planets and circumstellar disk evolution. Most fundamental to the structure are the locations of the planetesimals, which are commonly assumed to occur in belts like our Asteroid and Kuiper Belts. Such belts have been observa-

tionally inferred to exist in debris disks like β Pic (e.g. Okamoto et al. 2004) and AU Mic (e.g. Strubbe & Chiang 2006). Dust is generated by the parent planetesimals through mutual collisions or the sublimation of ices, akin to comets. As the orbits of the resulting grains, if bound, initially share the pericenter of the original parent body, they can be used in principle to map out the locations of the unseen parent bodies.

Once generated by the planetesimal population, the dust grains' trajectories are altered by a variety of forces and processes. An analytical and numerical treatment of many of these effects was recently given for the debris disk of AU Mic by Strubbe & Chiang (2006). I briefly review the processes here.

gravity Gravity from the star is fundamental to determining grain orbits. Planets can also alter dust orbits through gravitational interaction, considered later in this section.

radiation pressure Incident starlight transfers momentum to the grains. While the interaction of light with dust molecules is a quantum process, we can calculate the rate at which photons collide with a given grain in the classical sense through an effective cross section. For a spherical grain of radius a , this differs from the geometric cross section πa^2 by a wavelength-dependent efficiency factor Q_{pr} . The radial component of the resulting force is the outward-directed radiation pressure, and is well-documented by Burns et al. (1979). The ratio of radiation pressure to gravity equals

$$\beta_{\text{rad}} \equiv \frac{F_{\text{rad}}}{F_{\text{grav}}} = \frac{3}{16\pi} \frac{\tilde{Q}_{\text{pr}} L_*}{GM_* c \rho a}, \quad (4.1)$$

where c is the speed of light, M_* and L_* are the stellar mass and luminosity, and a and ρ are the grain size and density. Here, the tilde over the radiation force coupling efficiency \tilde{Q}_{pr} signifies an average over the stellar spectrum. The Q_{pr} efficiency factor is related to the scattering and absorption efficiencies via $Q_{\text{pr}} = Q_{\text{abs}} + Q_{\text{sca}}(1 - \langle \cos \alpha \rangle)$, where $\langle \cos \alpha \rangle$ parameterizes the scattering anisotropy averaged over angle relative to the incoming starlight. Particles for which $\beta > 0.5$ are blown out of the system. If \tilde{Q}_{pr} monotonically decreases

with increasing grain size (not true for many grain materials at sizes $\ll 1 \mu\text{m}$), then this defines a blowout size,

$$a_{\text{blow}} \equiv \frac{3}{8\pi} \frac{\tilde{Q}_{\text{pr}} L_*}{GM_* c \rho}. \quad (4.2)$$

Grains with sizes $a < a_{\text{blow}}$ will be removed from the system on short dynamical (free-fall) timescales ($\lesssim 10^4$ yr).

Poynting-Robertson drag The tangential component of the radiation force is directed counter to the azimuthal velocity of the grain relative to the star and is responsible for PR drag. A grain's orbit, having a periastron distance r_{peri} and eccentricity e , is modified over time by this drag force such that it spirals in toward the star. The timescale for this inspiral to occur is

$$t_{\text{PR}} = \frac{4\pi c^2 \rho}{3L_* \tilde{Q}_{\text{pr}}} E(e) r_{\text{peri}}^2 a, \quad (4.3)$$

where the factor $E(e)$ governs the eccentricity decay (Wyatt & Whipple 1950),

$$E(e) = \frac{8}{5} \frac{(1+e)^2}{e^{8/5}} \int_0^e \frac{x^{3/5}}{(1-x^2)^{3/2}} dx. \quad (4.4)$$

For grains on eccentric orbits, PR drag tends to keep r_{peri} nearly fixed while slowly reducing the semimajor axis. In the case of such grains, the time spent reducing the eccentricity is much longer than the time spent reducing r_{peri} of a nearly circular orbit.

corpuscular pressure The stellar wind produces an effect similar to stellar radiation, and the outward component of the wind's acceleration of the grains is the corpuscular pressure. Since the momentum flux for both stellar radiation and wind scale as r^{-2} from the star, it is relatively straightforward to modify the equations above for corpuscular forces. In the case of stellar wind pressure, the factor \tilde{Q}_{pr} in Eqs. 4.1 and 4.2 is replaced by $Q_{\text{wind}} \dot{M}_* v_{\text{wind}} c / L_*$, giving

$$\beta_{\text{wind}} = \frac{F_{\text{wind}}}{F_{\text{grav}}} = \frac{3}{16\pi} \frac{Q_{\text{wind}} \dot{M}_* v_{\text{wind}}}{GM_* \rho a}, \quad (4.5)$$

$$a_{\text{blow}} = \frac{3}{8\pi} \frac{Q_{\text{wind}} \dot{M}_* v_{\text{wind}}}{GM_* \rho}. \quad (4.6)$$

Here, \dot{M}_* is the mass-loss rate of the star, and v_{wind} is the stellar wind velocity. The factor Q_{wind} relates the collision cross-section to the geometrical cross-section, and is likely to be approximately unity.

corpuscular drag The tangential component of the interaction with the stellar wind is responsible for producing corpuscular drag. We can similarly replace the factor \tilde{Q}_{pr} in Eq. 4.3 with the term $Q_{\text{wind}}\dot{M}_*c^2/L_*$, giving

$$t_{\text{C}} = \frac{4\pi\rho}{3Q_{\text{wind}}\dot{M}_*} E(e)r_{\text{peri}}^2 a. \quad (4.7)$$

gas drag The gaseous component of a circumstellar disk is supported against gravity in part by the gas pressure, and thus orbits with sub-Keplerian velocities. Here the gas under consideration orbits the star, as opposed to the outward-streaming stellar wind. The dust, on the other hand, is a pressureless fluid orbiting at the Keplerian rate. Due to the difference in velocities, collisions between grains and orbiting gas molecules introduce a drag force on the dust. The effect of gas drag on dust grains is described in Takeuchi & Artymowicz (2001). When the size of the grain is much smaller than the mean free path of the gas molecules, the force on a grain is

$$\mathbf{F}_g = -\pi\rho_g a^2 (v_T + \Delta v^2)^{1/2} \Delta \mathbf{v}, \quad (4.8)$$

Where ρ_g is the gas density, $\Delta \mathbf{v} = \mathbf{v} - \mathbf{v}_g$, \mathbf{v} and \mathbf{v}_g are the particle and gas velocities, and v_T is the thermal velocity of the gas,

$$v_T = \frac{4}{3} \left(\frac{8kT}{\pi\mu_g m_H} \right)^{1/2}, \quad (4.9)$$

where k is Boltzmann's constant, T and μ_g are the gas temperature and mean molecular weight, and m_H is the mass of the Hydrogen atom. In the subsonic case ($\Delta v < v_T$), grains couple to the gas disk in one dynamical time when the surface density of a grain (mass/cross-sectional area) is comparable to the gas disk surface density. The subsonic stopping time is

$$t_{ss} = \Omega_K^{-1} \frac{4\rho_d a v_K}{3\rho_g r v_T}, \quad (4.10)$$

where ρ_d is the density of the dust. The generalized stopping time is $t_s = t_{ss}/\sqrt{1 - \Delta v^2/v_T^2}$. In most places in circumstellar disks, the gas pressure P_g decreases with increasing radius, and the gas rotates at sub-Keplerian velocities,

$$v_g = v_K(1 - \eta)^{1/2}, \quad (4.11)$$

$$\eta \equiv -\frac{1}{r\Omega_K^2\rho_g} \frac{dP_g}{dr}, \quad (4.12)$$

where v_K and Ω_K are the Keplerian orbital velocity and angular frequency. If Δv is small, then the radial velocity of grains (subject to both radiation and gas forces) is

$$v_r = \frac{\beta - \eta - 2\beta(v_K/c)(t_s\Omega_K)}{(t_s\Omega_K) + (t_s\Omega_K)^{-1}}. \quad (4.13)$$

Both inward and outward migration are possible, depending on the values of β , η , and the stopping time t_s . Since radiation and gas forces may balance somewhere in the disk, gas drag provides a mechanism for creating ring-like structures in gaseous debris disks. These processes have been studied by Takeuchi & Artymowicz (2001) and Besla & Wu (2007).

collisions When grains collide at sufficient relative velocity, smaller grains are created in the destruction of larger grains, either through catastrophic destruction (large impact energy) or cratering (small impact energy). For a disk of single-size grains on near-circular orbits, the mean time between collisions is

$$t_c \sim \frac{1}{\Omega\tau_\perp}, \quad (4.14)$$

where Ω is the orbital frequency and τ_\perp is the geometric vertical optical depth. The threshold for catastrophic destruction of grains depends on the collisional specific energy Q_* , which in turn depends on the impact velocity and target size (e.g. Housen & Holsapple 1999). In a steady-state collisional cascade, assuming Q_* is independent of grain size, the size distribution follows $dn \propto a^{-7/2}da$ (Dohnanyi 1969; O'Brien & Greenberg 2003; Pan & Sari 2005). When other size-dependent forces are involved, the size distribution can depart from a $-7/2$ power law. In such systems, the calculation of the

size-dependent collisional lifetimes and equilibrium size distribution are complicated; recent modeling efforts for debris systems include Takeuchi & Artymowicz (2001), Strubbe & Chiang (2006), and Wyatt et al. (2007a). The upper-limit to this size distribution is set where the destructive collision time equals the age of the system. The collisional evolution of debris disks is modeled by Dominik & Decin (2003), Wyatt et al. (2007a), and Wyatt et al. (2007b).

others The forces and processes altering the grains in debris disks are not limited to the above. For grains sufficiently close to the star to be heated to temperatures > 100 K, water ice *sublimation* can destroy grains on short timescales. As estimated by Backman & Paresce (1993) from expressions in Isobe (1970), the timescale for sublimation of pure water ice grains is

$$t_{\text{sub}} = 1.5 \times 10^{-12} a \rho \frac{10^{2480/T}}{T^{7/2}} \text{ yr.} \quad (4.15)$$

Sputtering of grains occurs when rapidly moving atoms or ions collide with grains and remove material. In debris disks, this may be done by the stellar wind or by species rapidly accelerating due to radiation pressure (β -meteoroids). Lien (1990) considers the lifetime of grains including sublimation and sputtering, finding that for the Solar System, sublimation is important out to ~ 3 AU, while sputtering from the solar wind is dominant beyond this distance. Lien also finds that the presence of rocky impurities in the ice reduces the sublimation timescale. Finally, I note the effect of *photophoresis*, though different from gas drag, may cause radial migration of dust grains in the presence of a gas disk. This effect requires that a temperature gradient be maintained across the day and night sides of the grain, and may be important in coupling the dust disk to the inner edge of the gas disk during the transition from optically thick to optically thin conditions (Krauss & Wurm 2005).

The freshly produced material in debris disks is not limited to dust. Recent observations have shown that, while the primordial gas has dissipated, atomic gas may be present and can be linked to production mechanisms involving the dust grains in orbit around the star. To date, β Pic is the only system with conclusive evidence for

an atomic gas disk linked to the dust distribution. Spectroscopic observations indicate a stable gas component as well as time-variable features redshifted with respect to the star (e.g. Vidal-Madjar et al. 1994; Lagrange et al. 1998). These variable features have been interpreted as the result of evaporating cometary bodies falling toward the star (dubbed “falling evaporating bodies”). More recently, spectral features from the stable gas disk have been spatially resolved (Olofsson et al. 2001; Brandeker et al. 2004). This gas is observed to be in Keplerian rotation, which is initially puzzling since these species are expected to be rapidly ejected from the system via radiation pressure, and hydrogen cannot act as a braking agent. Subsequent models have suggested that the gas is produced by grain collisions (Fernández et al. 2006; Czechowski & Mann 2007). Fernández et al. (2006) suggest that, if carbon is overabundant, Coulomb forces from C II act as a braking agent for the outward flow of gas, while Czechowski & Mann (2007) argue that no braking is needed for the grain collision model to show a peak at Keplerian velocities. Another model has been proposed for the production of Na I whereby photon-stimulated desorption releases atoms from dust grains (Chen et al. 2007), with similar arguments for the observed Keplerian rotation curve. A stable component of Na I has also been observed along the line of sight to HD 32297 (Redfield 2007), however more observations are needed to constrain its distribution and the processes responsible for its presence.

The architecture of a debris disk can be affected by the gravitational interactions between a planet and the dust grains (e.g. Ozernoy et al. 2000; Kuchner & Holman 2003; Kenyon & Bromley 2004). Eccentric planets alter debris disks by pumping grain eccentricities through *secular perturbations*, causing an offset between the star and the disk centroid. This also causes “pericenter glow” in thermal emission (Wyatt et al. 1999). Dust can be temporarily trapped by *mean motion resonances* (MMRs) (e.g. Liou & Zook 1999; Kuchner & Holman 2003), as happens in the Solar System. Other signatures in the debris are produced by dust from colliding planetesimals which are themselves trapped in MMRs (Wyatt 2006). The planetesimals trapped by resonant sweeping occupy different resonances (2:1, 3:2, etc.). The relative populations in these resonances acts as a probe of planetary migration history (e.g. Murray-Clay & Chiang 2005).

The appearance of a debris disk may have dramatic variation with wavelength. This arises in both scattered-light and thermal imaging because different wavelengths probe different grain sizes. The accelerations from forces acting on the grains are often size-dependent — the largest grains may most accurately trace the distribution of planetesimals, while the smallest can be blown out of the system. (Indeed, most of the mass is in large bodies for a collisional $a^{-7/2}$ size distribution.) Thus, spatially resolved observations across a broad range of wavelengths are important for understanding the dynamical processes responsible for shaping the architecture and evolution of the disk. Examples of this phenomenon will be given in §4.2.4.

4.2 Observations of Debris Disks

Since their discovery in the 1980s, the accumulation of observational data for circumstellar debris disks has accelerated rapidly. In this section I'll review the progress and nature of imaging observations of debris disks. While the focus of this section will be on images and their relation to AO coronagraphic study of circumstellar debris, spectroscopic studies have been important. Visible-light spectroscopy has identified a gaseous component to β Pic, and time-variability in spectral features have been used to infer the presence of cometary bodies falling into the star (e.g. Vidal-Madjar et al. 1994). Mid-infrared spectroscopy is particularly powerful in constraining the size and composition of circumstellar grains (e.g. Okamoto et al. 2004; Chen et al. 2006).

4.2.1 Unresolved Imaging

Debris disks are usually first detected by surveys designed to identify the excess thermal emission above the stellar photosphere at mid-IR wavelengths and beyond. As primordial disks transition to debris systems, the primordial gas dissipates and most of the warm dust leaves the inner few AU of the system. The emission from larger, cooler grains remains. Until the disks are resolved, photospheric excess systems remain as debris disk candidates because of the chance of superposition of dusty galaxies in the background. Although it flew more than two decades ago, the all-sky

survey of *IRAS* has a continuing legacy for detecting debris systems around nearby stars. While not as sensitive as modern instruments, the survey has been mined for emission from cool dust (particularly in the $60\ \mu\text{m}$ band). While covering less area, the more sensitive pointed observations of *ISO* and *Spitzer* have also added to the list of main sequence stars with infrared excesses. The re-analysis of *IRAS* and *ISO* data to detect the faintest emission has provided invaluable source lists for targeted coronagraphic follow-up, enabling the recent boom in scattered-light imaging of debris disks. In particular, the work of Silverstone (2000), Zuckerman & Song (2004), and Moór et al. (2006) have provided comprehensive lists of nearby debris disk candidates.

Spitzer has been productive in debris disk observation. With its superior sensitivity, it has been expanding the known population of debris disks around A stars through various imaging surveys (Bryden et al. 2006; Su et al. 2006). It has also made significant progress in characterizing disk evolution, by surveying young stellar populations in nearby associations and clusters (Low et al. 2005; Sicilia-Aguilar et al. 2006; Stauffer et al. 2005; Gorlova et al. 2006; Hernández et al. 2006; Shvonski et al. 2006; Hernández et al. 2007; Siegler et al. 2007; Monroe et al. 2007). Some programs, such as the Formation and Evolution of Planetary Systems (FEPS) survey (Meyer et al. 2006), have also been discovering new debris systems through searches of nearby field stars (e.g. Kim et al. 2005).

Millimeter and sub-millimeter imaging can detect cool emission from grains in debris disks. As with *ISO* and *Spitzer*, surveys at these wavelengths require pointed observations. Previous works have measured unresolved emission from many debris disks, though only a few have been spatially resolved (§4.2.3). Such data can be used to compute the mass in large grains detected at these wavelengths. Typically this is done by assuming the grains are at a single (color) temperature, such that

$$M = \frac{F_\nu d^2}{\kappa_\nu B_\nu(T)}, \quad (4.16)$$

where d is the distance to the system, and κ_ν is an assumed dust opacity. Several such surveys have been conducted of stars with excesses previously identified by far-IR surveys (e.g. Zuckerman & Becklin 1993; Sylvester et al. 1996, 2001; Holmes et al.

2003; Williams & Andrews 2006). Others have been conducted focusing on stars of given spectral class, allowing the study of the evolution of dust mass with age (e.g. Carpenter et al. 2005; Lestrade et al. 2006). Young moving groups and associations provide attractive samples for these studies (e.g. Liu et al. 2004). Significant study in this direction will be made by the SCUBA-2 Unbiased Nearby Stars survey, which will search for debris disks around 500 nearby A–K type stars (Matthews et al. 2007).

4.2.2 Scattered Light Imaging

Some of the most spectacular results from debris disk studies are scattered-light images. A few disks have been detected in scattered light in seeing-limited observations. These are β Pic (e.g. Kalas & Jewitt 1995), AU Mic (Kalas et al. 2004), and HD 32297 (Kalas 2005). Tables 4.1 and 4.2 list space-based and AO observations of scattered-light disks, respectively.

These studies' most important results are in measuring the structures of debris disks at high spatial resolution. Notable structures include a secondary inner disk around β Pic (e.g. Golimowski et al. 2006) and substructure in the midplane of AU Mic (e.g. Chap 5). Two common architectures are extended disks (like β Pic) and ring-like systems (e.g. HR 4796A and HD 139664). Scattered-light imaging has also revealed several types of asymmetry in disks; some of these arise from a combination of viewing geometry and scattering effects, while others can be linked to asymmetries in the distributions surface density and grain properties (e.g. Kalas & Jewitt 1995; Fitzgerald et al. 2007a). As seen in the tables, several disks now have scattered-light colors, which is important for finding the smallest grains in the size distribution and thus providing constraints on grain removal processes (§4.2.4). Scattered light data also constrain grains through the measurement of the scattering phase function (usually via the asymmetry parameter g), and polarization data can independently constrain grain sizes, composition, and porosity (e.g. in AU Mic; Graham et al. 2007).

Table 4.1. Debris disks resolved in scattered light by space-based coronagraphs.

star	band(s)	instrument	reference
β Pic	0.2–1.0 μm	<i>HST</i> /STIS	Heap et al. (2000)
	<i>F435W</i> , <i>F606W</i> , <i>F814W</i>	<i>HST</i> /ACS	Golimowski et al. (2006)
AU Mic	<i>F435W</i> , <i>F606W</i> , <i>F814W</i>	<i>HST</i> /ACS	Krist et al. (2005)
	<i>F606W</i> (pol)	<i>HST</i> /ACS	Graham et al. (2007)
HD 32297	<i>F110W</i>	<i>HST</i> /NICMOS	Schneider et al. (2005)
HD 15115	<i>F606W</i>	<i>HST</i> /ACS	Kalas et al. (2007)
HR 4796A	<i>F110W</i> , <i>F160W</i>	<i>HST</i> /NICMOS	Schneider et al. (1999)
HD 92945	?	<i>HST</i> /ACS	Clampin (2005); Golimowski et al. (2007)
HD 107146	<i>F606W</i> , <i>F814W</i>	<i>HST</i> /ACS	Ardila et al. (2004)
HD 181327	<i>F110W</i>	<i>HST</i> /NICMOS	Schneider et al. (2006)
	<i>F606W</i>	<i>HST</i> /ACS	
Fomalhaut	<i>F606W</i> + <i>F814W</i>	<i>HST</i> /ACS	Kalas et al. (2005)
HD 139664	<i>F606W</i>	<i>HST</i> /ACS	Kalas et al. (2006)
HD 53143	<i>F606W</i>	<i>HST</i> /ACS	Kalas et al. (2006)
HD 10647	?	<i>HST</i> /ACS	Stapelfeldt et al. (2007)
HD 61005	<i>F110W</i>	<i>HST</i> /NICMOS	Hines et al. (2007)
HD 15745	<i>F606W</i>	<i>HST</i> /ACS	Kalas et al. (in prep.)

Table 4.2. Debris disks resolved in scattered light by adaptive optics coronagraphs.

star	band(s)	instrument	reference
β Pic	<i>R</i>	Las Campanas/AOC	Golimowski et al. (1993)
	<i>K'</i>	La Silla/COME-ON-PLUS	Mouillet et al. (1997)
	<i>K</i> (pol)	Subaru/CIAO	Tamura et al. (2006)
AU Mic	<i>H</i>	Keck/NIRC2	Liu (2004)
	<i>H</i>	Keck/NIRC2	Metchev et al. (2005)
	<i>JHK'</i>	Keck/NIRC2	Chap. 5; also Fitzgerald et al. (2007a)
	<i>L'</i>	Keck/NIRC2	Marois et al. (in prep.)
HD 15115	<i>JHK'</i>	Keck/NIRC2	Kalas et al. (2007)
HD 32297	<i>K</i>	Keck/NIRC2	Fitzgerald et al. (in prep.)
HR 4796A	<i>L'</i>	Keck/NIRC2	Marois et al. (in prep.)

4.2.3 Thermal Imaging

Resolved images of thermal emission are also very important for understanding the structure of debris systems. Table 4.3 lists systems for which resolved images of thermal emission exist. The primary result of such imaging is information about the spatial distribution of grains whose sizes are comparable to the observing wavelength. At long wavelengths (i.e. mm-regime), these grains often trace the larger particles taking part in a collisionally evolved size distribution. Often, the structure of the cold dust seen in the sub-mm is clumpy. Such clumpiness may arise due to stochastic release of long-lived dust clumps through collisions (Wyatt & Dent 2002), or through resonant trapping by a planet (e.g. Wyatt 2003). In the case of ϵ Eri, these clumps have been interpreted as arising from perturbations by a planet. The marginally detected orbital motion of the clumps provides evidence for this scenario (Greaves et al. 2005).

As seen in Table 4.3, the SCUBA camera on the JCMT has resolved a large portion of these disks at sub-mm wavelengths. The more sensitive SCUBA-2 camera promises to significantly expand the list of thermally resolved disks.

4.2.4 The Need for Multiple Wavelengths

As noted in §4.1, key motivations for observing debris disks include inferring the presence of planets and understanding the dynamical processes responsible for shaping the dust distribution. Large degeneracies in structural parameters are present when modeling these optically thin systems solely with their SEDs. A lack of 10–20 μm excess in the SED may indicate an inner hole (with an inner planet as a possible mechanism; e.g. Liou & Zook 1999; Moro-Martín et al. 2005), but the inferred hole size is degenerate with the unknown grain space, size, and temperature distributions.

Many structural degeneracies are broken with resolved imaging. Resolved images uncover features and asymmetries in the disk structure, and therefore probe unseen planets. When seen in scattered light at a single wavelength and certain viewing geometries, it is possible to directly detect the global architectural features

Table 4.3. Debris disks resolved in thermal emission.

star	band(s)	instrument	reference
Vega	60 μm	IRAS	van der Blik et al. (1994)
	60, 90 μm	ISO/ISOPHOT	Heinrichsen et al. (1998)
	850 μm	JCMT/SCUBA	Holland et al. (1998)
	1.3 mm	OVRO	Koerner et al. (2001)
	1.3 mm	IRAM/PdBI	Wilner et al. (2002)
	24, 70, 160 μm	<i>Spitzer</i> /MIPS	Su et al. (2005)
β Pic	11.9 μm	La Silla/TIMMI	Pantin et al. (1997)
	11.7, 17.9 μm (spec)	Keck/LWS	Weinberger et al. (2003)
	1.2 mm	SEST/SIMBA	Liseau et al. (2003)
	17.9 μm	Keck/MIRLIN	Wahhaj et al. (2003)
	10 μm (spec)	Subaru/COMICS	Okamoto et al. (2004)
ϵ Eri	8.7, 11.7, 12.3, 18.3, 24.6 μm	Gemini-S/T-ReCS	Telesco et al. (2005)
	850 μm	JCMT/SCUBA	Greaves et al. (1998)
	350 μm	CSO/SHARC II	Wilner et al. (2003)
	450, 850 μm	JCMT/SCUBA	Greaves et al. (2005)
	70 μm	<i>Spitzer</i> /MIPS	Marengo et al. (2005)
Fomalhaut	850 μm	JCMT/SCUBA	Holland et al. (1998)
	450, 850 μm	JCMT/SCUBA	Holland et al. (2003)
	24, 70, 160 μm	<i>Spitzer</i> /MIPS	Stapelfeldt et al. (2004)
HR 4796A	<i>N</i> , IHW18 (18 μm)	CTIO/OSCIR	Jayawardhana et al. (1998)
	20.8, 24.5 μm	Keck/MIRLIN	Koerner et al. (1998)
	12.5, 24.5 μm	Keck/MIRLIN	Wahhaj et al. (2005)
HD 32297	<i>N'</i>	Gemini-N/MICHELLE	Chap. 6; also Fitzgerald et al. (2007b)
	<i>N'</i> , <i>Qa</i>	Gemini-S/T-ReCS	Moerchen et al. (2007b)
HD 107146	450, 850 μm	JCMT/SCUBA	Williams et al. (2004)
η CrV	450, 850 μm	JCMT/SCUBA	Wyatt et al. (2005)
τ Cet	850 μm	JCMT/SCUBA	Greaves et al. (2004)
49 Cet	12.5, 17.9 μm	Keck/MIRLIN	Wahhaj et al. (2007)
ζ Lep	<i>Qa</i>	Gemini-S/T-ReCS	Moerchen et al. (2007a)

of the disk. However, degeneracies still remain. In particular, grain scattering properties are degenerate with their surface density distribution. This is especially true in systems seen near edge-on, as the surface brightness profiles cannot be inverted to find the surface density without first knowing the scattering phase function and efficiency. Furthermore, when seen in a single waveband, the grain size distribution is unconstrained. As seen in §4.1, many of the processes acting on the grains are size dependent, and will produce size-dependent spatial distributions. Such distributions are impossible to discern without multi-wavelength data.

Many of the same architectural degeneracies that are characteristic of scattered-light imaging are also present in thermal imaging (Moro-Martín et al. 2005, and references therein). In particular, at a single wavelength, the grain emissivity and surface density distribution are degenerate. Grain sizes, temperatures, and surface density cannot be untangled without color information.

When images at multiple wavelengths are modeled simultaneously, many of these degeneracies are broken. With scattered-light data at multiple wavelengths, the colors can be used to infer the grain sizes and scattering properties. With this comes constraints on the scattering phase functions, and therefore the spatial distribution of the grains of varying size can be recovered. Note that polarization information can also decouple the scattering properties from the spatial distribution. When combining resolved thermal imaging at multiple wavelengths, the color temperature can be used to infer grain sizes, temperatures, and emissivities. These are decoupled from the surface density distribution. The combination of scattered-light data and thermal imaging is particularly strong when the data probe similar grain sizes. The grain albedos can be computed (giving compositional information), and the multiple constraints on absorption and scattering efficiencies and scattering phase functions can be used to simultaneously constrain the spatial distribution of grains of different size. We can then make significant inroads on the composition and structure of the grains (e.g. porosity). When the thermal and scattered-light imaging probe grains of different size, we gain information on the dynamical processes responsible for producing and disseminating grains throughout the disk.

As an example of how multi-wavelength imaging can probe different grain struc-

tures in the disk as well as break degeneracies in inferred grain properties, consider the case of Fomalhaut. Sub-millimeter maps of the dust thermal emission at 350, 450, and 850 μm reveal an inclined ring morphology, with asymmetric emission between the two ansae (e.g. Holland et al. 2003; Marsh et al. 2005). *Spitzer* has imaged the disk at 24, 70, and 160 μm (Stapelfeldt et al. 2004). The 70 and 160 μm images show an inclined ring similar to the sub-mm maps; however the 24 μm emission reveals spatially resolved emission from grains interior to the ring, as well as an unresolved component centered on the star. These components are not seen in the longer-wavelength images, which is evidence for separate grain populations. When coupled with the 70 and 160 μm *Spitzer* data, the line-of-sight optical depth map derived from the 350 μm image shows evidence for a displacement of the SSE ansa toward the star (Marsh et al. 2005). The thermal data show enhanced emission in the SSE lobe relative to the NNW. Both of these findings are consistent with the effect of pericenter glow caused by perturbations from an eccentric planet (Wyatt et al. 1999). The disk was imaged in scattered light by Kalas et al. (2005). These data show a striking geometrical offset of an inclined ring displaced from the star, with a sharp inner ring boundary at 140 AU from the ring center and a steep dropoff beyond this distances. This distance is somewhat coincident with boundaries derived from modeling far-IR and sub-mm emission. Based on the 850 μm image, Dent et al. (2000) find a sharp outer cutoff at 140 AU, with an inner boundary of ~ 100 AU. In contrast, the modeling of Marsh et al. (2005) for the data at from 70–350 μm , find an inner radius of 113 AU and an outer boundary at 240 AU. Note that the structure of the large-grain ring differs from models based on marginally resolved far-IR observations that predict a shallow density profile from 22–430 AU (Harvey et al. 1996).

Taken together, the data over a wide range of wavelengths probe the characteristics of grains in the disk, especially their size-dependent spatial distributions. Modeling of the thermal emission predicts grain sizes in the ring of ~ 100 μm (Dent et al. 2000; Stapelfeldt et al. 2004), and these sizes are consistent with the low scattering asymmetry inferred from the optical image ($|g| \sim 0.2$; Kalas et al. 2005). While size-dependent spatial distribution of grains has yet to be dynamically mod-

eled using all available data, conclusions have been drawn regarding the processes responsible for dust production and diffusion. The primary result is that the dust grains in the ring are in secular resonance with an eccentric planet. This is inferred independently through modeling of the optical depth from multi-wavelength thermal emission as well as from the scattered-light image. The sharp inner edge of the scattered-light disk has been used to infer the mass and eccentricity of the forcing planet (Quillen 2006). The grains in the ring are likely replenished by collisions, and P-R drag is dynamically unimportant. For the region interior to the ring, the resolved portion of the $24\ \mu\text{m}$ image and $20\text{--}30\ \mu\text{m}$ spectrum of Stapelfeldt et al. (2004) are consistent with a r^{-1} density distribution, and inward drift from the ring. However, the unresolved portion suggests there may be an additional source of grains nearer to the star. More observations are needed to constrain this separate grain population.

4.3 Adaptive Optics Coronagraphy for Circumstellar Debris

Adaptive optics coronagraphy enables the study of debris disks in the optical/IR region of the spectrum at high spatial resolution. This is currently important, since the workhorse instrument aboard *HST*, the Advanced Camera for Surveys (ACS), is now non-functional (the somewhat less-sensitive NICMOS near-IR coronagraph is still working, however). In terms of spatial resolution, the use of ground-based adaptive optics coronagraphs will therefore bridge the gap between the current and next generation of space coronagraphs, such as those aboard the *James Webb Space Telescope*.

Space-based coronagraphs have made prolific contributions to the study of debris disks. As discussed in Chap. 2, the stability of the space-telescope PSF enables superior contrast relative to ground-based scattered-light observations. This is particularly evident with the unparalleled sensitivity of *HST/ACS*. Ground-based sub-mm observations have also been important in resolving disk structures, although the spatial resolution is relatively poor and sensitivity is background-limited. Both

of these facts are illustrated in Tables 4.1 and 4.3. Despite the success of optical scattered-light imaging and resolved sub-mm observations, there are opportunities for scientific impact for near-IR scattered-light observations. As discussed in §4.2.4, the combination of scattered-light colors over a broad wavelength range and resolved thermal emission can act in synergy to uncover the physical processes shaping the disk architecture and evolution. Additional observations of resolved disks in the near-IR, either from *HST*/NICMOS or ground-based AO coronagraphs, are sorely needed to characterize the range of architectures and dynamical processes governing the evolution of debris.

Ground-based AO coronagraphs have gradually increased their scientific contributions to debris disk studies in the past decade (Table 4.2). Early efforts were directed at imaging the disk of β Pic, with tip/tilt compensated coronagraphy (Golimowski et al. 1993) and adaptive optics coronagraphy (Mouillet et al. 1997). More recently, the disk has been measured in polarized light with an AO coronagraph (Tamura et al. 2006). These latter data have been fit with a model for the size and space distribution of compact silicate grains, which reproduce the *BVR**IK* polarization fraction (Krivova et al. 2000; Tamura et al. 2006). Further, the *K*-band polarization data show a dip in polarized fraction at 100 AU, which indicate the location of a gap in the dust distribution. Such a gap is difficult to discern in total intensity because the forward scattering from grains in the outer regions of the disk fill in the light near the dip. This gap is also just inside the location of surface brightness profile inflections, which may arise from a boundary due to ice sublimation (Golimowski et al. 2006). The adaptive optics of both Mouillet et al. (1997) and Tamura et al. (2006) show evidence for fluctuations (“ripples”) in the total intensity between 50–120 AU, which are interpreted as arising from multiple planetesimal belts (similar to those inferred from mid-IR data; Wahhaj et al. 2003; Okamoto et al. 2004).

The disk around AU Mic has also been the focus of modern AO coronagraphs, with imaging by Liu (2004); Metchev et al. (2005), and myself (Chap. 5). While the scientific results will be detailed in a later chapter, I note here the power of AO coronagraphy to reveal the substructure present in the disk brightness profiles, and the complementarity of AO coronagraph and space-based imaging to constrain the

spatial distribution of grain properties and the underlying dynamics. The edge-on disk of HD 15115, recently published by Kalas et al. (2007), was imaged with the Keck AO coronagraph, based on techniques in this work. The *HST* imaging initially revealed the near-edge-on, highly asymmetric disk. Adaptive optics coronagraphic follow-up was crucial in confirming the presence of this disk (which might have been a strange instrumental artifact). The ground-based data are able to probe the disk closer to the star than in the optical, showing power-law profiles in the inner disk. These data imply any planetesimal belts must lie closer to the star than has been imaged to date. The asymmetric structure revealed by the imaging data require theoretical explanation; hypotheses include close passage by a bound stellar companion and eccentricity pumping by an inner planet. More work is needed to model the observed images in terms of disk architecture and color for the purpose of constraining grain characteristics and dynamics.

Given the technical importance of adaptive optics coronagraphs for the study of debris, what scientific questions is the technique best suited to address? On their own, these are largely the same as those addressed by space-based coronagraphy. The high spatial resolution and ability to constrain grain properties permit inferences of the dynamical processes governing the evolution of the solid material, as well as the distribution of planets and planetesimals. For a full accounting of the dynamical processes involved in the evolution of solid material around stars, AO coronagraphic images should be augmented by multi-wavelength observation, for the reasons outlined in §4.2.4. With the absence of a visible light coronagraph on *HST*, adaptive optics coronagraphy can potentially provide the greatest spatial detail in the architecture of debris disks. A critical path to understanding the dynamical structure responsible for the structure lies through the nature of the grains. Because AO coronagraphy is currently well-suited to measuring scattered light in the near IR at high spatial resolution, we sample the grain scattering properties at these wavelengths. When combined with scattered light images in the visible (e.g. from space-based coronagraphs) or with mid-IR resolved imaging and spectroscopy, we can begin to disentangle grain space and size distributions, porosity, and composition. These grain properties can then be used to glean information about the forces

and processes responsible for distributing the debris throughout the disk. With a detailed accounting of the dynamical processes, we are in a position to test hypotheses regarding the presence of planets and potentially test their migration histories.

As discussed in Chapter 2, there are substantial challenges to achieving the contrast needed for imaging debris disks from the ground. The brightest disks scatter a fraction of the starlight $L_{\text{sca}}/L_* \sim 10^{-3}$ (e.g. β Pic). This scattered light is distributed over the extent of the disk, and the surface brightness depends on the viewing geometry and distance to the system. Because they are optically thin, the brightest disks are near edge-on. This scattered light must be detected in the presence of the PSF halo, and as noted in §2.1, the stability of the PSF can severely limit the detectability of faint emission, especially when the disk is oriented near face-on. These considerations strongly bias the range of disk viewing geometries achievable from the ground. Because of the relative inability to distinguish face-on disks from the residual seeing halo (present in all ground-based images), such studies of debris disks are limited to those with inclinations near edge-on. Even with favorable geometries, it is still no easy task to distinguish a debris disk from the fluctuating image of the star.

The success of adaptive optics coronagraphy relies on suitable observing and data reduction techniques. The faintness of the scattered light requires that the stellar PSF be subtracted. Differential measurements are gained either by subtracting a reference PSF observation, or by using the observations themselves in a self-subtraction scheme. One such differential method is that of Simultaneous Differential Imaging (SDI; e.g. Marois et al. 2000), which uses the wavelength scaling of the PSF to subtract simultaneous observations at two or more wavelengths. This method has been implemented at the CFHT and VLT, and has been directed toward faint companion searches (Marois et al. 2005; Biller et al. 2004). Integral field spectrographs, while currently uncommon on adaptive-optics-equipped telescopes, have the potential to make efficient use of the SDI technique (e.g. Thatte et al. 2007). The use of this method for imaging debris disks is challenging due to their extended nature, though instruments like the Gemini Planet Imager, using integral field spectrographs, have their detection as primary science goals (Macintosh et al.

2006).

To date, the most powerful class of differential techniques for self-subtraction of AO coronagraphic images is that of roll subtraction, which have been successful in resolving near-edge-on disks from the ground. Indeed, β Pic, AU Mic, HD 32297, and HD 15115 (from Table 4.2) all have such viewing geometries. In a general form of this scheme, an alt-az telescope is used without the aid of an instrument rotator. The PSF maintains a fixed orientation on the detector, while the image of the sky rotates with parallactic angle. This allows the frames to be combined to obtain estimates of the PSF in each image. After subtraction, the residuals are rotated to a common frame and combined. These methods are useful for finding faint point sources and edge-on disks. Self-subtraction techniques are not well-suited for face-on disks. Past uses of roll subtraction for disks include AU Mic (Liu 2004), HD 15115 (Kalas et al. 2007). An advanced form of the technique, called Angular Differential Imaging (ADI; Marois et al. 2006; Lafrenière et al. 2007a), has been applied to point source searches (Lafrenière et al. 2007b) and has successfully imaged debris disks (C. Marois, priv. comm.). I will detail my technique for roll subtraction with AO coronagraphy in §5.2.2.

Chapter 5

The AU Microscopii Debris Disk

5.1 Introduction

Contemporary work has revealed an exciting laboratory for the detailed study of circumstellar debris. AU Microscopii (GJ 803) is a nearby star that harbors an optically thin debris disk. The spectral type in the literature ranges from dM0–2.5Ve (Joy & Abt 1974; Linsky et al. 1982; Keenan 1983; Gliese & Jahreiss 1995). It is a member of the β Pictoris moving group, and as such is one of the youngest (12_{-4}^{+8} Myr; Barrado y Navascués et al. 1999; Zuckerman et al. 2001) and among the closest (9.94 ± 0.13 pc; Perryman et al. 1997) of the known resolved debris disks. It is especially attractive to study in the larger context of disk evolution as a function of stellar mass. In terms of mass, M dwarfs like AU Mic constitute the dominant stellar component of the Galaxy. Despite the abundance of such stars, AU Mic is currently unique among the resolved debris systems. It is a touchstone for studying the evolution of circumstellar disks around low-mass stars. AU Mic has a well-chronicled history of flare activity (e.g. Robinson et al. 2001). It is likely that strong stellar activity has a significant effect on dust dynamics and lifetimes (Plavchan et al. 2005). Notably, we can make direct comparisons across spectral types given AU Mic and its sibling β Pic, the archetypal A star with an edge-on debris disk.

The scattered light of the dust around AU Mic was discovered by Kalas et al. (2004), who used seeing-limited *R*-band coronagraphic imaging to resolve it into an

extended, near-edge-on disk. Additional high-resolution studies followed, with adaptive optics (AO) observations at H -band by Liu (2004, hereafter L04) and Metchev et al. (2005, hereafter M05), as well as in the visible with the *Hubble Space Telescope* (*HST*) by Krist et al. (2005, hereafter K05). These detailed images reveal a very thin midplane (FWHM ~ 2 AU) with an inner disk closely aligned with the line of sight ($\theta \sim 0.5^\circ$ for $r < 50$ AU; K05). The midplane surface brightness profiles show a break around 35–45 AU, with brightness decreasing more sharply at larger projected distances. There are slight asymmetries in the overall brightness of the profiles between the two disk ansae. Further, the midplane exhibits substructure on smaller scales, including localized enhancements and deficits in brightness, and vertical deviations of midplane positions away from that of a uniform disk. Comparison of these structures between datasets is required to confidently reject image processing artifacts. The origin of the small-scale structure remains unexplained. A striking feature of the scattered light disk is its color. K05 found a blue color in the visible with *HST*, along with an apparent color gradient — the disk is increasingly blue from 30–60 AU. The disk is also blue from the visible to the H band, as noted by M05. This is unlike many of the disks resolved to date, which are neutral or red scatterers like β Pic (Golimowski et al. 2006; Meyer et al. 2007). We note, however, that two other recently imaged disks, HD 32297 (Kalas 2005) and HD 15115 (Kalas et al. 2007), also scatter blue between the optical and near-IR. Such data are important because images at each new wavelength serve to further constrain the sizes, composition, and structure of grains through analysis of their scattering properties.

While the scattered light imaging of the disk has attracted attention in the past few years, there has also been significant study of the grains’ thermal emission in the SED. The cold dust around AU Mic was first identified by the *Infrared Astronomical Satellite* (*IRAS*), as excess emission at $60\ \mu\text{m}$ was weakly detected (Mathioudakis & Doyle 1991; Song et al. 2002). Recently, sensitive measurements of the $850\ \mu\text{m}$ flux confirmed the presence of cold dust around the star (Liu et al. 2004). The *Spitzer Space Telescope* has further constrained the thermal emission of the dust in the mid-IR (Chen et al. 2005).

Results of these studies have been taken as indirect evidence for the presence

of planets around the star. The gravitational influence of such planets provides a possible mechanism for generating the substructure in the disk. In particular, mean-motion resonances from a planet can trap dust to produce radial, azimuthal, and vertical structure (e.g. Ozernoy et al. 2000; Wahhaj et al. 2003; Thommes & Lissauer 2003; Wyatt 2006), though to date, no models of these mechanisms have been applied to the substructure of AU Mic. Further, the shallow surface brightness profiles in the inner disk and lack of thermal excess in the 10–20 μm region of the SED have suggested an inner clearing of dust, perhaps maintained again by the presence of an inner planet (e.g. Roques et al. 1994; Moro-Martín & Malhotra 2005). Nonetheless, it is imperative to understand the detailed physics affecting the distribution of dust grains around this disk prior to establishing the presence of unseen planets. The gravity of such perturbers is just one of many effects which may shape the dust distribution, including grain-grain collisions, forces from both stellar radiation and wind, and gas drag. Because the disk is along the line-of-sight to the star, AU Mic is a favorable target for using absorption spectroscopy to search for remnant gas in the disk. Roberge et al. (2005) placed limits on the column of H_2 toward the star using the *Far Ultraviolet Spectroscopic Explorer (FUSE)*, concluding that giant planets were unlikely to have formed given the rapid dissipation of primordial gas. Different groups have placed planet detection limits around the star in very narrow ($r < 2'' \approx 20 \text{ AU}$; Masciadri et al. 2005) and slightly wider fields (Neuhäuser et al. 2003; M05), and to date none have been directly detected. Certainly the question of planets in this system warrants further study, as these different lines of evidence have not been resolved.

Comprehending the physics that sculpt the dust distribution in this debris disk remains a key step for not only determining the existence of planets, but also for informing us about the evolution of solid material around stars in general. Augereau & Beust (2006) and Strubbe & Chiang (2006, hereafter SC06) have both investigated the observed break in the midplane surface brightness profile and color gradient in the outer disk, and hypothesize that a ring of parent bodies (near the break in surface brightness profile) acts as a source of dust grains, which are subsequently swept outward by a strong stellar wind. SC06 provide a detailed physical model for AU Mic

for this scenario. The steady-state spatial and size distributions of dust grains are determined by a small set of physical processes (e.g. collisions, radiation, wind, etc.), and with other assumptions about grain properties, the model can reproduce observations of scattered light profiles and the SED.

As illustrated by the work done to date, we have constraints on the distribution of dust using scattered light images coupled with the SED. However, in this edge-on system, a degeneracy remains between the scattering properties of grains and their supposed spatial distribution. The advantage of measurements in polarized light, rather than total intensity, is that they give complementary information in the grain scattering properties (for grain sizes a such that $x \simeq 2\pi a/\lambda \sim 1$) and thus reduce this degeneracy. The polarization properties of AU Mic's disk have recently been measured with *HST*/ACS by Graham et al. (2007). The disk exhibits strong gradients in linear polarization, and their modeling of the flux of polarized visible light indicates the presence of small porous grains and an architecture consistent with a significant ($>300:1$ in vertical optical depth to scattering) inner clearing.

In this chapter, we report and analyze multiband AO observations of the scattered light disk of AU Mic in the near IR. Our high-contrast images were processed with a novel data reduction technique which aims to mitigate the effects of point-spread function variability on ground-based observations. We report on the observed colors and color gradients of the disk brightness profiles for our images, and also for reprocessed *HST* data previously presented by K05. Guided by the recent characterization of grain scattering properties by Graham et al. (2007), we simultaneously fit a dust model to near IR and visible scattered light data as well as the SED. With this model of dust distribution, we then check the consistency of SC06's physical model for the disk architecture with our empirical results. We examine the question of whether the inner disk is populated, as expected if corpuscular drag forces can draw grains inward before they are pulverized through collisions. We document our observational and data reduction techniques in §5.2; we present our observational results in §5.3 and analyze dust models in §5.4. Discussion and conclusions follow in §5.5.

5.2 Observations & Reduction

The achievable spatial resolution is a prime motivator for imaging debris disks in the optical and near infrared — resolved images here highlight structural details and dust properties. However, at these wavelengths the star overwhelms the light scattered by the circumstellar debris. This contrast ratio characterizes a fundamental observational challenge in such studies of debris systems. To meet this challenge, we use AO to concentrate the star’s light and employ a coronagraph to occult the resulting stellar image, thereby increasing sensitivity to the disk. Here, we detail our use of AO coronagraphy and image processing techniques to study the circumstellar dust (§5.2.1–5.2.2). We describe calibration of the AO data in §5.2.3, and our use of *HST* images in §5.2.4.

5.2.1 Near Infrared Imaging

We observed AU Mic on the nights of 2004 Aug 29-30 with the Keck II AO system and a coronagraphic imaging mode of the NIRC2 camera. AU Mic is sufficiently bright to serve as its own reference for adaptive wavefront correction. After wavefront compensation, the on-axis starlight is blocked by a focal-plane mask. Diffraction effects are then suppressed by a pupil-plane Lyot stop, and the light is reimaged onto a 1024×1024 pixel Aladdin detector. The narrow-field mode of the camera was used, at a scale of ≈ 10 mas pixel⁻¹. Exposure times were 30–60 s in *JHK'* (60×1 s in *L'*), and the filter was cycled after a few short exposures in each band. Exposures where the disk was aligned with a diffraction spike were discarded. The filters, total integration times, and focal masks are listed in Table 5.1. We used a $0''.5$ radius focal plane mask on the second night, however the data in the region around the edge of this mask were discarded due to large residual subtraction errors. Calibration employed standard bias subtraction and flat fielding techniques.

Imaging faint circumstellar material requires suppression of the stellar light, whose distribution is given by the on-axis point spread function (PSF). While the coronagraph suppresses much of the starlight, a fraction leaks through the system and must be subtracted from the data in post-processing. The relative success

Table 5.1. Observations of AU Mic

night	band	r_{mask} (")	T (s)	ΔPA ($^{\circ}$)
2004 Aug 29	J	0.75	600	16.9
	H	0.75	690	49.8
	K'	0.75	1110	40.5
2004 Aug 30	J	0.50	570	39.0
	H	0.50	600	34.5
	K'	0.50	1260	45.6
	L'	0.50	720	43.6

Note. — The radius of the coronagraphic focal plane mask is given by r_{mask} . Filters were cycled after a few short exposures in each band. Here, T is the total integration time and ΔPA is the total amount of field rotation over the course of the exposure sequence in that band.

of this operation is linked to PSF stability. In observations through an altitude-azimuth telescope like Keck, the image plane rotates relative to the telescope with parallactic angle. However, features in the PSF that are produced by the telescope (e.g. diffraction spikes) maintain a fixed orientation relative to it. We disabled the instrument rotator of NIRC2 to additionally fix the orientation of any features arising from camera aberrations. With the disabled rotator, the PSF orientation is fixed relative to the detector while the edge-on disk appears to rotate around the stellar image with time. This allows us to disentangle the image of the disk from features in the diffraction pattern of the star, as well as use the stable orientation of the stellar PSF on the detector for more accurate subtraction. “Roll subtraction” is a general observational methodology that has been applied with success to AO imaging of circumstellar disks (e.g. L04; M05). An account of our version of the roll subtraction technique follows.

5.2.2 PSF Subtraction Technique

The time variability of the AO PSF is often the limiting factor in detecting faint circumstellar material from the ground. Rather than subtracting the stellar PSF from non-contemporaneous observations of reference stars, we wish to directly exploit information from the science target exposures. Techniques developed by Véran et al. (1997a) and Sheehy et al. (2006) seek to model the AO system to estimate the PSF, using telemetry data and crowded field imaging, respectively. However, these techniques do not yet have demonstrated applicability to high-contrast imaging. For roll subtraction, mitigation of AO PSF variability can potentially improve contrast. We note in particular the technique’s advancement in this regard by Marois et al. (2006) for the case of point source detection.

We developed an algorithm suited to the self-subtraction of time-varying AO PSFs and applied it to the reduction of our near-IR images. In essence, because the PSF remains in a fixed orientation while the edge-on disk rotates, one may use PSF information spanning several exposures to estimate the stellar PSF (effectively removing the disk). Our refinement to the procedure is to estimate the PSF for each exposure, rather than for the ensemble. The PSF estimates are then used to

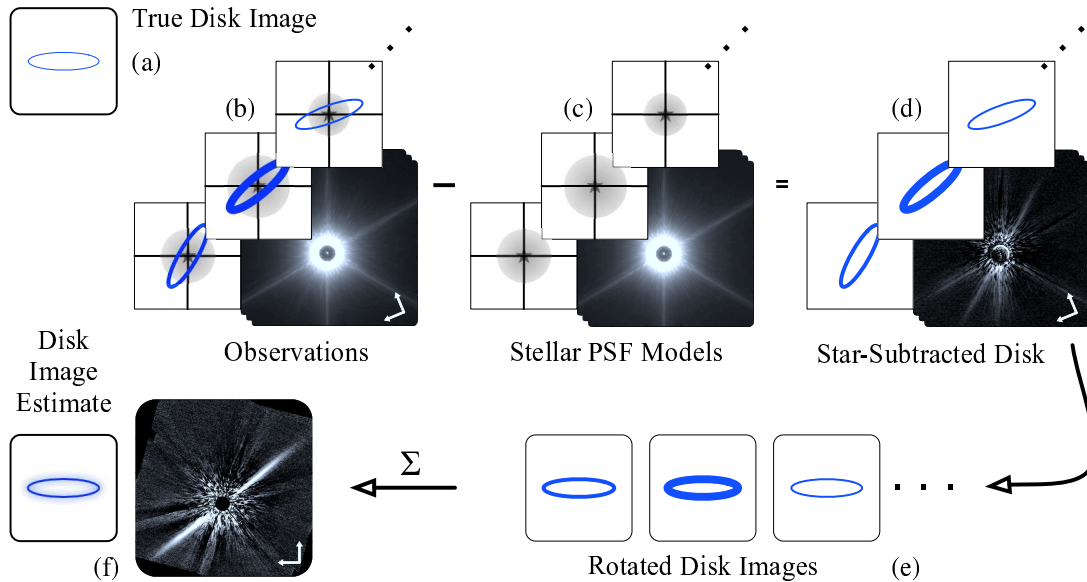


Figure 5.1 The roll subtraction process, which estimates the image of the disk in the presence of a fluctuating stellar PSF. The disk (a) is observed on an alt-az telescope with no image de-rotation (b). The PSF is fixed relative to the detector while the disk image rotates due to sidereal motion. The observed disk images are blurred by different amounts by the time-varying PSF, illustrated by different line weights the disk images and the size of the circular stellar halo. Estimates of the PSF scaled and positioned to match the stellar image (c) are subtracted from the observations, leaving residual disk images (d). These images are transformed to a common frame (e) and combined to estimate the disk image (f).

subtract the stellar image from each frame. The residuals are transformed to a common sky orientation and then combined to estimate the star-subtracted object field (Fig. 5.1), corresponding to the disk emission. We detail our procedure, including the refinements for tracking changes in the time-variable AO PSF, here.

In general, the long-exposure AO PSF is a non-trivial function of atmospheric turbulence fluctuations, filtration by closed-loop AO, and additional quasi-static wavefront errors arising from the optics in the system (“static speckles”). With the PSF structure arising from these effects in mind, we built an empirical model of the

PSF for each exposure, and then used these models to optimally subtract the stellar image. Our proposed deconstruction hinges on the removal of the radial profile from each image. It is much more challenging to remove the stellar profile from images with face-on disks. The procedure outlined here is most-suited for imaging edge-on disks from the ground.

PSF Model

The ideal model PSF will reproduce the response of the imaging system to the starlight which has been occulted by the coronagraph. For our subtraction problem, we are interested in estimating the structure of the stellar PSF’s outer regions — outside of any coronagraphic focal-plane mask. For the moment, we ignore the focal-plane mask and consider only the case of a monochromatic image of an on-axis star. We approximate the adaptively corrected long-exposure point spread function $S(\mathbf{x})$ as the convolution (\star) between a “static” PSF and a blurring kernel encompassing the time-variable wavefront errors (e.g. Véran et al. 1997a),

$$S(\mathbf{x}) \approx S_s(\mathbf{x}) \star \Lambda(\mathbf{x}). \quad (5.1)$$

Here, $\Lambda(\mathbf{x})$ is determined by the variable wavefront errors of partially corrected atmospheric turbulence which, depending on correction level, has a characteristic width $\lesssim \lambda/r_0$ (where r_0 is the Fried length). $S_s(\mathbf{x})$ is the PSF that would arise solely from time-independent wavefront errors. For a circular pupil of diameter D with no obscurations or wavefront errors, $S_s(\mathbf{x})$ is the diffraction-limited Airy pattern of characteristic width $\sim \lambda/D$.

With good AO correction, the structure of the long-exposure PSF is characterized by a diffraction-limited core and a seeing-disk halo. Features like diffraction spikes and individual speckles also play an important role in the structure. To further motivate our model, we first decompose the static PSF into the sum of its Airy core ($\theta < 1.22\lambda/D$) and all other static speckles ($\theta > 1.22\lambda/D$),

$$S_s(\mathbf{x}) = S_{s,c}(\mathbf{x}) + S_{s,sp}(\mathbf{x}). \quad (5.2)$$

Note that since the core is sharply peaked relative to the halo scale in the blurring kernel ($\lambda/D \ll \lambda/r_0$), $S_{s,c}(\mathbf{x}) \star \Lambda(\mathbf{x})$ is approximately proportional to Λ itself; the

scale factor α is related to the Strehl ratio. For computational simplicity, we treat the blurring effect of $\Lambda(\mathbf{x})$ on $S_{s,sp}(\mathbf{x})$ by a scalar factor β , which also correlates with correction level — decreased blurring increases peak speckle intensity. Further approximating (5.1), we have

$$S(\mathbf{x}) \sim \alpha\Lambda(\mathbf{x}) + \beta S_{s,sp}(\mathbf{x}). \quad (5.3)$$

We have simplified the PSF from a convolution of static and atmospheric terms (Eq. 5.1) to a linear combination (Eq. 5.3), and we now seek to increase computational efficiency further. First, we note that with this linear combination, it is straightforward to generalize to wide-band imaging since Λ and $S_{s,sp}$ can each be represented by a linear combination of quasi-monochromatic PSFs. Second, although not strictly true under real conditions, we further assume that the blurring is symmetric in azimuth (ϕ). This leads us to isolate the azimuthally symmetric radial profile of each term in equation (5.3). For an exposure i , we estimate the image of the star as

$$\hat{S}_i(\theta, \phi) \equiv \rho_i(\theta) + \beta_i S'_{s,sp}(\theta, \phi), \quad (5.4)$$

with $S'_{s,sp}(\mathbf{x})$ given by $S_{s,sp}(\mathbf{x})$ with the radial profile removed and subsumed into the profile term $\rho(\mathbf{x})$.

We treat the coronagraphic focal mask in our model (Eq. 5.4) simply. *Prima facie*, the circular mask's suppression of the stellar image will be absorbed into ρ . Errors in centering the star behind the mask will result in additional leakage of light outside the spot via diffraction (Lloyd & Sivaramakrishnan 2005), an effect we ignore. These misalignments manifest themselves as subtraction errors in the vicinity of the mask edge.

A key requirement for our model is the profile-removed speckle map, $S'_{s,sp}(\mathbf{x})$. In practice, we use the target images themselves to construct $S'_{s,sp}(\mathbf{x})$. We remove the radial profile from each image, mask out the region around the (rotating) edge-on disk, and combine the results to form the speckle map. We additionally mask the the diffraction spikes from each image when estimating the radial profiles ρ_i , because the spikes' blurring (which we treat only by a scale factor β) can bias the profile estimates. In practice, we mask the disk with a $0''.5$ -wide strip, and the spikes with

regions that are $1''.6$ wide, tapering inward for $\theta \leq 5''$. With $\rho_i(\mathbf{x})$ and $S'_{s,sp}(\mathbf{x})$ in hand, the PSF model for each image is parametrized solely by β_i , which scales the speckle map.

Subtraction Procedure

We subtract the model PSF \hat{S}_i from each image. The map scale parameter β_i and a registration offset are tuned to minimize subtraction residuals, which are rotated to a common frame and combined to form the image of the disk.

Special software masks are used in various stages of the subtraction process. Diffraction spikes and the edge-on disk were masked during calculation of the radial profile. The disk was also masked from individual frames before they were combined to form the speckle map. Diffraction spikes, the focal plane spot, and the disk were excluded from consideration during the least-squares optimization of the PSF model subtraction. Finally, diffraction spikes were masked from the subtraction residuals before they were combined to form the final disk image.

In summary, the sequence is to

1. register each frame to a fiducial position using stellar centroid estimates,
2. mask the diffraction spikes and the disk, then extract the radial profile about the fiducial point (ρ_i),
3. remove the profile and combine the residuals from each image to obtain the speckle map ($S'_{s,sp}$),
4. construct a PSF model for each image, using a scaled speckle map ($\beta_i S'_{s,sp}$) and the radial profile (ρ_i),
5. use an optimization method to subtract PSF model from image, solving for stellar position and speckle map scale (β_i),
6. repeat the process from step (1) using updated centroid estimates if not in final iteration,

7. mask diffraction spikes, rotate the subtraction residuals into the sky's frame, and combine to form the disk image estimate.

We find that, for these data, three iterations of this process is enough for convergence to visually detectable levels.

Technique Comparison

The subtraction procedure described in the previous sections is compared with similar implementations in Figure 5.2. In panel (a), we follow the steps we outlined above. In panel (b), we restrict the model fitting process so that the scale of the speckle map (β_i) is fixed and only offsets were optimized. Finally, in (c) we discard the PSF models altogether and fit the offset and scale of an average PSF. No spike or object masking were used when combining residual images in (c). In panel (d) we display curves of annular *rms* (corresponding to the photometric errors shown in Figure 5.6), excluding the regions near the disk. These curves show that fitting the speckle scale gives modest contrast gain ($\lesssim 0.1$ mag), while larger gains are obtained when removing the radial profile of the observations prior to combination (~ 0.5 mag).

5.2.3 Calibration

Immediately after bias subtraction and flat fielding, we corrected the camera's geometric distortion in each image. However, no attempt was made to calibrate for the scale and orientation of the detector on the sky, as any differences from nominal values are expected to be minor. When visually comparing with *HST* imaging (§5.2.4), we found a 0.1° rotation between the two sets.

Our calibrations for photometry require measurement of zero point and PSF. We bracketed our observations of AU Mic with photometric standard stars SJ 9170 and HD 205772 on the first night, and GJ 811.1 on the second (Elias et al. 1982; Persson et al. 1998). These observations were used to determine the photometric zero point in each band. The stars were positioned outside the coronagraphic spot, and aperture photometry was used to measure the stellar brightness. Since large aperture radii

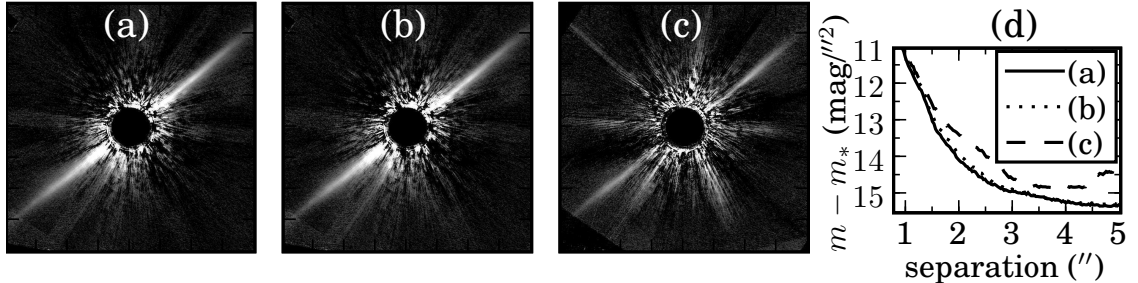


Figure 5.2 A comparison of different methods of roll subtraction. Panel (a) shows the resulting image from the technique described in §5.2.2. Panel (b) is the same as (a), except the scale of the speckle map is not optimized (§5.2.2). For comparison, panel (c) registers an average PSF to each image, rather than fitting a PSF model. Each of these images is $8''$ on a side. In (d), we show the annular *rms* (excluding the disk) of photometry in $0''.1 \times 0''.5$ apertures as a function of radius for subtractions shown in (a)-(c). At a radius of $2''$, curve (b) is 0.56 mag more sensitive than (c), while (a) is 0.16 mag more sensitive than (b). The gain in contrast when subtracting the profile highlights the suitability of the technique for edge-on disks.

could be used on the well-exposed stellar images, no encircled energy corrections were used in determining zero points. For all measurements, we applied an airmass correction assuming extinction values appropriate for Mauna Kea (Krisciunas et al. 1987).

To measure the scattering properties of the dust, we express the disk flux relative to that of the star. However, measuring the brightness of AU Mic is a challenge with this instrumental configuration because it is too bright for direct unocculted imaging, while observations using the focal plane mask complicate calibration. Here we adopt 2MASS photometry for the stellar brightness ($J = 5.436 \pm 0.017$, $H = 4.831 \pm 0.016$, $K = 4.529 \pm 0.020$; Skrutskie et al. 2006). We ignore the small (\sim few centi-mag) color correction when transforming from K to K' , as we expect disk photometry to be dominated by other errors. To determine the brightness of the star in L' , we first measured the brightness of GJ 811.1 through the partially-transmissive focal plane spot in L . We then applied a color correction to compute the zero point (behind the spot) in L' , and measured the brightness of the AU Mic using the same

photometric aperture, finding 4.38 ± 0.04 mag in L' . We note that our attempts to express the relative disk and stellar flux ratio should take AU Mic's variability into consideration. The star regularly flares in the X-ray and EUV regions of the spectrum (for a review with application to grain dynamics, see Augereau & Beust 2006). Periodic variations in the visible regions of the spectrum, thought to be caused by spots ($\Delta m_V \sim 0.35$ mag, $P = 4.865$ d; Torres & Ferraz Mello 1973; Cutispoto et al. 2003), are also relevant. However, as noted by M05, for AU Mic these are likely not problematic since the contrast between spots and the photosphere is lower in the near IR.

It is convenient to measure surface brightness in rectangular photometric apertures, as are used in the calculations detailed in §5.3.2. Because of the difficulty in using coronagraphic observations to infer the off-axis (unobscured) PSF, we apply an aperture correction based on the enclosed energy in this aperture by using the unobscured observations of photometric standard stars as PSF references. In each band, we average the enclosed energy over azimuthal rotation of the reference PSF to simulate the final roll-subtracted image's PSF. The aperture corrections we derived from these enclosed energy measurements are susceptible to variability in the AO PSF because the reference PSFs are measured non-contemporaneously from those of AU Mic. To estimate the systematic errors in the overall flux levels, we examined the random error in the enclosed energy of the reference PSF exposures in each band. The largest fluctuation on a single night was 16%. Although the combination of data from both nights will reduce this uncertainty ($\lesssim 11\%$), the potential for unmeasured changes in the PSF from the reference star to science measurements remains. With caution in mind, we estimate the uncertainty in flux calibration error in the final near-IR images at 20% and note that, in general, unsensed fluctuations will tend to affect the shorter-wavelength observations to a greater degree. This systematic calibration uncertainty will affect the absolute levels of the surface brightness profiles we measure in §5.3.2, and depending on the degree in correlation between errors in calibration in different bands, the disk colors (§5.3.3). Measurements of color gradients will not be affected by this type of error.

5.2.4 HST Imaging

In order to compare disk images over a wider range of wavelengths, we reduced and analyzed data previously obtained with the *Hubble Space Telescope* Advanced Camera for Surveys in the *F606W* filter ($\lambda_c=606$ nm, $\Delta\lambda = 234$ nm) on 2004 April 03 (K05). We acquired the flatfield images of AU Mic and the PSF reference star HD 216149 from the *HST* OPUS pipeline. These data were further calibrated by dividing by an appropriate spotflat and multiplying by a pixel area map. A final image of AU Mic was constructed by averaging three frames of 750 seconds integration each, with appropriate filtering to reject cosmic rays. The final image of HD 216149 was constructed by averaging eight frames of 225 seconds each. We subtracted the PSF subtraction in a manner described by K05. There was no need to apply our specialized roll-subtraction technique (§5.2.2) to these data because of the stability of the ACS PSF. The PSF-subtracted AU Mic image was then corrected for geometric distortion using a custom IDL routine (J. Krist, private communication). We used the Tiny Tim PSF model¹ (Krist & Hook 2004) to compute the enclosed energy in rectangular apertures to enable comparison of surface brightness profiles with our near-IR data.

We used the same method for computing midplane surface brightness profiles described previously (§5.2.3). We checked the consistency of our *F606W* midplane surface brightness measurements against those reported in K05’s Fig. 4 (using their $0''.25 \times 0''.25$ apertures) and found that our measurements of the same data were uniformly 0.20 ± 0.05 mag brighter. The discrepancy is due to the fact that K05 divided their images by a factor of 1.124 when correcting their pixel areas from 28×25 mas pixel⁻¹ to 25×25 mas pixel⁻¹ (J. Krist, private communication). However, the photometric calibrations, both in the image headers and produced by SYNPHOT, assume that the final undistorted image is processed using DRIZZLE. The drizzled data product is similar to the manual calibration performed above and in K05, except that it does not include a uniform scaling of the image by a factor of 1.124. To correct the error, the disk brightness values reported in K05 should be increased by this factor. We adopted K05’s value of 8.63 ± 0.03 mag for the stel-

¹<http://www.stsci.edu/software/tinytim/>

lar brightness. Aperture size aside, our measurement methodology of the $F606W$ midplane surface brightness profile presented in §5.3.2 produces results consistent with K05 after scaling their surface brightness by a factor of 1.124. The stability of the HST/ACS PSF ensures that the flux calibration uncertainty, set by the 0.03 mag uncertainty in stellar brightness, is much lower than those of the near-IR bands. The stellar brightness in $F606W$ was measured in unocculted images at the same epoch, so our measurements are unaffected by the star’s variability.

5.3 Results

5.3.1 Disk Morphology

The PSF-subtracted images are shown in Figures 5.3 and 5.4. As observed by other authors, the disk has a near-edge-on morphology. The data in each band of Figs. 5.3 and 5.4 has been divided by the corresponding stellar brightness, such that the resulting colors trace the relative scattering efficiencies of the dust. We find the disk decreases in brightness relative to the star with increasing wavelength, up to K' -band, indicating an overall blue color. We do not detect the disk with strong confidence in L' .

The disk midplane shows vertical structure (Fig. 5.5). We fit a Gaussian function to the vertical profile of the disk as a function of projected distance. We subtract this profile from the image, scale the residuals by a smooth fit to the amplitudes of the Gaussians, and display the results in the left panels of the Figure. This procedure clearly reveals the location of a sharp midplane. Broader features also show variation — the width of the best-fit Gaussians is not constant with projected distance from the star. This effect has been noted and studied by other authors (K05; Graham et al. 2007). Capturing the vertical structure of the disk is important for detailed physical models of the system. However, here and in §5.4, we restrict ourselves to considering only the most basic disk properties and defer detailed two-dimensional modeling for future work. We will discuss the disk substructure (brightness enhancements and deficits) in §5.3.4.

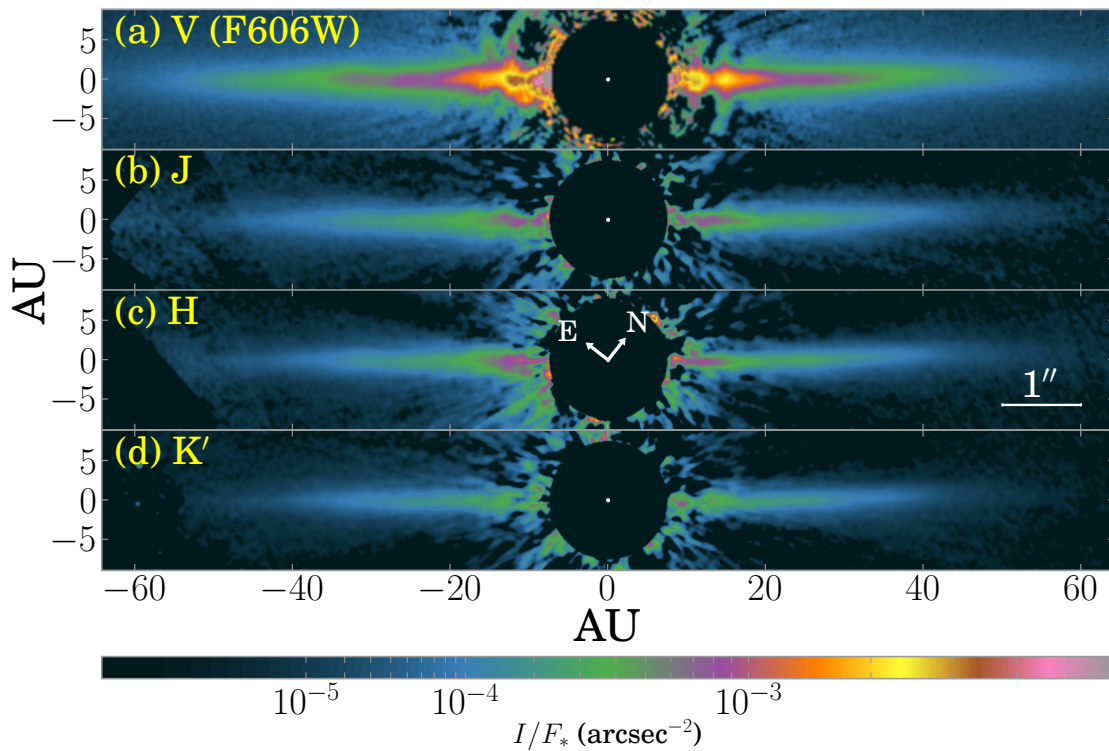


Figure 5.3 Images of the AU Mic debris disk with direct starlight removed via PSF roll subtraction (§5.2.2). Data are displayed on a square-root scale, and in each band the disk brightness I is divided by the stellar flux F_* , allowing for comparison of color differences intrinsic to the dust rather than the star. In each image, a circular software mask ($1''.5$ diameter) is applied to obscure subtraction residuals about the stellar location, marked by a small white circle. The near-IR images have been additionally smoothed by a Gaussian matched to the resolution of the PSF to eliminate small high-frequency errors introduced by the masking process (§5.2.2). The data in panel (a) were obtained with the ACS coronagraph aboard *HST*, while the data in (b)–(d) are newly acquired via Keck AO. The blue color of the dust is indicated by the trend of decreasing scattering efficiency toward longer wavelengths in panels (a)–(d).

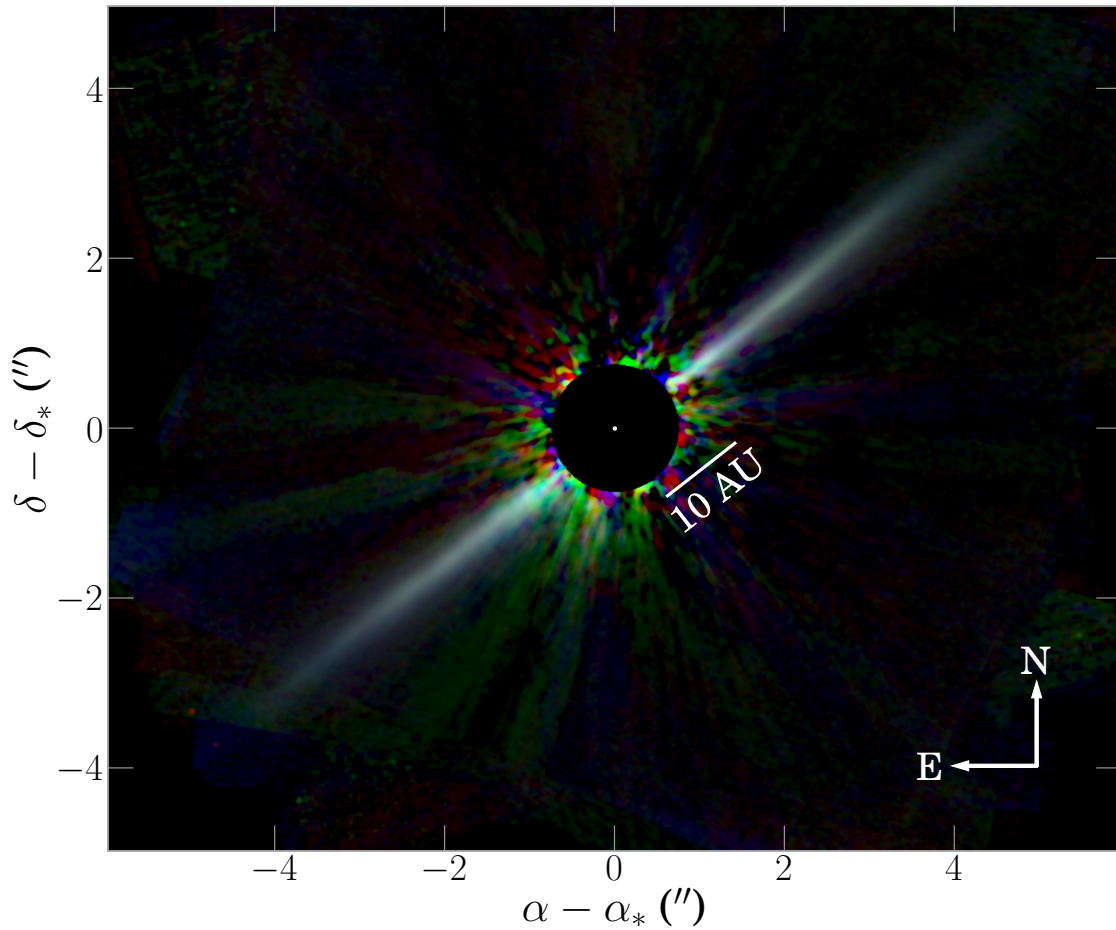


Figure 5.4 A JHK' composite image using the data in Figure 5.3. The data are displayed relative to the stellar brightness, highlighting the intrinsic color of the dust. The structures emanating from the mask outside of the disk are residuals from the stellar PSF subtraction. The blue color of the disk is visible, as is evidence for substructure.

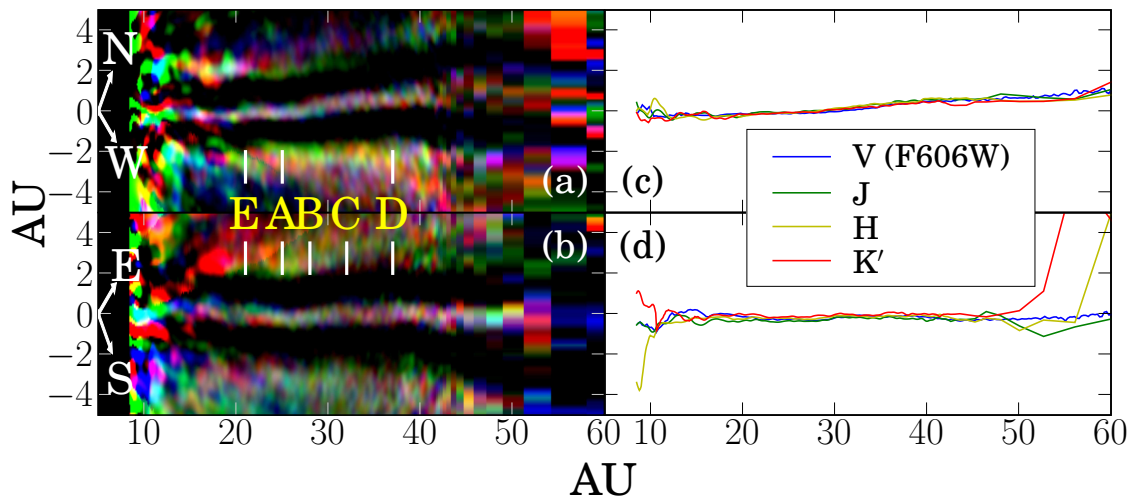


Figure 5.5 Vertical structure in the near-IR disk images. Panels (a) and (b) show a JHK' composite of disk images, whereby a Gaussian fit to the vertical structure of the disk has been subtracted. The residuals clearly show the location of the sharp midplane, and have been scaled by a smooth fit to the amplitudes of the Gaussian functions. The SE side is flipped about the star to allow for direct comparison to the NW. The locations of physical features are indicated (A–E; cf. Table 5.3). Panels (c) and (d) plot the variation of the vertical midplane position resulting from Gaussian fits to the vertical profile. No significant differences in midplane position with wavelength are seen.

5.3.2 Surface Brightness Profiles

Midplane surface brightness profiles are useful metrics of disk structure. These profiles average over the vertical extent of the observed scattered light image, which is naturally integrated along the line of sight. This facilitates comparison with scattered light models by reducing the brightness distribution to one dimension. We note that this convenient technique can fail to capture variation in the projected vertical extent of the disk, though we do follow the vertical centroid as a function of projected position. Prior to computing our profiles, we fit a spline to the vertical midplane position along each ansa. We used $0''.1 \times 0''.5$ photometric apertures centered on these positions in unsmoothed images to extract the photometry (Figure 5.6). The width of this aperture is chosen to provide sufficient spatial resolution along the disk midplane, while the height is sufficient to capture several vertical FWHM of the inner disk. As reported by Graham et al. (2007), the apparent *F606W* disk thickness increases outward, reaching the $0''.5$ aperture height at ~ 60 AU. Beyond this point, these photometric apertures do not perform a vertical average; rather, they sample the midplane brightness.

Our PSF-subtracted L' data exhibit very low S/N structures along the disk plane in L' at separations of $\sim 1''$ from the star, though these may result from PSF subtraction errors. In Figure 5.6, we show upper limits on the disk brightness in this band.

The uncertainties in Fig. 5.6 represent the random measurement errors. At each radius, the contribution from residual speckle and background noise sources was estimated from the standard deviation of photometry in apertures placed in an annulus, excluding the locations near the disk. The photon noise from disk photometry is also factored into the random errors. The inner and outer edges of the profiles are set by the requirement that $S/N \geq 1$. To estimate the contribution of PSF subtraction to the systematic errors, at each radius we compared the mean values of the off-disk apertures (placed in an annulus) to the random error estimated from their standard deviation. These are generally less than one, suggesting that any bias in the profiles is smaller than the estimated random errors. Another possible mechanism for systematic error arises in the near-IR data because the PSF estimates

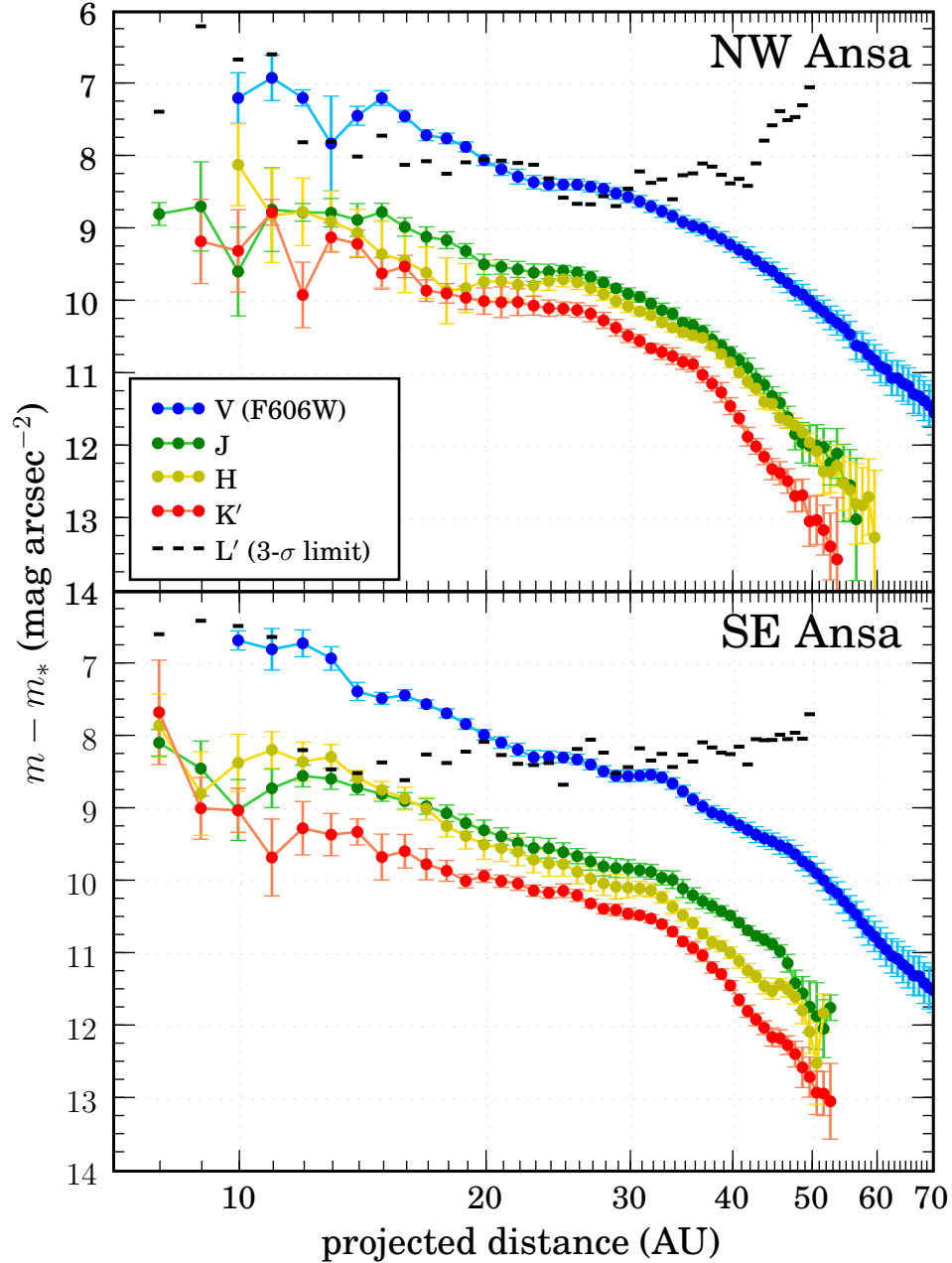


Figure 5.6 Midplane surface brightness profiles for the disk ansae. Flux was gathered in $0''.1 \times 0''.5$ apertures, which were placed according to the spline fit to the vertical disk midplane. The measurements are shown relative to the stellar brightness to highlight the intrinsic scattering properties of the dust in the J - to K' -bands. The uncertainties represent $1\text{-}\sigma$ random errors, and do not include systematic errors in calibration (§5.2.3). We also indicate $3\text{-}\sigma$ upper limits to the L' brightness.

are derived from the target exposures (§5.2.2 and §5.2.2). If there is insufficient field rotation in the images, light from the inner disk may be subsumed in the PSF estimate, resulting in a self-subtraction of the disk. Nearly all of our datasets have $\Delta\text{PA} > 30^\circ$ (Table 5.1), sufficient to exclude this as a source of significant error. However, the 2004 Aug 29 *J*-band data have $\Delta\text{PA} \simeq 17^\circ$, which corresponds to one disk midplane FWHM at ~ 8.5 AU. The 2004 Aug 30 data have much more field rotation, so the effect on the inner region of the composite *J*-band surface brightness profiles is likely to be small. Finally, the uncertainties in Fig. 5.6 do not include potential errors due to flux calibration, which may be as large as 0.2 mag for the *JHK'* bands (§5.2.3). We conclude that, relative to the random errors, the systematic errors are unlikely to affect the shape of the surface brightness profiles at separations greater than 8.5 AU.

By comparing our near-IR data to those of L04 and M05, we confirm a break in the overall midplane surface brightness profile around 30–35 AU. A break at ~ 15 AU in the *F606W* data was reported by K05, though the innermost points in our near-IR profiles are consistent with both a slight flattening and no break at all.

Broken power laws provide a compact description of the observed surface brightness profiles. Using flux-based units rather than magnitudes, we fit a function $f(b) \propto b^{-\alpha}$ to the midplane surface brightness profiles in Fig. 5.6, and report the resulting indices α in Table 5.2. We scale the formal $1\text{-}\sigma$ random errors by $\sqrt{\chi_\nu^2}$ when this quantity is > 1 to partially account for the ill-fittedness of a strict power-law to profiles which exhibit substructure. Errors in subtraction may be correlated because some PSF structures have significant radial extent. We ignore measurement covariance in the analysis, and thus potentially underestimate χ_ν^2 and the quoted errors. We chose to fit over two domains in projected separation: an inner region of 15.0–32 AU, and an outer region of 32–60.0 AU. The innermost boundary was chosen to mitigate possible biases from systematic errors. The outermost boundary is an upper limit, and is more precisely set by the availability of data in Fig. 5.6. The break between the two regions was chosen to correspond to the kink in the midplane surface brightness profile of the SE ansa, corresponding to feature C (§5.3.4). The power-law fits of our *H*-band data are somewhat consistent with those of L04, who

measures for the NW (SE) ansa $\alpha = 1.4 \pm 0.3$ (1.0 ± 0.3) over 20–35 AU and 4.4 ± 0.3 (4.4 ± 0.4) over 35–60 AU. Using the same method as used in Table 5.2 on these ranges (but different aperture sizes and positions), we obtain 1.6 ± 0.2 (1.5 ± 0.1) and 4.4 ± 0.2 (3.4 ± 0.2), respectively. The values we compute for the SE slopes are steeper in the inner region, but shallower outside. Our measurements are consistent with those of M05 over similar domains. Those authors measure $\alpha = 1.2 \pm 0.3$ over 17–33 AU and 4.0 ± 0.6 over 33–60 AU. Using these ranges and averaging over ansae (but different aperture parameters) we obtain 1.4 ± 0.2 and 3.8 ± 0.2 . We have significant differences in our *F606W* power-law indices relative to those of K05. The authors, using apertures that are $0''.25$ tall in the direction perpendicular to the mid-plane, calculate $\alpha = 1.8$ over the domain 15–43 AU, and 4.7 in the region beyond 43 AU, both of which are somewhat steeper than our findings of 1.6 ± 0.1 and 4.1 ± 0.2 (measuring from 15–43 AU and 43–70 AU with our apertures). However, measuring with $0''.1 \times 0''.25$ apertures over the region 43–60 AU and averaging the fit indices over both ansae, we find $\alpha = 4.7$ — consistent with K05. The differences in these comparisons serve to underscore the sensitivity of such power-law measurements to methodology. These differences may arise from PSF subtraction residuals, aperture sizes, aperture center locations, and the fit domain. Inferences between different datasets should be based on consistent power-law fits.

5.3.3 Disk Color Variation

The blue color, relative to the star, of the scattered light was first reported by K05. It becomes increasingly blue at larger radii ($F435W-F814W = 0.2-0.5$ mag from 30–60 AU). The disk also scatters blue when comparing visible data to the *H*-band measurements of L04 and M05. The blue color of the scattered light extends to our *JHK'* observations. Figure 5.7 shows the color as a function of projected radial position along the disk midplane. The stellar contribution to the apparent disk color has been removed in order to highlight intrinsic grain scattering processes. Systematic uncertainties in calibration are not included, though as discussed in §5.2.3–5.2.4, these are expected to be $\lesssim 0.3$ mag for *K'-H* and *J-H*, and $\lesssim 0.2$ mag for *F606W-H*. In the inner disk ($\lesssim 35$ AU), the observed color gradient is consistent with a flat

Table 5.2. Midplane Surface Brightness Power-Law Indices

band	ansa	fit domain	
		15–32 AU	32–60 [†] AU
<i>F606W</i>	NW	1.46 ± 0.09	3.00 ± 0.13
	SE	1.53 ± 0.08	2.97 ± 0.12
	avg.	1.49 ± 0.09	2.99 ± 0.12
<i>J</i>	NW	1.21 ± 0.10	3.95 ± 0.19
	SE	1.34 ± 0.12	3.27 ± 0.19
	avg.	1.27 ± 0.11	3.61 ± 0.19
<i>H</i>	NW	1.19 ± 0.19	3.84 ± 0.13
	SE	1.58 ± 0.15	3.47 ± 0.17
	avg.	1.39 ± 0.17	3.66 ± 0.15
<i>K'</i>	NW	1.24 ± 0.13	5.16 ± 0.23
	SE	1.09 ± 0.10	4.63 ± 0.16
	avg.	1.17 ± 0.12	4.90 ± 0.20

[†]Maximum projected distance used in fit; the domain may be further restricted by the availability of data in Fig. 5.6.

Note. — Power-law indices α , calculated by converting the the midplane surface brightness profiles (Fig. 5.6) to flux units and fitting $f(b) \propto b^{-\alpha}$. Formal 1- σ errors are scaled by $\sqrt{\chi^2_\nu}$ when this quantity is > 1 . These errors are lower limits, as both systematic errors and measurement covariance have been ignored. Entries marked “avg.” are computed by averaging α and its variance over both ansae

profile, while the outer disk is increasingly blue with stellocentric distance.

5.3.4 Disk Substructure

The AU Mic debris disk is known to exhibit non-uniformity in its midplane surface brightness distribution (L04; K05; M05). In order to remove global structure and highlight localized variations, we divided each brightness distribution by a smooth function in each band. We obtained weighted fits of spline functions to the NW and SE ansae’s midplane surface brightness profiles (§5.3.2) and averaged the results. The order and smoothness of the splines used to enhance the data have direct bearing on the spatial frequency content of the resulting map and may affect the observed positions and brightness of disk features. We used the `curfit` routine of FITPACK² to fit a cubic spline to the data in Fig. 5.6, with smoothness $s = m + \sqrt{2m}$, where m is the number of data points in the profile. Figure 5.8 shows an *F606W* image and a *JHK'* color composite that have been processed in this manner. The annotations give the locations of substructural features (A–E). To allow for more quantitative comparison of disk features, in Figure 5.9 we show surface brightness profiles processed in the same manner. In order to highlight the structure of midplane brightness, these profiles are computed with $0''.1 \times 0''.1$ apertures.

The imperfect removal of time-variable features in the PSF may introduce systematic errors which can masquerade as disk structures, underscoring the value of independent observations when identifying particular features. Liu (2004) identified several features of the disk substructure, which were also observed by K05 and M05. In independent observations such as these, any changes seen in the structures may be due to PSF-subtraction artifacts. However, given that AU Mic exhibits brightness variability due to starspots, it is also possible that these spots differentially illuminate the disk such that the spatial distribution of disk brightness is also time-variable. We also note that differences in feature position and brightness from different authors may arise via analysis methodology. As we have done in Figs. 5.8 & 5.9, it is desirable to highlight features by dividing the data by a function $f(b)$, where b is the projected stellar separation. For example, L04 used $f(b) = |b|^{-1}$ (see his Fig. 3)

²See <http://www.netlib.org/dierckx/>.

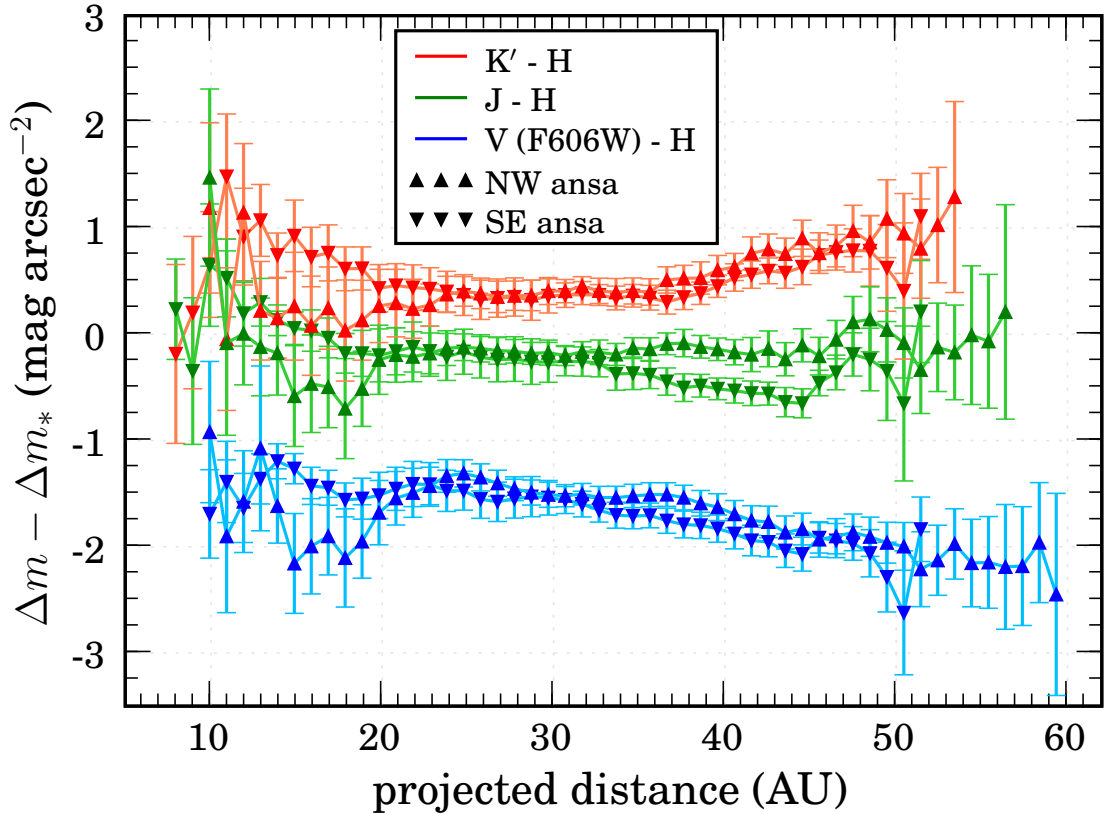


Figure 5.7 The disk color vs. the projected distance along the disk midplane. We compute disk colors relative to the H -band midplane surface brightness profile. The contribution of the intrinsic stellar color has been removed. The disk appears blue between the visible and near-IR and between H and K' . Note that $K'-H$ colors are shown, which accounts for the reversed gradient from $F606W-H$. Systematic uncertainties in calibration are not included, though these are expected to be $\lesssim 0.3$ mag for $K'-H$ and $J-H$, and $\lesssim 0.2$ mag for $F606W-H$ (§5.2.3–5.2.4). In the inner disk ($\lesssim 35$ AU), the colors are consistent with a flat profile. The outward branching of these curves in the outer disk indicates blue color gradients (most clearly indicated by the $F606W-K'$ color). These gradients may indicate differences in grain sizes or compositions.

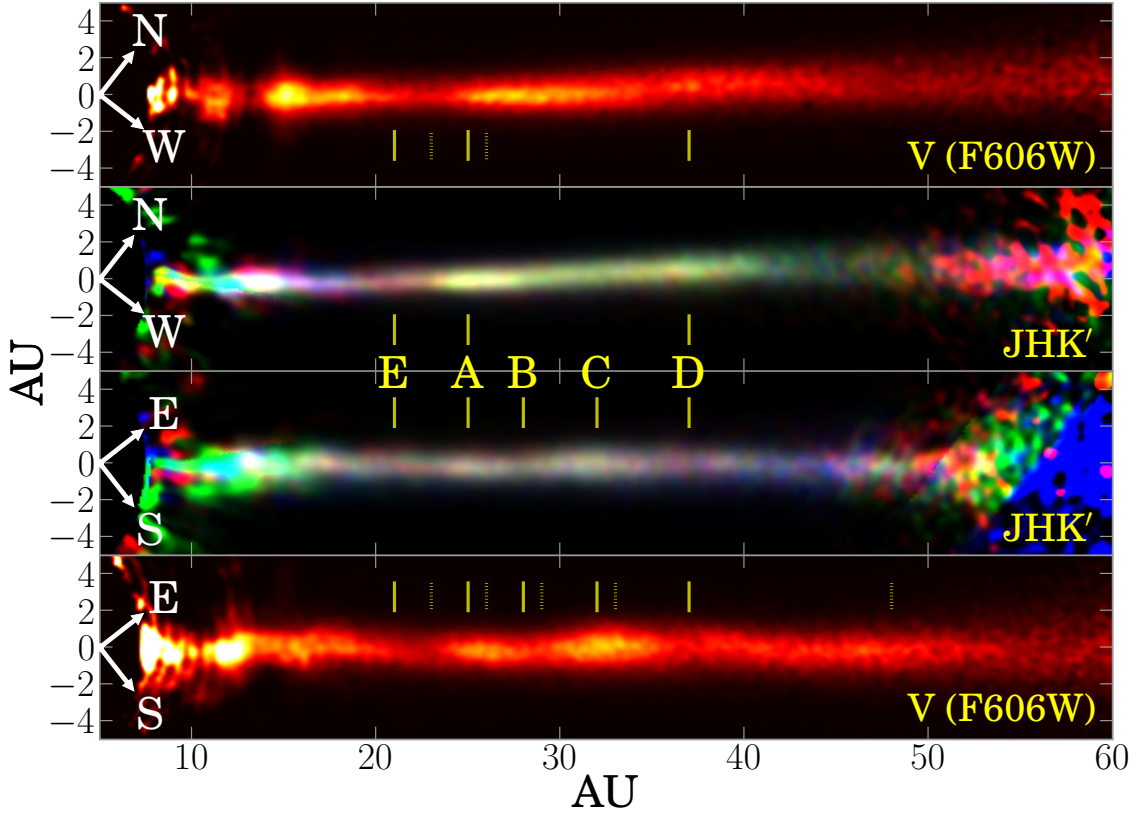


Figure 5.8 Substructure in the disk images. The upper and lower panels are $F606W$ data, while the middle panels are JHK' composites. The image in each band is scaled by a spline fit to an average of its NW and SE midplane surface brightness profiles (§5.3.2). The SE side is flipped about the star to allow for direct comparison to the NW. Feature locations in the near-IR are indicated by solid lines (A–E), while the original identification of feature locations in $F606W$ data by K05 are shown as dotted lines (cf. Table 5.3). A broad clump in the SE ansa at 48 AU was also identified by K05. We confirm the presence of a brightness deficit at location E. In our favored models (§5.4), the bulk of the scattered light comes from small grains outside of 40 AU. Therefore, the features at projected distances inward of 40 AU (A–E) must arise from azimuthal perturbations in the dust distribution outside this radius. The origin of the substructures is unknown; they may result from the gravitational influence of unseen planets.

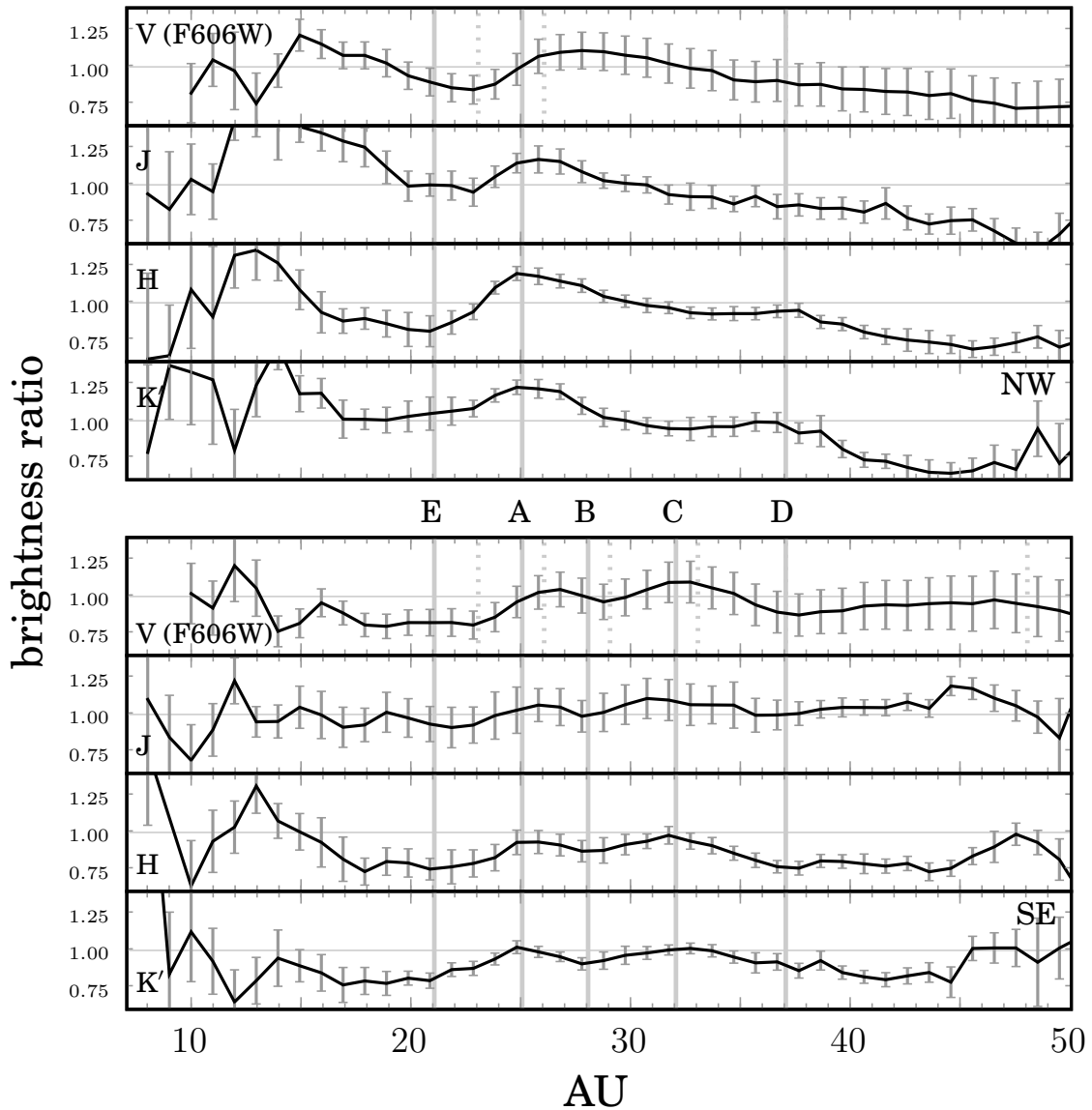


Figure 5.9 Substructure in disk profiles. Surface brightness profiles computed with $0''.1 \times 0''.1$ apertures have been processed in the same manner as Fig. 5.8, by dividing each wavelength's profile by a smooth spline function derived from an average of the NW and SE profiles from Fig. 5.6. Feature locations derived for the near-IR data are indicated by solid vertical lines (A–E), while dotted lines indicate the feature locations in *F606W* data by K05.

and M05 used $f(b) = b^{-2}$ (their Fig. 3b). In contrast, K05 use a fourth-order polynomial fit to the surface brightness profile for $f(b)$, while we use a spline fit (detailed above). These more complicated functions can better capture the overall brightness profile of the disk, which does not follow a single power law. On the other hand, they can suppress the appearance of the broadest features (e.g. feature D in the NW ansa).

The application of the spline fit to the $F606W$ - and JHK' -band data allows us to eliminate analysis methodology as a potential source of variation in feature brightness and position. While there are minor differences in the apparent characteristics of features between the near-IR bands, distinct differences in feature location arise when comparing those seen in visible to the near-IR.

Feature A, which is a brightness enhancement seen in both ansae, is ~ 1 AU further from the star in the visible (26 AU) compared to the near-IR (25 AU). There is also evidence for a change in the position of this feature in the near-IR; in particular, the J -band centroid is further out than in H or K' (cf. Fig. 5.9). Feature B is a brightness deficit in the SE ansa that also exhibits a similar inward-moving centroid with increasing wavelength. Feature C is a SE brightness enhancement, broader than A, that shows a different position depending on the waveband. In J and H , the feature centroid is at ~ 32 AU, while it peaks closer to 33 AU in $F606W$ and K' . Feature D (37 AU) corresponds to a broad enhancement on the NW ansa, a narrower dip in the SE ansa brightness, and the location of the vertical displacement of the NW midplane. The position of this feature is not significantly wavelength-dependent in these data. We confirm K05's identification of a dip in midplane brightness inward of feature A, which we denote 'E.' The locations of the other features seen in $F606W$ agree with the positions given by K05. The H -band positions and characteristics of features A–D compare favorably to the results of L04. Together these strengthen the evidence for ~ 1 AU differences in the positions of features A–C. In contrast, M05 measures positions for A and B slightly closer to the star (by 2–3 AU); however those data are of lower S/N and the differences may not be significant. A summary of these results is given in Table 5.3.

There are additional deviations in brightness that are detected in multiple

Table 5.3. Comparison of Disk Features

Label	NW	SE	Location (AU)			
			L04	K05	M05	this work
A	↑	↑	25	26	22	25
B	...	↓	28.5	29	26	28
C	...	↑	31	33	32	32
D	↑	↓	37	37	38	37
E	↓	↓	...	23	...	21

Note. — Features are marked in Figure 5.8. Arrows denote localized enhancements (↑) and deficits (↓) of disk brightness. Feature locations in K05 are seen in *F606W*, while L04 and M05 are *H*-band. Average feature locations in the near-IR data from this chapter are in the final column, based on visual positions in Fig. 5.8 with uncertainties of approximately ± 0.5 AU. We newly designate the close-in feature E here.

bands. The broad enhancement at ~ 46 AU in the SE noted by K05 is also detected in all the bands we consider. The feature seen in the *F606W* data, characterized by a peak enhancement at 15 AU and sharper drop at 12 AU, has corresponding characteristics in the near-IR bands. In *JHK'*, the peak is seen at 12–13 AU and the inner cutoff at 11–12 AU. The outer extent of this feature decreases gradually from ~ 20 AU in *F606W* to 17 AU in *K'*. The peak enhancement in the SE at ~ 12 AU in *F606W* also has corresponding enhancements at 12–13 AU in *J* and *H*; an examination of the *K'*-band surface brightness profile (Fig. 5.6) suggests the enhancement may also be present at ~ 13 AU in this band, but is not visible in Figs. 5.8 & 5.9 due to the spline fitting process.

5.3.5 Point Source Detection Sensitivity

We do not detect any point-like sources in the disk midplane. We have developed a methodology for utilizing the artificial insertion of point sources into an image to measure the detection sensitivities in both the background and the disk midplane. We detail our technique here.

When quoting sensitivity limits for the detection of point sources around a star, it is common practice to measure the standard deviation of pixel values in concentric annuli, $\hat{\sigma}(r)$, and to set a scale to this curve with artificially inserted sources. In this case, σ represents a by-eye threshold. Here we wish to extend this methodology for the case of sources within the disk. To this end, we adopt a model for the sensitivity and solve for this model's parameters through visual detection of randomly inserted sources (both inside and outside of the disk) and maximum likelihood techniques.

We assume that the process of detecting a source can be characterized by zero-mean, normally distributed background noise fluctuations. In this case, the background can be characterized by σ , and the probability of detecting a source (denoting $D = 1$ for detection) of flux f is given by

$$P(D = 1|f, \sigma) = \frac{1}{2} \left[1 + \operatorname{erf} \left(\frac{f}{2\sigma} \right) \right], \quad (5.5)$$

which is the cumulative normal distribution function. Our task is to determine σ , which we can assume is proportional to $\hat{\sigma}(r)$ in regions devoid of disk light. Similarly,

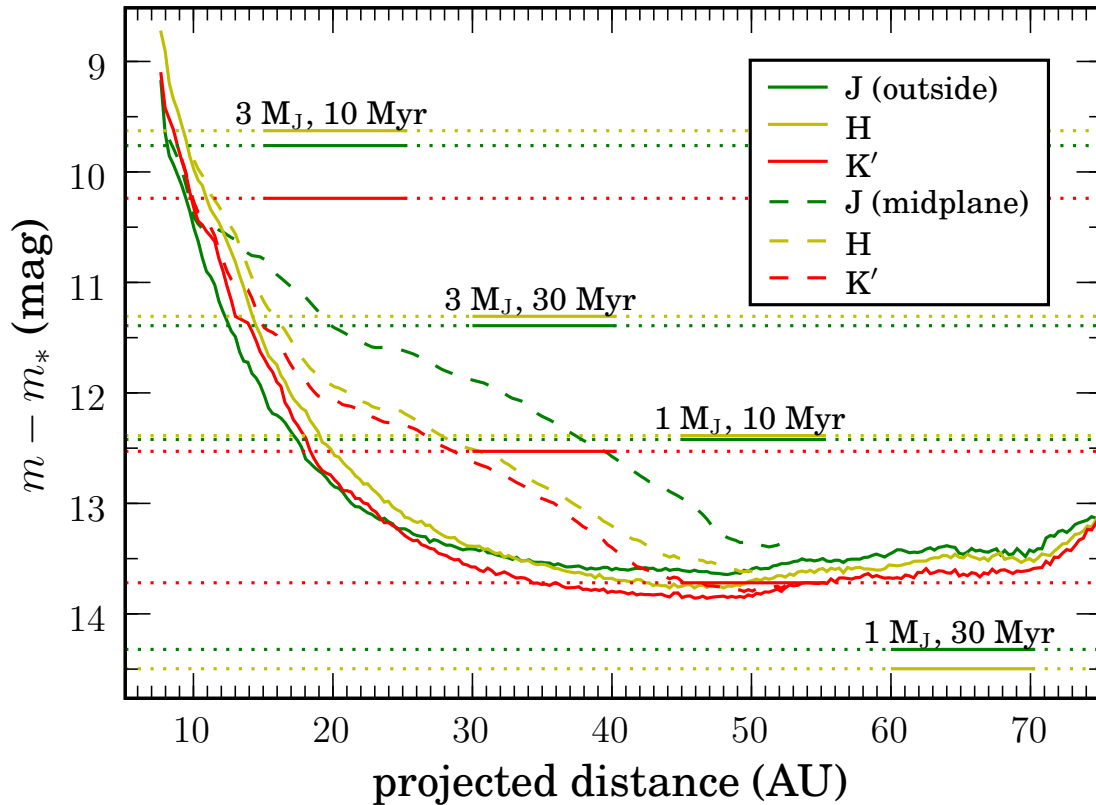


Figure 5.10 Point source detection limits ($5\text{-}\sigma$). The solid curves are for sources outside of the disk, while the dashed curves give limits for sources residing in the disk midplane. In some places the midplane is more than a magnitude less sensitive. No point sources were detected along the disk. Horizontal lines indicate the predicted brightnesses for the model giant planets of Burrows et al. (1997), at ages of 10 and 30 Myr (AU Mic is 12^{+8}_{-4} Myr; Barrado y Navascués et al. 1999). Initial conditions play a large role in the luminosity evolution of young $\sim 1 M_J$ planets, and these “hot start” models represent brightness upper limits (e.g. Fortney et al. 2005; Marley et al. 2007).

in the disk midplane, we expect an additional contribution to the background fluctuations from the disk light. For our ground-based observations, these fluctuations are dominated by speckle noise (including Strehl fluctuations) rather than photon statistics, and therefore the variance of this contribution is proportional to the square of the disk brightness, I^2 (e.g. Aime & Soummer 2004; Fitzgerald & Graham 2006). We model the sensitivity in the midplane by

$$\sigma^2(\mathbf{x}, \mu, \xi) = \mu^2 \hat{\sigma}^2(\mathbf{x}) + \xi^2 I^2(\mathbf{x}). \quad (5.6)$$

We fix $\xi = 0$ to model the sensitivity in regions devoid of disk light. We measure $\hat{\sigma}(r)$ with a sigma-clipped sample standard deviation of pixels in concentric annuli, excluding regions of disk emission.

We randomly generated positions and fluxes for artificial sources to be inserted in each of our ground-based images. Two populations of sources were generated — one set randomly distributed along the disk midplane, and another in the off-disk region. The number of sources in each population was drawn from a Poisson distribution, and no blending of sources was allowed. Fluxes were drawn from a log-uniform distribution about $\sigma(\mathbf{x}, \mu = 1, \xi = 1)$ in the midplane and $\sigma(\mathbf{x}, \mu = 1, \xi = 0)$ elsewhere. After the computer inserted the randomly generated sources, the images were inspected and detections recorded. False detections were ignored in our analysis.

With these data in hand, the problem reduces to finding the most likely model parameters (μ, ξ) given the set of artificial source positions, fluxes, and detections $\{\mathbf{x}_i, f_i, D_i\}$. Our sensitivity curves will use the model parameters which maximize the probability density $p(\mu, \xi | \{\mathbf{x}_i, f_i, D_i\})$. This quantity can be re-written with Bayes' Theorem,

$$p(\mu, \xi | \{\mathbf{x}_i, f_i, D_i\}) \propto p(\mu, \xi) p(\{\mathbf{x}_i, f_i, D_i\} | \mu, \xi), \quad (5.7)$$

$$= p(\mu, \xi) \prod_i P(D_i | \mathbf{x}_i, f_i, \mu, \xi) p(\mathbf{x}_i, f_i), \quad (5.8)$$

$$\propto p(\mu, \xi) \prod_i P(D_i | \mathbf{x}_i, f_i, \mu, \xi). \quad (5.9)$$

The final step is valid since we are free to choose the position and flux distribution of independent artificial sources without regard to the model parameters. Our prior information on the model parameters is represented by $p(\mu, \xi)$, and we assume uniform

distributions which are also independent of μ, ξ . We maximized the logarithm of this function with respect to μ and ξ for each of our JHK' images, to obtain best-fit 1- σ sensitivities, and we show our 5- σ point source detection sensitivity as a function of separation from the star in Figure 5.10. Midplane sensitivities are averaged over both ansae. We show predicted planet brightnesses using models of Burrows et al. (1997) at different ages, allowing inference of detection limits for planet mass. We note the caveat that at young ages, the emission from Jupiter-mass planets may be sensitive to initial conditions (e.g. Fortney et al. 2005; Marley et al. 2007).

5.4 Analysis

Models of the grain size and space distributions that reproduce the scattered light and thermal emission probe the dynamical processes affecting the dust distribution. Previous models of the AU Mic disk have attempted to model the SED (Chen et al. 2005) and the scattered light profiles (e.g. K05). Metchev et al. (2005), Augereau & Beust (2006), and SC06 tackled the task of simultaneously fitting both. Using continuous power-law descriptions for the grains' space and size distributions (sub- μm to mm sizes), M05 find they cannot simultaneously account for the scattered-light color, the SED, and the break in the surface brightness profiles at ~ 35 AU. As an alternative to power-law density distributions, Augereau & Beust (2006) obtained surface density models via scattered-light profile inversion. They tuned the size distribution to simultaneously fit the scattered light and SED. A distribution of silicate grains successfully matched the $F606W$ -band profiles and SED, and in a separate fit, the H -band profiles and SED could be matched using a minimum grain size that is 10 times larger than the visible case. This discrepancy implies that size distributions which match the scattered light colors underestimate the amount of large grains responsible for the sub-mm emission. A different approach was taken by SC06, who modeled the dynamical structure of the debris disk to match the $F606W$ scattered light and SED. For sufficiently large values of the stellar mass loss rate \dot{M} , this model produces a blue color, with an outward blue gradient.

These previous efforts highlight two essential results. First, the blue color of

the scattered light suggests small dust grains scattering in the Rayleigh regime, i.e., submicron particles. Second, the shallow slope of the long-wavelength SED is best fit with large grains of up to mm size (grains larger than this are weakly constrained). More recently, Graham et al. (2007) demonstrated that the linear polarization of the *F606W* scattered light requires porous grains. These data are important because the degeneracy between scattering asymmetry and spatial distribution can weaken inferences of debris disk structure based solely on measurements of total intensity. As the structure, size, and compositions of the grains determine the scattering properties, the assumption of compact grain types in previous work warrants reexamination.

Our goal is to find the simplest description of the grains and their distributions that is compatible with the variety of available observational data. In §5.4.1 we describe the methods and structure of our models, the process used to fit the models to the observed scattered light and SED, and the properties of the resulting best-fit models. We then examine these results in the context of the dynamical model of SC06 for a steady-state grain distribution produced by a ring of parent bodies (§5.4.2).

5.4.1 Dust Modeling

Monte Carlo Radiative Transfer

We model the debris disk around AU Mic using MCFOST, a Monte Carlo radiative transfer code that uses the Stokes formalism to treat the interaction between dust grains and photons to produce SEDs, scattered light images, and polarization maps. MCFOST is fully described in Pinte et al. (2006), and we summarize its main features here. Monochromatic photon packets are emitted by the star and propagated through the disk. The optical depth through which the photon travels before it interacts with a dust grain is randomly chosen from an $e^{-\tau}$ probability distribution. Scattered light and the thermal SED are computed separately. When monochromatic scattered light images and polarization maps are produced, photons are only allowed to scatter off dust grains, with a loss of intensity corresponding to the absorption cross-section of the grain. When the SED is computed, photons

are either scattered or absorbed, depending on the local albedo; in the latter case, they are immediately re-emitted at a longer wavelength selected on the basis of the local dust temperature. Once photons exit the computing volume, they are stored in “reception captors,” corresponding to specific inclinations. Maps at all inclinations are simultaneously created, but in this study we focused on the most edge-on captor, which includes inclinations ranging from 88.9° to 90° , believed to be appropriate for the inner disk of AU Mic.

To calculate the thermal equilibrium of dust grains, and therefore SEDs, the dust properties must be known throughout the electromagnetic spectrum, from the ultraviolet to the millimeter regime. It is not possible to describe the dust grains with a simple parametrization based on the albedo and the phase function asymmetry factor, for instance, unless these are known at all wavelengths. Rather, MCFOST relies on Mie theory (i.e., the grains are assumed to be spherical or essentially randomly oriented), so the knowledge of the dust optical indices (the complex index of refraction) at all wavelengths is sufficient. Grains with complicated structure, such as porous aggregates, are approximated by spheres with an effective optical index at each wavelength. Mie theory is used to calculate the scattering and absorption properties for these effective-medium spheres. In the case of AU Mic, small Rayleigh-scattering grains are indicated by the blue color and high polarization fraction (Graham et al. 2007). For composite grains, an effective medium approximation (depending on the constituent materials and method for computing the effective indices) can be reasonably accurate in the Rayleigh limit (Voshchinnikov & Mathis 1999).

MCFOST was first developed to model gas-rich, optically thick disks surrounding T Tauri stars. Several features have been added to efficiently and correctly treat the case of optically thin debris disks like AU Mic. The first modification was to increase the computational efficiency of treating optically thin material. Rather than expend effort computing the fates of all random photons, the majority of which will not scatter off grains in the optically thin disk, we enforce the first scattering of each photon packet to occur within the disk. The expected non-interacting photons are not randomly generated; instead we analytically account for the correspond-

ing transmitted starlight. This ensures that all randomly generated stellar photons scatter at least once in the disk without energy loss. Second, in the absence of gas and given the low density of dust particles, the dust grains cannot be considered to be thermally equilibrated with one another. Rather, we compute a size-dependent temperature for the grains, each being in equilibrium with the surrounding radiation field. In the case of the AU Mic disk, this results in a significantly different shape of the SED in the mid-infrared due to large difference in temperature between grains of different size. Future high-resolution spectra in the $10\ \mu\text{m}$ region may measure features which can constrain the composition and size distribution of grains (e.g. Li & Greenberg 1998; Chen et al. 2006).

Model Construction

Disk models frequently assume power-law descriptions for both the geometry of the disk and the grain size distribution. This is unlikely to reproduce all observed aspects of the disk, such as the complex small-scale structure seen in the scattered light (§5.3.1). It is nonetheless a valuable approach for constraining some of the main system parameters and testing simple hypotheses. Here, we attempt to reproduce the observations of the disk (SED and scattered light profiles) with a two-zone disk description. In a narrow inner zone, large grains would be present and account for most of the long wavelength thermal emission, whereas a much more extended outer region would contain small grains and be responsible for the scattered light. This is a model that qualitatively matches models proposed by SC06 and Augereau & Beust (2006), where our inner annulus would represent the observable population of parent bodies and the outer zone the populations of small grains created by collisions of large bodies and swept out by pressure forces.

In both regions, we assume that the surface density and the grain size distributions follow $\Sigma(r) \propto r^p$ and $dN(a) \propto a^\gamma da$. The outer radius is fixed at 300 AU, as scattered light has been detected out to a sensitivity limit of 210 AU (Kalas et al. 2004). The inner radius and transition radius between the inner and outer regions are free parameters. In addition, the surface density index, minimum and maximum grain size and distribution index, and the total dust mass in each of the two

zones are free. We initially use a $\gamma = -7/2$ index for the size distribution, which is commonly assumed for debris systems and is suitable for a steady-state collisional cascade (Dohnanyi 1969). While both theory and observations may suggest specific functional forms for the vertical density profile of the disk, we cede to our preference for simplicity and assume that the vertical density distribution follows a Gaussian with a fixed width of $\sigma = 0.8$ AU and a flat radial dependence. In this case, the photometric apertures capture the majority of the scattered light flux during brightness profile calculation. The particular choice of vertical density function is unimportant as long as the scale is much less than the photometric aperture height (§5.3.2). We defer for future modeling the exploration of relationships between the form of the vertical density profile, the dependence of scale height with radius, grain scattering phase functions, and the geometry of the disk.

The data for the SED were first compiled by M05 and supplemented with new *Spitzer* measurements by Chen et al. (2005). We use a $T_{\text{eff}} = 3600$ K, $\log g = 4.5$ NEXTGEN model for the stellar photosphere (Hauschildt et al. 1999), using radius $R = 0.88 R_{\odot}$ to match the observed stellar flux. For scattered light, we use the J -, H -, and K' -band profiles from data presented here, as well as the $F606W$ -band profiles from data initially presented by K05 and re-analyzed for this work in §5.3.2.

Fitting Procedure

Thorough exploration of the available parameter space is a time-consuming task when producing a SED and multiple scattered light images. We therefore explored it by hand, iteratively narrowing down the possible values for each parameter. Our objective is not to find the best possible model, but to determine if there is at least one solution based on this simple two-zone model that can match the data relatively well, which would in turn provide support to theoretical birth ring models (SC06; Augereau & Beust 2006). We compare our results to these models in §5.4.2. To further reduce computation, we have elected to fit the $F606W$ - and H -band profiles and the SED, and to later check for consistency with J - and K' -band profiles and $F606W$ fractional polarization curves of Graham et al. (2007). We calculate the model profiles with the same rectangular aperture sizes as the observed

profiles in §5.3.2 ($0''.1 \times 0''.5$).

We used a grain model that intrinsically includes a high porosity, a characteristic that provides both strong forward scattering and polarization — necessary features as demonstrated by Graham et al. (2007). The dust model developed by Mathis & Whiffen (1989) consists of a mixture of silicate, carbonaceous, and icy small elements combined into porous aggregates. With $a_{\min} = 5 \text{ nm}$, $a_{\max} = 0.9 \mu\text{m}$, a size distribution index of $\gamma = -3.9$, and a vacuum fraction of 80%, this model reproduces the interstellar extinction law from the ultraviolet to the near-infrared. We use the same optical constants but allow the size distribution to vary. We fixed the inner zone’s size-distribution index to $\gamma = -3.5$. We searched for the power law distributions that would adequately produce the blue color (in terms of albedo \times opacity) and roughly wavelength-independent phase function, so as to maintain roughly parallel surface brightness profiles from *F606W* to *H*. It was then possible to adjust the model parameters until a match to the SED and the scattered light profiles was obtained. We tuned the boundaries, grain size distributions, surface density indices, and total mass of each zone. For comparison, we also fit a model using the optical properties of compact silicate grains (from Draine & Li 2001) using the same procedure.

Fit Results

The parameters of our best-fit models are listed in Tables 5.4 and 5.5, and the results are shown in Figures 5.11 and 5.12. Considering the *F606W*- and *H*-band profiles and the SED, we obtain reasonable agreement with the predictions our two-zone model using porous grains: a region of large grains between 35–40 AU, and a region of smaller grains outward of 40 AU. These are slightly further out than the best-fit regions using compact grains, which are more isotropically scattering. We find that, if the particles in the inner region are porous, they must be in the mm-regime (sizes of 3–6 mm). Allowing the size distribution to encompass smaller grains results in an overly steep long-wavelength SED as well as a flux deficiency in the outer small grain region. Much larger bodies could be present yet undetectable; they would emit very little, even at mm wavelengths. For porous dust in the outer region, we

Table 5.4. Best-Fit Model Parameters

region	range (AU)	dust mass (M_{\oplus})	a	γ	p
porous (Mathis & Whiffen 1989)					
inner	35–40	1.0×10^{-2}	3–6 mm	-3.5^{\ddagger}	+1.5
outer	40–300	2.3×10^{-4}	0.05–3.0 μm	-4.1	-2.5
compact (Draine & Li 2001)					
inner	28–32	2.7×10^{-2}	1–2 mm	-3.5^{\ddagger}	+1.5
outer	32–300	2.7×10^{-4}	0.15–50.0 μm	-4.1	-2.5

‡ Fixed.

Note. — Parameters for our models which produce the best fit to the *F606W*- and *H*-band profiles and SED, for both porous and compact grains. The grain size distribution is $dN(a) \propto a^{\gamma} da$, while the surface density is described by $\Sigma(r) \propto r^p$. Illuminating star: $T_{\text{eff}} = 3600$ K, $\log g = 4.5$ NEXTGEN model, stellar radius $0.88 R_{\odot}$. Both models give comparable fits to the scattered light and SED, but the measured polarization rules out compact μm -sized grains (Figs. 5.11 & 5.12).

require a distribution encompassing small grains (0.05–3.0 μm , $dn \propto a^{-4.1} da$), with a power-law index that is steeper than the collisional steady-state value of -3.5.

The masses in the inner and outer regions of the porous grain model are around $1.0 \times 10^{-2} M_{\oplus}$ and $2.3 \times 10^{-4} M_{\oplus}$, respectively. The surface density profile falls rapidly outside of the transition radius (index -2.5 to -3.0), as expected from swept up material; shallower indices yield an improved SED but insufficient scattered flux inside 40 AU and too-shallow profiles overall. Steeper indices yield an excessively precipitous *F606W*-band brightness profile and excess flux around 50–100 μm . In the inner region, the surface density can be flat or increase with radius, peaking at the transition radius. This is only loosely constrained: the big grains never get very

Table 5.5. Best-Fit Model Avg. Scattering Parameters

λ	g	A
porous		
606 nm	0.83	0.52
1.6 μm	0.81	0.54
compact		
606 nm	0.66	0.83
1.6 μm	0.60	0.81

Note. — Scattering parameters for the outer regions of our best-fit models (Table 5.4), averaged over the grain size distribution. The scattering asymmetry factor g and albedo A are given.

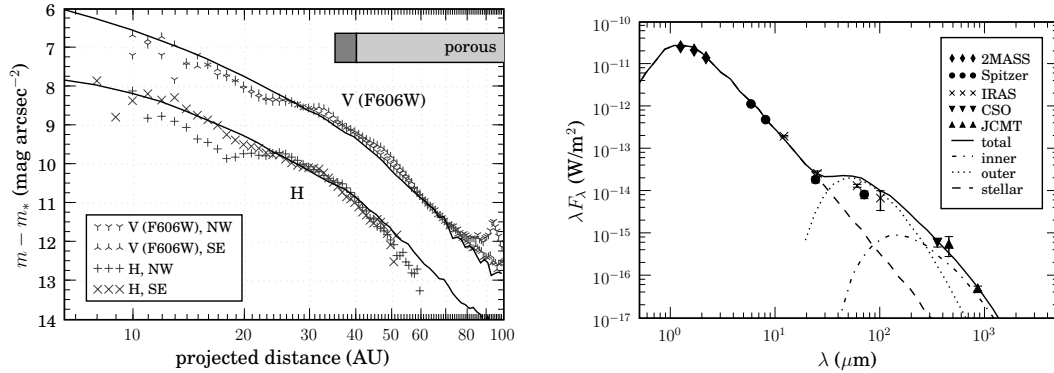


Figure 5.11 A model fit to the scattered light and SED of the system. (*left*) The surface brightness profiles from Fig. 5.6 along with surface brightness profiles from the best-fit model. The gray boxes above the profiles represent the grain locations in our model (cf. Table 5.4); the dark region indicates the inner region of larger grains, while the smaller scatterers are in the lighter zone outside. (*right*) The model SED along with measured photometry of AU Mic. In this model, the smaller grains are responsible for the bulk of the scattered light and the mid-IR emission, while the larger grains reproduce the long-wavelength end of the SED.

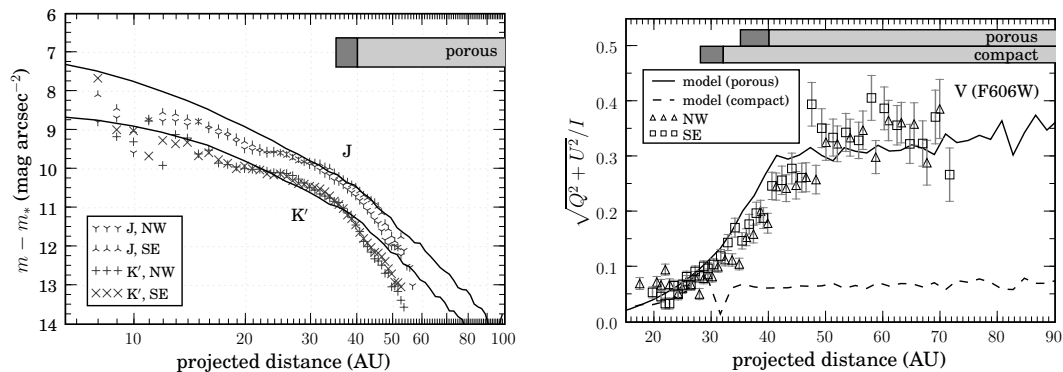


Figure 5.12 (*left*) A comparison of the surface brightness profiles from Fig. 5.6 to surface brightness profiles from the best-fit model in J and K' bands. These data were not used in the fitting process. The differences in overall flux may be due to photometric calibration uncertainties (§5.2.3), though the model clearly overestimates the emission in the outer zone in these bands. More complicated models may resolve these discrepancies; a changing minimum grain size with radius can produce a color gradient. (*right*) The fraction of linear $F606W$ polarization produced by our model compared to measurements of Graham et al. (2007), which include both systematic and random errors. Compact, μm -sized grains are ruled out by these data.

hot in this narrow annulus and there is little effect on the SED.

We performed some exploration of the parameters to estimate uncertainties. The masses are relatively well constrained, to 50% or so, depending on the grain size distribution parameters. Again, more mass could be hidden in the form of very large bodies in the inner region; the mass derived here is just what is needed to reproduce the long wavelength end of the SED. In computing the total intensity of scattered light, there is an anticorrelation between a_{\min} and the region boundary at ~ 40 AU. We can adjust the minimum grain size by a factor of 2, and the ring radius by ± 5 AU and still achieve satisfactory *F606W*- and *H*-band profiles and SED.

As demonstrated by Graham et al. (2007), the fractional linear polarization profiles provide a complementary constraint on the optical properties of the small grains. The measured fractional polarization gradually rises to a plateau of $\sim 35\%$ at around 50 AU. Our best-fit models using compact and porous grains are comparable in fit quality for the total scattered light intensity profiles and the SED; however the polarization curves in Fig. 5.12 clearly rule out compact grains, which reach maximum fractional polarizations $< 10\%$. The porous grains generally follow the measured trend, and reach a plateau of 30–35% by 40 AU, the starting location of the small outer grain region.

This model has some shortcomings, in that it predicts excess flux around 60–70 μm and a slightly too-shallow scattered-light profile in the *H* band outside of the transition radius. This latter point results in a predicted disk color that does not change outside of $1''$, as opposed to the observations. We also note that the model profiles show less agreement with the *J*- and *K'*-band profiles (Fig. 5.12). The overall flux levels differ (though this may coincide with photometric calibration uncertainty; cf. §5.2.3), and we overpredict the midplane surface brightness in the outer regions. For this analysis, we have avoided goodness-of-fit metrics like χ^2_ν because our model, by design, will fail to reproduce substructure in the scattered-light profiles. Further, PSF subtraction residuals introduce correlations between errors in the measured profiles, which we ignore (§5.3.2). Nevertheless, we can get a sense of model fidelity by considering the long wavelength end of the SED (where the dust contributes). For the nine SED points in Fig. 5.11 at $\lambda > 10 \mu\text{m}$, the best-fit compact grain model

gives $\chi = 8.6$ and the porous model gives $\chi = 10.9$. The bulk of the deviation arises from the 60–70 μm region. A formal χ^2_ν analysis is not applicable, as we have also tuned our parameters to match the scattered light. In contrast to the porous grain model, the compact grain model underpredicts the 60–70 μm flux. With their higher average albedo, the compact grains absorb less energy than the porous ones (Table 5.5), suggesting a better fit may be obtained with grain albedos in the 0.6–0.7 range. Still, the fit is satisfying, considering the simplicity of the model (§5.4.1). Presumably, considering non-power law prescriptions, other dust composition, non-spherical grains, and/or overlap between small and large grains would result in a better fit. One attractive possibility, that we do not explore here, is that ever-smaller grains are present as we move outside of the belt of parent bodies (§5.4.2). This could account for the increasingly blue color in the outer region as well as for the seemingly different transition radii obtained from the *F606W*- and *H*-band profiles (~ 40 AU vs. ~ 30 AU).

5.4.2 Birth Ring Examination

In the Solar System, the Asteroid Belt and Classical Kuiper Belt constitute rings of solid bodies that, through mutual collisions, act as sites of continual dust production. Several forces act on the newly liberated grains, and the resulting trajectories shape the overall structure of the Sun’s debris disk. A similar belt of parent bodies has been invoked to explain the break in the surface brightness profile of the β Pic debris disk (Lecavelier Des Etangs et al. 1996; Augereau et al. 2001). Additional rings have been proposed to explain features seen in recent imaging (e.g. Wahhaj et al. 2003; Telesco et al. 2005) and spatially resolved spectroscopy (Weinberger et al. 2003; Okamoto et al. 2004) of this system. An attractive feature of such models is that their dust distributions are in steady-state — we need not appeal to a rare (but recent) catastrophic collision between large (e.g. km-sized) bodies, such that fresh grains have had insufficient time to completely diffuse through the system.

The breaks in the slopes of AU Mic’s surface brightness profiles naturally raise the prospect of a ring of parent bodies analogous to the Classical Kuiper Belt. The existence of such a belt was proposed by M05, SC06, and Augereau & Beust

(2006). Here, we focus our attention on a detailed theoretical model, developed by SC06, which yields the steady-state spatial and size distributions of dust grains in the disk. A critical parameter is the stellar mass-loss rate, \dot{M}_* , which governs the corpuscular forces on the grains. In addition to modifying the disk structure, the stellar wind is crucial in determining the lifetimes of debris disks around late-type stars (Plavchan et al. 2005). Assuming the scenario of steady-state dust production by a ring of parent bodies is applicable, one may use a dynamical model to infer \dot{M}_* from observations. We note that the theory was applied to the AU Mic disk prior to the observational findings of Graham et al. (2007), who showed that the disk’s scattered light is strongly polarized, and that porous grains are required to fit the polarization profile. In this chapter, we examine the disk structure predicted by the birth ring scenario in light of the currently available observational data. After a brief review of the predictions for compact grains, we probe modifications to the theory given the porous grains of our best-fit model and check the consistency of the theory’s features with those of our Monte Carlo radiative transfer model. In this context, we appraise the predictive power of the observations to determine \dot{M}_* via inferences of the size and space distributions of grains.

The Theoretical Scenario

We first recapitulate the basic physical arguments of the model put forth by SC06. Collisions occur within the ring of parent bodies, producing dust grains. The radial components of forces arising from stellar radiation and wind result in a pressure acting to push grains away from the star, causing blow-out for sufficiently small grains. In contrast, the tangential components of these forces act as a drag mechanism, which for radiative forces is the well-known Poynting-Robertson (PR) drag. Grains dominated by drag forces spiral in toward the star. The competition between these forces and the relative frequency of destructive grain collisions determine the dynamical structure of the disk. In disks dominated by drag forces, (SC06’s “type A”), the action of PR and corpuscular drags fill the region interior to the birth ring with grains that avoid destructive collisions. In disks dominated by collisions (“type B”), this interior is essentially empty, as the pulverized remains of colliding grains

are quickly swept outward. In both cases, the region exterior to the birth ring is largely populated by the small, tenuously bound grains which follow elliptical orbits with periastra near the birth ring. In type B disks, these grains are just larger than the blow-out size of stellar wind and radiation pressure. In type A disks, the smallest grains are pulled inward by corpuscular and PR drag, and the peak of the grain size distribution in the outer disk corresponds to a size significantly larger than that of blow-out.

SC06 developed analytical and numerical descriptions of the results of these processes on the size-space distributions of dust grains, and then applied this theoretical framework to the case of AU Mic. They postulate a belt of parent bodies at 43 AU, a location determined by the surface brightness profile break in *HST* imaging. By simultaneously modeling the scattered light profiles (*F606W*-band from K05 and *H*-band from M05) and the SED with compact spheres of pure water ice, they determine that type B conditions hold and place limits on \dot{M}_* . With these assumptions on grain type, there are two pieces of evidence for an inner disk devoid of in-spiraling grains, which is expected for type B conditions: (1) a lack of photospheric excess in the $10\ \mu\text{m}$ region of the SED, and (2) the shallow slope of the surface brightness profile at projected distances interior to the proposed ring. Augereau & Beust (2006) argue for a similar dynamical scenario for explaining the observed structure, where corpuscular pressure forces sweep grains outward. Considering the pressure from the stellar wind (and additional radiative enhancement by stellar flares), they determine that radial forces can sufficiently diffuse small grains into the outer regions to account for the observed profile break, in analogy with the dominance of radiation pressure in β Pic's disk.

Potential Ramifications of Porous Grains

It is important to examine the birth ring scenario in view of the new constraints on scattering properties from recent imaging of the disk in polarized light (Graham et al. 2007). The polarization data strongly indicate the presence of porous grains scattering in the Rayleigh regime, reaffirmed in our modeling (§5.4.1). Such grains are largely forward-scattering and produce the required high peak polarization frac-

tion. Since scattering asymmetry directly affects the inferred spatial distribution of grains, previous models' use of spheres of solid material must be re-evaluated with this new evidence. We also stress that, as noted in §5.3.2, analyses involving surface brightness profiles require consistent methodology across all data sets. Following these points, it is appropriate to both check the consistency of the model by SC06 with our porous grain Monte Carlo model, and to evaluate the strength of such models for inference of AU Mic's stellar mass-loss rate.

In approaching this problem, it is apt to contrast the relevant properties of the compact and porous grain types we use in the models of §5.4.1. As expected, the porous grains of Mathis & Whiffen (1989) are less dense than the compact grains, at $\rho = 0.5 \text{ g cm}^{-3}$ (compared to 2 g cm^{-3} for Draine & Li 2001 grains). At a given size, the porous grains also couple less efficiently to the radiation field than their compact counterparts. Taking a $0.05 \mu\text{m}$ grain as an example, the effective cross section for radiation pressure ($Q_{\text{pr}}\pi a^2$) is more than an order of magnitude smaller for a porous grain: $Q_{\text{pr}} \sim 2 \rightarrow 0.05$ when changing from compact to porous. This coupling inefficiency is similarly manifested in a decrease in the effective cross section to scattering, $Q_{\text{sca}}\pi a^2$, for porous grains.

Debris disk structure is commonly parameterized by the vertical optical depth. In the following analysis, we will refer to both the vertical optical depth to scattering, $\tau_{\perp}^{\text{sca}}$, and the geometric vertical optical depth, $\tau_{\perp}^{\text{geo}}$. The former quantity is useful for describing the 1-d brightness profile, while the latter governs the collisional timescale. For a given surface mass density Σ , the depth $\tau_{\perp}^{\text{geo}}$ depends only on the grain density and size distribution dN/da , while $\tau_{\perp}^{\text{sca}}$ additionally depends on scattering efficiency:

$$\tau_{\perp}^{\text{geo}}(r) \propto \frac{\Sigma(r)}{\rho} \int (\pi a^2) \frac{dN}{da} da, \quad (5.10)$$

$$\tau_{\perp}^{\text{sca}}(r) \propto \frac{\Sigma(r)}{\rho} \int [Q_{\text{sca}}(a)\pi a^2] \frac{dN}{da} da. \quad (5.11)$$

For a given grain type and size distribution, $\tau_{\perp}^{\text{geo}}$ and $\tau_{\perp}^{\text{sca}}$ can differ by orders of magnitude. As an example, consider the outer region of porous grains in our model from the previous section. While the size distribution is steep ($dN/da \propto a^{-4.1}$), because $Q_{\text{sca}}(1 \mu\text{m}) \gg Q_{\text{sca}}(0.05 \mu\text{m})$, micron-sized grains constitute the bulk of τ_{sca} despite their relative scarcity. The geometric depth τ_{geo} , on the other hand, is

dominated by the smallest grains, resulting in $\tau_{\text{geo}} \gg \tau_{\text{sca}}$.

Disk Structure Analysis: Theoretical Considerations

The models of SC06 delineate three regions of water ice grains: (1) a birth ring, populated by parent bodies of sizes up to ~ 10 cm, (2) an outer region made up of smaller grains ($a_{\text{min}} \lesssim 1 \mu\text{m}$) on loosely bound orbits, and in type A disks, (3) an inner region of grains, $\lesssim \mu\text{m}$ size, spiraling inward as a result of corpuscular and PR drag forces. Grains smaller than the stellar wind and radiation pressure blow-out size, a_{min} ($\sim 0.1 \mu\text{m}$), have negligible contribution to the disk. Our modeling of the dust distribution with porous grains (§5.4.1) shows that a two-zone architecture (lacking an inner region of drag-dominated grains) is consistent with the observations and, qualitatively, with the architecture predicted by physically modeling dust generated by a belt of parent bodies.

In the birth ring model, how does the expected grain size distribution change in light of the differences between the Mathis & Whiffen (1989) grains and water ice spheres? We first consider a_{blow} , which is determined by the combined action of radiation and stellar wind pressures. The density decrease of porous grains relative to spheres tends to increase a_{blow} . However, this effect is offset by the decrease in the effective cross section, parameterized by Q_{pr} (a factor for 40 lower for $a = 0.05 \mu\text{m}$ grains), resulting in a net decrease of porous grains' blow-out size relative to their compact counterparts. Rewriting SC06's Eqs. 7 and 8, the blow-out size assuming constant pressure is

$$a_{\text{blow}} = \frac{3}{8\pi} \frac{L_*}{GM_*c\rho} \left(Q_{\text{pr}} + Q_{\text{wind}} \frac{\dot{M}_* v_{\text{wind}} c}{L_*} \right). \quad (5.12)$$

We follow SC06 in adopting $v_{\text{wind}} = 450 \text{ km s}^{-1}$ and $\dot{M}_{\odot} = 2 \times 10^{-14} M_{\odot} \text{ yr}^{-1}$. We choose $L = 0.12 L_{\odot}$ and assume that the cross section to wind ($Q_{\text{wind}} \pi a^2$) is unchanged ($Q_{\text{wind}} = 1$) for the porous grains. Together these yield $a_{\text{blow}} = \{0.029, 0.047, 0.23, 2.1\} \mu\text{m}$ for $\dot{M}_* = \{1, 10, 10^2, 10^3\} \dot{M}_{\odot}$. The minimum grain size in the outer region of our disk model ($0.05 \mu\text{m}$) is larger than a_{blow} for the weaker stellar winds, which suggests $\dot{M}_* \ll 10^2 \dot{M}_{\odot}$.

Next, we consider the implications of our porous grain model on the amount of disk infill (type A vs. B) predicted by the birth ring theory — a process regulated by the collision rate, which depends on $\tau_{\perp}^{\text{geo}}$ (Eq. 5.10). In our model for the scattered light at $r_{\text{BR}} = 40 \text{ AU}$, the smallest grains contribute the bulk of the total geometric cross section. The abundance of these grains increases $\tau_{\perp}^{\text{geo}}$ at the birth ring relative to the SC06 value by a factor of 10, to $\tau_{\perp}^{\text{geo}}(r_{\text{BR}}) = 4 \times 10^{-2}$. This shortens the timescale for destructive collisions of the average particle, assuming the specific collisional energy is unchanged. The collisional timescale is balanced by the drag-induced infall time at a grain size defined by a_{break} (cf. SC06 Eqs. 36–37). Grains near this size constitute the bulk of $\tau_{\perp}^{\text{geo}}(r_{\text{BR}})$, and in equilibrium, grains of sizes $a_{\text{blow}} < a < a_{\text{break}}$ fill the interior ($r < r_{\text{BR}}$). Like the case of compact ice spheres, for porous grains we find that a_{break} is the same order as a_{blow} : $a_{\text{break}} = \{1.005, 1.03, 1.08, 1.1\} a_{\text{blow}}$ for a peak geometric vertical optical depth at r_{BR} and the same stellar wind values. In contrast to SC06’s results for the compact grain case, we find that $(a_{\text{break}} - a_{\text{blow}}) < a_{\text{blow}}$ for porous grains in all wind cases, including stronger values. The implication of this result is that no amount of corpuscular drag will produce a significant fraction of grains with orbits crossing the inner region, favoring a clear inner disk (type B).

Disk Structure Analysis: Observational Limits on Infill

As a complementary approach to examining the birth ring scenario, we can, for the moment, set aside the final conclusion of the previous section and use our model from §5.4.1 to test allowed small-grain infill. When using MCFOST to model the observed disk with porous grains, can we make a distinction between the conditions of type A and B? By definition, our two-zone model lacks grains inward of the putative birth ring, consistent with a collisionally dominated type B disk. To test whether the system could be consistent with type A, we now consider adding a third region of grains. If a significant mass of small grains are present inward of $\sim 35 \text{ AU}$ (type A), then these warmer grains would increase dust emission in the 10–20 μm region of the SED and add to the scattered light of the system (Figs. 5.11–5.12). We note that, compared to more isotropically scattering spheres, the strong forward scattering of

porous grains allows us to hide more mass in this region without strongly affecting the total intensity of scattered light. The smallest projected separations, where the added contribution from forward scattering would be maximal, are lost in the glare of the central star and are behind the occulting spot.

The additional zone of porous grains has a flat $\Sigma(r) \propto r^0$ density profile and ranges from 15–35 AU. The inner cutoff corresponds to the estimate of the ice boundary by M05 (13–15 AU). As a general feature of the birth ring conditions modeled by SC06, the outer region’s grains have $a_{\min} \sim a_{\text{break}} \sim a_{\text{blow}}$; therefore we model a single-sized population of $a = 0.05 \mu\text{m}$ grains in this new inner region. The middle and outer regions’ dust distributions were fixed to the best-fit parameters (Table 5.4), and we adjusted the mass in the new inner region in ~ 0.5 dex steps until the scattered light profiles (including fractional polarization) or SED showed significant deviation. We found that the SED first showed noticeable deviation at $M = 10^{-5} M_{\oplus}$; this is an upper limit to the mass of grains in this population allowed by the observations.

We can express this limit as either the geometric or scattering vertical optical depths relative to the peak depth in the birth ring, $\zeta \equiv \tau_{\perp}(r < r_{\text{BR}})/\tau_{\perp}(r_{\text{BR}})$. The geometric vertical optical depth is more closely related to the dynamical structure, while the scattering depth is traced by our imaging observables. As noted in §5.4.2, these geometric and scattering optical depths can be quite different. We find $\tau_{\perp}^{\text{geo}}(r < r_{\text{BR}}) \lesssim 2.5 \times 10^{-2}$, giving $\zeta_{\text{geo}} \lesssim 0.6$. While our limit to ζ_{geo} is order unity, the strong decline in Q_{sca} with grain size results in a more stringent limit to ζ_{sca} for $0.05 \mu\text{m}$ grain filling. An inner mass of $3 \times 10^{-5} M_{\oplus}$, easily ruled out by our analysis, corresponds to $\zeta_{\text{sca}} \sim 1/400$. This is the same order as the limit of Graham et al. (2007), who determined $\zeta_{\text{sca}} \lesssim 1/300$ inward of 40 AU using a similar method (though without SED modeling).

While the limit for ζ_{sca} implies an inner disk relatively free of scattering grains, the relevant quantity for the dynamical structure of the disk is ζ_{geo} . The weakness of our geometric optical depth ratio limit implies that we cannot yet determine type A vs. B dynamics or make inferences of \dot{M}_{*} by matching the expected disk structure to current scattered light and SED data. Rather, perhaps the strongest

direct observational evidence for a type A disk would come from resolved thermal emission from this zone.

Future Considerations

When considering more rigorous tests of birth ring theory, several enhancements can be made to our simple disk model. Faithful models must not rely on an artificial separation between the site of dust production (inner, large-grain region) and the small grains, as we have done in §5.4.1. SC06 also predict different asymptotic power-laws for the outer region’s geometric vertical optical depth in type A and B disks (-2.5 and -1.5, respectively). However, the corresponding asymptotes in scattered light profiles are not reached until distances of a few 100 AU, ruling out reliable comparisons with current data. Somewhat more challenging aspects of the theory are grain size distributions that do not follow power-law description (cf. Fig. 3 of SC06). The prediction of SC06 is an excess of grains above the Dohnanyi collisional cascade ($dn \propto a^{-7/2} da$) for sizes near a_{blow} . Incorporating a population of grains at this size, in addition to the power-law size distribution, is a possible avenue for future significance testing. Both SC06 and Augereau & Beust (2006) predict diminishing minimum grain size with increasing stellar distance (due to ever-more tenuously bound grains as a result of stellar wind and radiation pressure), which can effectively model the observed blue color gradient in the outer region. Future scattered light modeling may incorporate a function $a_{\text{min}}(r)$ in the outer zone.

5.5 Discussion & Conclusions

Debris disks are a long-lived phase in the evolution of circumstellar material, and they provide indirect probes for the presence of planets and planetesimals. Resolved imaging is crucial for determining the structure and dynamical history of the dust. In our near-IR imaging, we measured the structure of the disk seen in scattered light. We confirmed the overall architecture of the disk seen in H band by L04 and M05, and presented the first images seen in J and K' (§5.3.1). We represented the global disk structure with a power-law description of the midplane surface brightness, and

noted that discretion must be used when comparing between profiles measured in different manners (§5.3.2). Scattered light features on both large and small scales are largely consistent across the bands studied here. The colors we measured in the surface brightness profiles (§5.3.3) allow inferences of the scattering properties, which are determined by the composition, sizes, and structures of dust grains.

We used a model for the space and size distributions of the grains to reproduce these profiles and the SED (§5.4.1). The simple, two-zone description of power-law grain distributions cannot faithfully reproduce the observations with compact silicate grains. Rather, porous grains of dirty ice, whose presence is indicated by recent polarization measurements (Graham et al. 2007), have optical constants with which we can match such an architecture to the data with reasonable fidelity. The key degeneracy is between the scattering phase function and the density distribution. Models of K05 and M05 place grains which exhibit moderate scattering asymmetry in the inner regions of the disk. The porous grains in the outer zone of our model, which are larger and more forward scattering than the compact grains used in previous efforts, fill in this region of scattered light. As such, our modeling does not require grains inward of 35 AU to reproduce the midplane surface brightness profiles. The inner zone (35–40 AU) of our model is made up of few-mm-sized grains, which reproduce the far-IR end of the SED. The outer zone grains of our model are smaller (0.05–3.0 μm) and produce the majority of the mid-IR emission and the scattered light.

The blue color of the scattered light disk is relatively rare among resolved systems (cf. Table 1 of Meyer et al. 2007). The succession of modeling efforts have shown that a significant population of submicron grains reproduces the disk’s blue scattered-light color, and that the presence of such grains is compatible with interpretations of the disk’s dynamical structure. As other authors have noted, stellar properties play a major role in the removal of submicron grains. As an M dwarf, AU Mic has a uniquely low radiation pressure relative to other stars with scattered-light debris disks. For sufficiently low values of \dot{M}_* , we find a_{blow} is submicron and grains will scatter blue. While stellar properties can reasonably be used as a predictor for the presence of submicron grains in debris systems, grain properties can also

affect the blow-out size. As we noted in §5.4.2, the smallest of our porous grains have much smaller Q_{pr} relative to their compact counterparts of the same size. The blow-out sizes we calculate for porous grains are up to a factor of eight smaller than those of compact grains (as computed by SC06). When blue scattered-light colors are detected around earlier-type stars with stronger radiation pressure (e.g. HD 32297 and HD 15115; Kalas 2005; Kalas et al. 2007), inferences of submicron grains may constrain their porosity and composition (see also Artymowicz 1988; Grigorieva et al. 2007).

The study of debris disk evolution hinges on accurate measurements of stellar ages and dust masses. The total observed mass of the disk in our model ($1.0 \times 10^{-2} M_{\oplus}$) is dominated by the mm-sized grains in the inner zone. Note that this is a factor of few times smaller than the mass we derive for compact grains ($2.7 \times 10^{-2} M_{\oplus}$). Though the equilibrium temperatures for the two grain types differ, this is primarily an opacity effect (Voshchinnikov et al. 2006). The decrease in density increases the opacity, which in turn lowers the mass needed to match the sub-mm fluxes. Since these grains contribute little to the scattered light, we have no information about their porosity (and correspondingly whether any compaction has occurred). Therefore, in addition to the normal caveats about dust masses derived from sub-mm fluxes (e.g. insensitivity to larger bodies), derived debris disk masses are additionally uncertain by a factor of a few depending on the grain porosity. The same opacity caveat applies to the inferred sizes of the grains that dominate the sub-mm emission. In the inner region, our porous grains are a factor of three larger than the equivalent best-fit compact ones — the increased opacity means a larger size is needed to match a given temperature.

Nevertheless, we can compare our dust masses to those of other authors. Our estimate is similar to the mass estimated by a single-temperature fit to the long-wavelength SED by Liu et al. (2004), who found $1.1 \times 10^{-2} M_{\oplus}$ of 40 K dust at 17 AU. M05 found a similar mass as Liu et al., for single-zone power-law distributions of size and density of ISM-like grains. Augereau & Beust (2006) calculate a mass of $7 \times 10^{-3} M_{\oplus}$ by adjusting the grain size distribution in their scattered light model in order to match the long-wavelength SED. Finally, SC06 argue for parent

body sizes up to 10 cm, the maximum size participating in a steady-state collisional cascade. For their model’s size distribution, the mass of parent bodies is $\sim 10^{-2} M_{\oplus}$. However, current observations are not sensitive to grains larger than a few mm, so the maximum observed mass in this model is significantly lower. For size distribution index $\gamma = -7/2$, the mass $M \propto a_{\max}^{1/2}$, and the observable portion of SC06’s mass is a few times smaller than that of our work.

The interpretation of debris disk observations for inferring the presence of planets and the history of the grains rests on sound physical modeling of grain dynamics. The overall shape of the midplane surface brightness profile distribution is consistent with steady-state dynamics arising from a ring of parent bodies (§5.4.2). With models of grain dynamics, we might constrain \dot{M} by examining the density of small grains in the inner disk ($\lesssim 35$ AU). We found that for the porous grains in our model, an inner region would be populated primarily by grains just above the blow-out size for a wide range of \dot{M}_* . Further, the constraint of the presence of grains in an inner region is set by the mid-IR SED, and we can only say that the geometric vertical optical depth in this region is at most the same order as the peak depth in the birth ring, consistent with both drag- and collision-dominated (type A and B) disks. However, the presence of small ($0.05 \mu\text{m}$) grains in the outer region implies that the mass-loss rate is low enough such that these grains survive blow-out, i.e. $\dot{M}_* \ll 10^2 \dot{M}_{\odot}$.

The overall disk architecture inferred from these models has implications for the substructure seen in scattered light. In §5.3.4, we compared our measurements of features A–E with the results of other authors, giving further evidence that they are not artifacts of stellar PSF subtraction. Additional brightness enhancements located 11–15 AU from the star have also been identified, though additional observations of the disk at small angles are needed to improve confidence. The appearance of such substructural features is determined by the grain distribution; since the bulk of the scattered light comes from small grains beyond ~ 40 AU, the features at projected distances inward of 40 AU must arise from azimuthal perturbations in the dust distribution beyond this distance. Some of these features appear to exhibit a wavelength-dependent position. (We note the position of feature D, which is closest

to 40 AU, does not appear to do so.) While the overall position of a feature may be used to trace a perturbation in the density distribution in the outer disk, the wavelength dependence of the position may constrain additional spatial variation in the grain size distribution. In a similar vein, any vertical structure associated with a given feature (Fig. 5.5) can be tied to the vertical structure of the outer disk.

In summary, we:

1. Demonstrate a new roll-subtraction technique that attempts to mitigate AO PSF variability (§5.2.2),
2. Detect the AU Mic debris disk in JHK' -band imaging and place an upper limit on the L' -band brightness distribution (§5.3.1),
3. Confirm the blue color of the disk and measured a blue color gradient outside of the transition radius (§5.3.2-5.3.3),
4. Place detection limits on point sources in the disk midplane (§5.3.5) and document a technique for determining point-source detection sensitivity in the disk midplane (§5.3.5),
5. Verified the presence of substructure in the inner disk, and shown that some features exhibit slight variation in their positions with wavelength (§5.3.4),
6. Demonstrate the applicability of a simple two-zone model which simultaneously fits the scattered light profiles and SED (§5.4.1),
7. Find that compact silicate grains cannot be used in our simple model, while porous, icy aggregates of silicate and carbonaceous grains can reasonably account for the observed thermal and scattered light (§5.4.1),
8. Determine that a two-zone model is consistent with steady-state grain dynamics dominated by collisions (SC06 type B; §5.4.2),
9. Show that, by relying on models of the inner disk ($r \lesssim 35$ AU) structure, we cannot place strong limits on the geometric vertical optical depth of small

($0.05 \mu\text{m}$) porous grains interior to the birth ring and therefore cannot yet constrain \dot{M}_* from this approach alone (§5.4.2), and

10. Show that the blow-out size for porous grains is consistent with modeled grain size distribution for $\dot{M}_* \ll 10^2 \dot{M}_\odot$ (§5.4.2).

The next modeling steps will seek to utilize all available imaging and SED data. We note in particular that measurements of scattering in polarized light provide strong, complementary constraints on the composition and distribution of dust in this system. Future work will incorporate fitting to scattered light images rather than surface brightness profiles, and will begin to probe the vertical structure of the disk while taking into account the effects of projection and blurring by the PSF. Finally, we emphasize that the global structure of the debris can be explained by steady-state dust production and diffusion, and we need not invoke a planet to clear the inner region of dust. However, the mechanisms responsible for maintaining the structure of parent bodies in the birth ring as well as the dust substructure remain undetermined.

Chapter 6

A Ring of Warm Dust in the HD 32297 Debris Disk

6.1 Introduction

The attrition of the primitive remnants of solar system formation replenishes the dust in circumstellar debris disks. The scattered light and thermal emission from this dust provide a window into the physical processes governing the evolution of solid material around normal stars, at a time after they have shed their primordial gas and dust envelopes and are transitioning to more mature, nearly dust-free systems (e.g. Backman & Paresce 1993; Meyer et al. 2007).

HD 32297 ($d = 112_{-12}^{+15}$ pc; Perryman et al. 1997) is a main-sequence star with a recently discovered circumstellar disk. Schneider et al. (2005) first resolved the dust in near-IR scattered light with *HST*/NICMOS (*F110W*). They detected the near-edge-on inner disk out to $3''.3$ (~ 400 AU), and found a brightness asymmetry inward of $0''.5$ and a break in the surface brightness profile at $1''.7$. Optical confirmation of the scattered-light disk by Kalas (2005) followed, revealing an extended, asymmetric outer disk extending to $15''$ (~ 1680 AU) and suggesting a blue-scattering R -[F110W] dust color. Redfield (2007) detected the gaseous component of the disk, finding that HD 32297 exhibits the strongest Na I absorption of any nearby main-sequence debris disk system.

We report our discovery of spatially resolved emission arising from warm dust surrounding HD 32297 (§6.2), and note the independent discovery of resolved thermal emission by Moerchen et al. (2007b). We examine the morphology of the observed dust emission by removing the direct stellar contribution and determine that the residual structure suggests a model of thermal emission from an optically thin ring. We fit such a model to the data and explore the allowed parameter distribution (§6.3). To conclude, we consider the implications of these findings in the context of physical processes shaping the disk’s physical structure (§6.4).

6.2 Observations

We observed HD 32297 and HD 20893 with MICHELLE on the Gemini-N telescope on the night of 2006 September 19 (GN-2006B-C-12). HD 20893 serves as the photometric calibrator and point spread function (PSF) reference. We imaged these stars in the N' filter ($\lambda_0 = 11.2 \mu\text{m}$, $\Delta\lambda = 2.4 \mu\text{m}$) in a chop-nod sequence with a $15''$ throw. Observations were chopped and nodded at a position angle (PA) of 120° , chosen to be roughly perpendicular to the scattered light disk (PA = $47^\circ.6 \pm 1^\circ$; G. Schneider, 2005, private communication). Image quality was good (N' -band resolution $\sim 0''.3$), though terrestrial cirrus contributed to a varying background level which sometimes saturated the detector. The ABBA chop-nod sequences which contained saturated frames were discarded. Of the 188 s (23.5 s) of guided, on-source integration time for HD 32297 (HD 20893), 94.0 s (23.5 s) was used in the final analysis. Each ABBA sequence was processed to remove both the sky and instrumental backgrounds via a double difference. The central, guided images resulting from each ABBA double difference were registered and stacked.

Photometric calibration was performed with HD 20893, which is a Cohen et al. (1999) standard with a zero-airmass mean N' -band flux density of $4.29 \pm 0.14 \text{ Jy}$ at an isophotal wavelength of $11.23 \mu\text{m}$. The mean airmass during the HD 32297 exposures was $\sim 11\%$ greater than during the HD 20893 exposures, and we assumed an extinction of $0.172 \text{ mag AM}^{-1}$ (corresponding to a mean N -band [$\lambda_0 = 10.0 \mu\text{m}$, $\Delta\lambda = 5 \mu\text{m}$] Mauna Kea extinction; Krisciunas et al. 1987) when correcting the

measured HD 32297 fluxes.

6.3 Results & Analysis

The resulting images are shown in Figure 6.1. The image of HD 32297 exhibits extension consistent with the direction of the scattered light disk. The extended emission is detected out to the sensitivity limit at $\sim 1''$. With a $1''.4$ radius aperture and an encircled energy correction derived from the image of HD 20893, we measured the total flux of the star and disk to be 49.9 ± 2.1 mJy. The uncertainty includes the contribution from both the background noise and the zero point uncertainty derived from HD 20893. As the filter is relatively narrow, a color-correction to this monochromatic flux density was not considered necessary. We place the measurement of total flux in relation to the known SED in Figure 6.2.

6.3.1 Stellar Properties

In order to characterize the dust emission, we must (1) estimate the fraction of the observed N' flux attributable to the star, and (2) estimate the stellar luminosity, which affects the temperature balance of the grains. To these ends, we characterize the star by modeling the optical and near-IR portion of the SED, given by Tycho-2 and 2MASS photometry (Høg et al. 2000; Skrutskie et al. 2006). For model comparison, we synthesized photometry with the stellar atmospheres of the NEXTGEN grid (Hauschildt et al. 1999). The scaling for the resulting photospheric fluxes, parameterized by $\xi \equiv (R_*/d)^2$, was least-squares fit to match the synthetic photometry to the optical/near-IR data. The choice of model atmosphere parameters is unclear at first glance, since the spectral type of HD 32297 is inconsistent in the literature. It was classified as A0 by Cannon & Pickering in the Henry Draper Catalog, while it specified as A5 in the AGK3 Catalog (Heckmann 1975). Assuming no interstellar extinction, $\log g = 4.5$, and $[\text{Fe}/\text{H}] = 0$, we found that a $T_{\text{eff}} = 9600$ K spectrum (appropriate for A0V) is clearly rejected by the photometry ($\chi^2_{\nu} = 200$), while a 7600 K NEXTGEN model fit the data best ($\chi^2_{\nu} = 2.5$). The resulting best-fit model is shown in Figure 6.2.

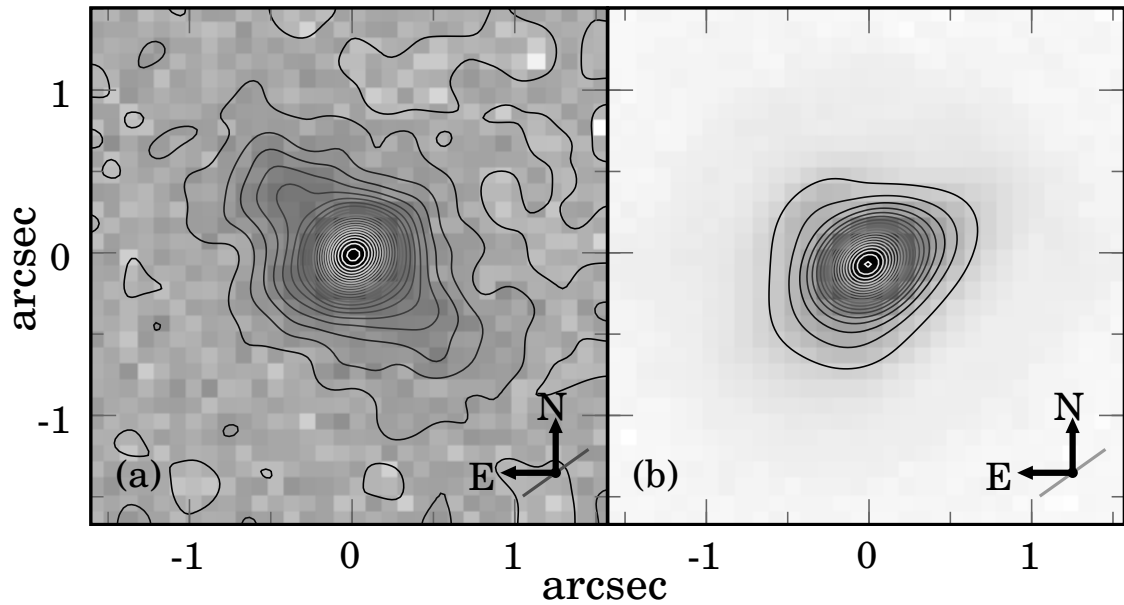


Figure 6.1 Panel (a) displays the result of our Gemini-N/MICHELLE imaging of the HD 32297 debris disk (N' band), showing elongated emission around the star. Contours are spaced according to the $1\text{-}\sigma$ background noise level. The elongation PA is consistent with the scattered light disk. The chop direction is indicated by the grey line on the compass. Panel (b) shows the image of the reference star HD 20893. The contour spacing is selected to match those in (a) relative to the stellar flux.

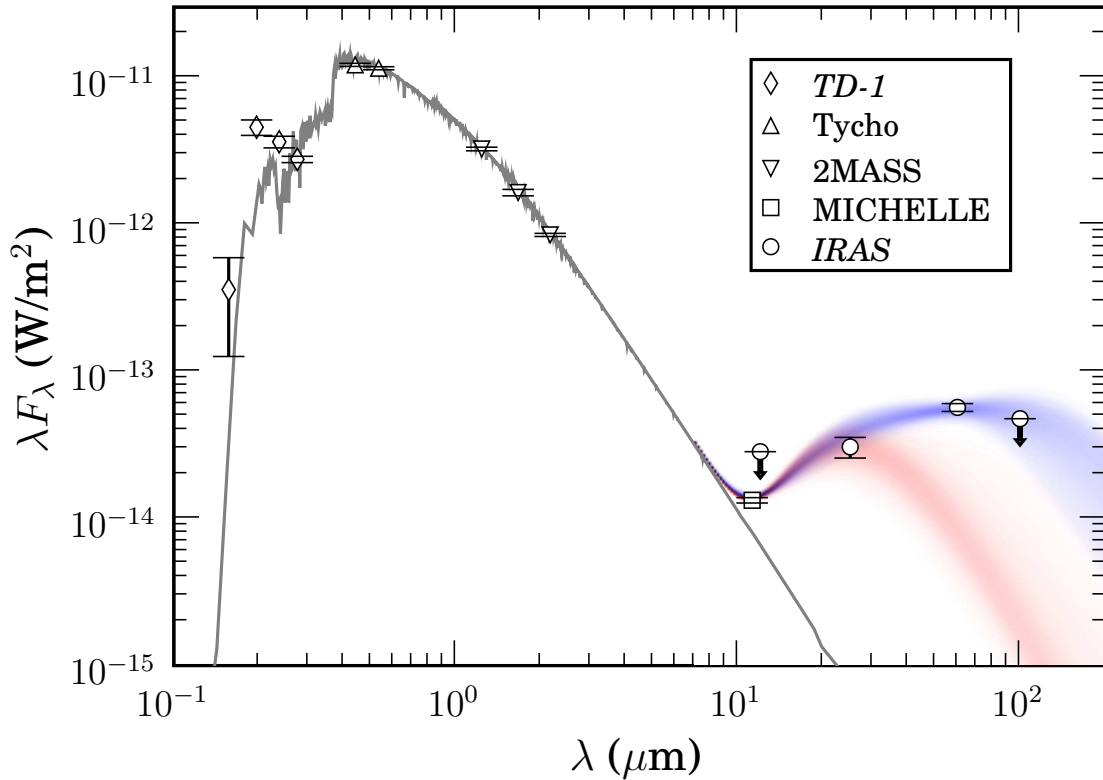


Figure 6.2 The SED of the HD 32297 system. *IRAS* photometry is from Moór et al. (2006) (see also Silverstone 2000). Near-IR data is from 2MASS (Skrutskie et al. 2006), optical data from Tycho-2 (Høg et al. 2000), and UV data from *TD-1* (Thompson et al. 1978). A 7600 K NEXTEGEN model photosphere (Hauschildt et al. 1999) with zero foreground extinction was fit to the optical-NIR photometry. The range of allowed dust emission from Model I is shown in blue, while that of Model II is shown in red (§6.3.3). Model I fits for the image and all SED points, while Model II treats the 60 μm measurement as an upper limit, effectively allowing for a separate population of cool dust.

Can interstellar reddening bias our inferred T_{eff} ? At ~ 112 pc, the star may be outside the relatively dust-free Local Bubble, which Redfield (2007) notes is expected to extend to ~ 90 pc in this direction (Lallement et al. 2003). As an empirical test, we fit for the extinction (parameterized by A_V) using the A_λ/A_V law of Fitzpatrick (2004) and assuming $R_V = 3.1$. The best-fit model, fixing $T_{\text{eff}} = 9600$ K, gives $A_V = 0.72 \pm 0.02$ mag (formal error) and is rejected with $\chi_\nu^2 = 8.5$.¹ When adjusting T_{eff} , the 7600 K model again minimizes χ^2 , with a best-fit $A_V = 0.026 \pm 0.024$ mag at this temperature. Thus, we empirically determine that the observations are consistent with zero interstellar extinction.

As an alternative approach to inferring the amount of interstellar dust toward the star, we consider the measurement of the interstellar component of Na I absorption by Redfield (2007). He measures a column density of $N_{\text{NaI}} \sim 10^{12}$ cm⁻². There is considerable scatter in the correlation between N_{NaI} and $E(B-V)$, and assuming $R_V = 3.1$, values of $A_V = 0.03$ to 0.3 mag are reasonable (Fig. 4d of Hobbs 1974). Since this is consistent with a small amount of extinction, we do not alter our conclusions.

We estimate the flux scaling $\xi = (7.22 \pm 0.14) \times 10^{-20}$ from the best-fit zero-extinction model (after scaling the formal uncertainty by $\sqrt{\chi_\nu^2}$). Using this quantity, we calculate the monochromatic flux density $F_\nu(11.23 \mu\text{m}) = 28.2 \pm 0.6$ mJy. The uncertainties in our estimates of the stellar radius and luminosity are dominated by distance errors, as

$$L_* = 4\pi\xi d^2 \sigma T_{\text{eff}}^4. \quad (6.1)$$

Taking the best estimates $\xi = 7.22 \times 10^{-20}$ and $d = 112$ pc, we find $R_* = 1.34 R_\odot$ and $L_* = 5.4 L_\odot$. Together, these suggest the literature value of A5 is closer to the “true” classification, though the cool temperature we estimate suggests even later A subclasses. As noted by Schneider et al. (2005), the star lies near the bottom of the A star main sequence in a color-magnitude diagram, a property in common with other young debris disk systems (Jura et al. 1998). Figure 2 of Moór et al. (2006) shows that HD 32297 is relatively under-luminous and is positioned toward

¹With the addition of A_V as a parameter, the number of degrees of freedom ν has decreased relative to previous fits.

the red end of the local A star sequence, consistent with our results. A modern high-resolution spectrum can settle the debate over the correct stellar classification.

Finally, we note the ultraviolet measurements from the *TD-1* satellite (Thompson et al. 1978) shown in Figure 6.2. We did not use these data in our photometric fit. The *F1965* and *F2356* bands ($\lambda = 196.5$ and 235.6 nm, respectively) show excess above the model photosphere. These may be due to line emission — such as Si III] and C III] in the former band, and Fe II in the latter — similar to what is seen in T Tauri stars (e.g. Lamzin 2000a; Valenti et al. 2003). In such stars, the intercombinational lines are likely associated with accretion rather than the chromosphere (Lamzin 2000b). The UV excesses in HD 32297, along with the recent evidence for a gas disk (Redfield 2007), lend indirect support to the contention that this is a young stellar system.

6.3.2 PSF Subtraction

Using the range of ξ estimated in the previous section, we scaled the image of HD 20893 and subtracted it from the that of HD 32297. After PSF subtraction, we find 21.6 ± 2.2 mJy in non-color-corrected residual flux (Fig. 6.3). The residuals suggest the observed image (Fig. 6.1a) is a composite of a bilobed structure and an unresolved central source, whose flux can be fully accounted for by the star. The lobes peak at offsets of $0''.5$ – $0''.6$ from the star, corresponding to a radius of ~ 60 AU. This suggests an inner edge to the population of grains with optically thin N' -band emission — both hotter dust closer to the star and the case of optically thick material would fill in the emission at smaller projected separations.

We quantified the degree of asymmetry between the disk lobes with aperture photometry of the PSF-subtracted disk image (Fig. 6.3c). We used $0''.6$ square apertures placed on each lobe, with centers $0''.6$ from the stellar centroid. Neglecting an aperture correction and calibration uncertainty, we measured a NE-SW flux difference of 0.17 ± 0.36 mJy. As a fraction of the total flux in these apertures, the difference is $(2.0 \pm 4.3) \times 10^{-2}$. We conclude that the disk emission is consistent with symmetry.

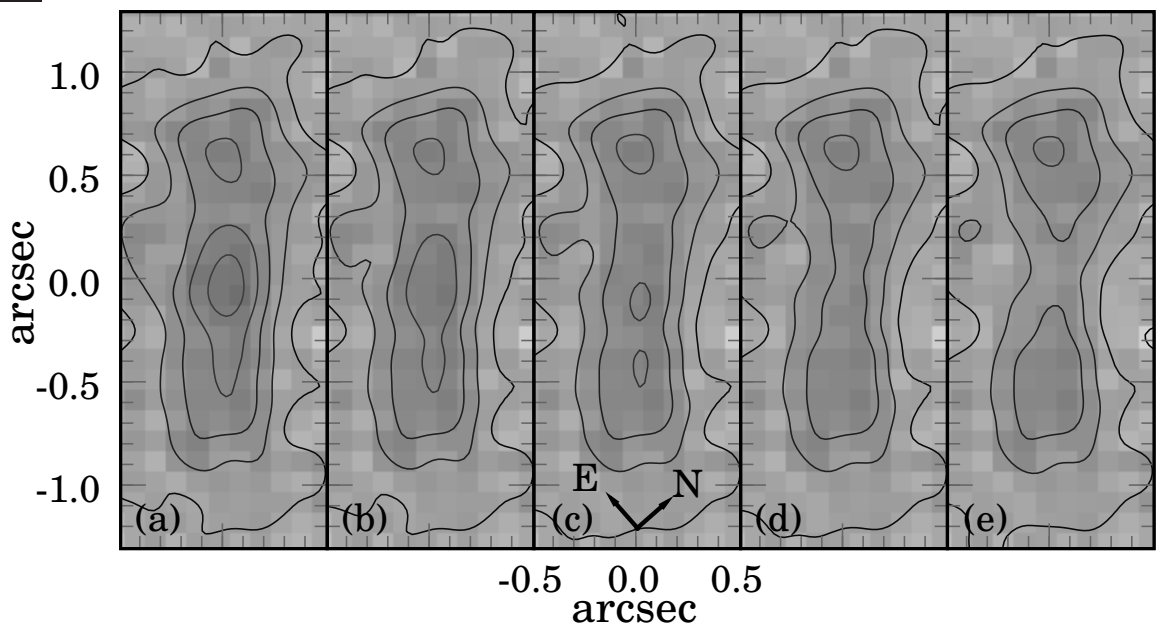


Figure 6.3 Images of the disk with the stellar PSF subtracted for various values of the stellar flux estimate. With $F_\nu^0 \equiv 28.2 \text{ mJy}$ and $\sigma \equiv 1.1 \text{ mJy}$ (which includes both error in our flux estimate, §6.3.1, and N' calibration uncertainty, §6.2), panels (a)–(e) depict subtractions of a central source with $F_\nu = \{F_\nu^0 - 2\sigma, F_\nu^0 - \sigma, F_\nu^0, F_\nu^0 + \sigma, F_\nu^0 + 2\sigma\}$, respectively. As in Fig. 6.1, contours are spaced according to the $1\text{-}\sigma$ background noise level. The bilobed residuals suggest that the system may be modeled as a central star with an optically thin ring of warm material.

6.3.3 Modeling

Model Construction

We adopt the model for thermal emission from optically thin dust rings developed by Backman et al. (1992), which assumes particles of effective size λ_0 that radiate as modified blackbodies with emission efficiencies ϵ_ν . We model the three-dimensional emission of the dust $j_\nu(\mathbf{x})$ by evaluating

$$\alpha_\nu(\mathbf{x}) = \begin{cases} \tau_0 \left(\frac{\varpi}{\varpi_0}\right)^\gamma f\left[z, h_0 \left(\frac{\varpi}{\varpi_0}\right)^\eta\right] & \text{for } \varpi_0 \leq \varpi \leq \varpi_1, \\ 0 & \text{otherwise,} \end{cases} \quad (6.2)$$

$$\epsilon_\nu = \begin{cases} \lambda_0/\lambda & \text{if } \lambda > \lambda_0, \\ 1 & \text{otherwise,} \end{cases} \quad (6.3)$$

$$T(r) = 468 \left(\frac{L_*/L_\odot}{\lambda_0/1\ \mu\text{m}}\right)^{1/5} \left(\frac{r}{1\ \text{AU}}\right)^{-2/5} \text{K}, \quad (6.4)$$

$$j_\nu(\mathbf{x}) = \alpha_\nu(\mathbf{x})\epsilon_\nu B_\nu [T(r)]. \quad (6.5)$$

Here, α_ν is the absorption coefficient, and the function $f(z, h)$ describes the vertical distribution of dust and has scale height h . The fiducial values for the vertical optical depth to absorption τ_0 and scale height h_0 are set at the inner edge of the dust annulus, ϖ_0 . We use cylindrical coordinates for positions \mathbf{x} , with $r^2 = \varpi^2 + z^2$, and assume azimuthal symmetry.

Some assumptions of grain properties are implicit in Equations 6.2–6.5. The disk is assumed to be optically thin at all radii. The particles are efficient absorbers, but inefficient emitters (Eq. 6.3). Backman et al. (1992) discuss the relationship between λ_0 and the particle absorption efficiency and size distribution in their Appendix D. They argue that for “dirty ice” dielectric constants and $dn(a) \propto a^{-7/2} da$ collisional-cascade size distribution (Dohnanyi 1969), the minimum grain size is an uncertain $a_{\min} \sim \lambda_0/6$. With these assumptions, the model contains only minimal information regarding grain characteristics. While we ignore the effects of grain composition with this approach, the absence of evidence for grain mineralogy (e.g. mid-IR spectroscopy) renders consideration of various compositions premature. Future work using more advanced models with explicit dependence on grain sizes and mineralogy may produce significant differences from our results.

For simplicity, we assume the vertical density distribution f is Gaussian, with width $\sigma = h_0 = 10 (d/112 \text{ pc}) \text{ AU}$ fixed at all radii ($\eta = 0$). Because we do not measure a significant brightness asymmetry (§6.3.2), we assume the disk is spatially centered on the star. The distance d is a ‘nuisance’ parameter not directly related to the disk architecture, and in the interest of independence we define $\theta_0 \equiv \varpi_0/d$ (likewise for θ_1). The remaining free parameters are θ_0 , θ_1 , λ_0 , vertical optical depth to absorption $\tau_0 \equiv \tau_{\perp}^{\text{abs}}(\varpi_0)$, (subpixel) stellar centroid \mathbf{x}_* , stellar flux (parameterized by ξ ; §6.3.1), disk inclination i , and PA. The stellar luminosity is given by Eq. 6.1. There are 11 degrees of freedom within the set of model parameters $\Theta = \{d, \mathbf{x}_*, \text{PA}, i, \xi, \gamma, \theta_0, \theta_1, \tau_0, \lambda_0, h_0, \eta\}$.

We construct the density distribution on a three-dimensional grid, with spatial resolution of $0''.05 = 5.6 (d/112 \text{ pc}) \text{ AU}$, which is half the spatial sampling of the MICHELLE detector ($0''.1 \text{ pix}^{-1}$). The emission coefficient j_{ν} (Eq. 6.3) is sampled at the grid points and numerically integrated along each line of sight. As in the simple subtraction in §6.3.2, the PSF is derived from the image of HD 20893 (Fig. 6.1b). We upsample the PSF to match the grid resolution, shift it according to \mathbf{x}_* , and convolve it with the disk model’s integrated emission. These procedures take place in the Fourier domain with their Fourier-equivalent operations via the convolution and shift theorems. We transform back to the image domain and bin the result to the resolution of the instrument (a factor of 2 in each dimension).

Fitting Process

Given the model disk, how do we characterize the range of model parameters allowed by the data? As we have only limited information (e.g. the thermal emission resolved in a single band), we expect that degeneracies will exist between some parameters (such as λ_0 and τ_0). Further, because Eqs. 6.1–6.5 contain significant nonlinearities, we expect non-Gaussianity in the joint distribution of allowed parameters. Finally, this problem contains nuisance parameters (e.g. d) which are unimportant when considering the physical architecture of the disk. These characteristics, combined with a desire to incorporate prior knowledge, suggest a Bayesian approach to model fitting. The range of disk architectures allowed by our simple

model can be described by the joint posterior distribution of model parameters, namely

$$p(\Theta|\mathcal{D}, I) \propto p(\mathcal{D}, \Theta|I) = p(\mathcal{D}|\Theta, I)p(\Theta|I). \quad (6.6)$$

The posterior distribution of parameters is proportional to the likelihood, $p(\mathcal{D}|\Theta, I)$, times the prior, $p(\Theta|I)$. Here, \mathcal{D} represents the observational data and I represents our background information. In this framework, the best-fit model is one whose parameters maximize the posterior distribution (so-called *maximum a posteriori* fitting). The Bayesian approach has previously been used in modeling mid-IR images of debris disks (e.g. Koerner et al. 1998; Wahhaj et al. 2003). A more general comparison of Bayesian and frequentist methods in the context of common astronomical problems is given in Loredo (1992).

Brute-force characterization of this distribution is not computationally efficient. The large number of model parameters ensures that the posterior has a relatively high dimensionality, and grid-based schemes for mapping the posterior require many evaluations of the model. Instead, we turn to Markov chain Monte Carlo (MCMC) methods to more efficiently explore the parameters' joint posterior distribution. We note that these advanced statistical techniques stand in contrast to the relative simplicity of our model; our goal of measuring the ranges of allowed disk architectures motivates the expenditure of computational resources in the exploration of parameter space rather than the complexity of the underlying disk model.

The MCMC framework uses a Markov chain, consisting of a series of states $\{\Theta_n\}$, to explore the parameter space and sample the posterior. A requirement of MCMC methods is an algorithm for randomly choosing states in the Markov chain. Given a state Θ_n , the Metropolis-Hastings algorithm provides a general-purpose method for randomly choosing the subsequent state Θ_{n+1} based on a candidate transition function (commonly Gaussian). Often this algorithm is used in conjunction with the Gibbs sampler, which provides a prescription for choosing which of the model variables to change in each transition. With the Metropolis-Hastings algorithm choosing states, the chain will eventually reach convergence. A key property of converged chains is that the distribution of states approximates the posterior distribution. The use of MCMC in astrophysical data analysis has grown in recent

years; a summary of this technique and an application to quantify uncertainty in orbit fitting is given by Ford (2005).

When addressing questions about the physical properties of the disk, we are sometimes interested only in the range of a subset of parameters allowed by the model. In the Bayesian framework, the distribution of a parameter (or joint distribution of a subset of parameters) is obtained through marginalization. The posterior is integrated over the variables not of interest. For example, to obtain the joint marginal distribution of τ_0 and λ_0 , we integrate over the other variables $\Theta' = \{d, \mathbf{x}_*, \text{PA}, i, \xi, \gamma, \theta_0, \theta_1, h_0, \eta\}$,

$$p(\tau_0, \lambda_0 | \mathcal{D}, I) = \int p(\Theta | \mathcal{D}, I) d\Theta'. \quad (6.7)$$

Having obtained an MCMC chain, this integral is trivial — the joint marginal distribution is simply the joint distribution of the variables’ samples, in this case the distribution of $\{\tau_{0,n}, \lambda_{0,n}\}$.

Having chosen the sampling scheme, we must define the likelihood and prior distributions for our model parameters. We calculate the likelihood by subtracting the model image from the observed emission presented in Fig. 6.1a. We compute χ_{im}^2 for the image fit using the background noise level, and we add the χ_{SED}^2 arising from the *IRAS* SED measurements (including upper limits). The likelihood is then $p(\mathcal{D} | \Theta, I) \propto \exp[-(\chi_{\text{im}}^2 + \chi_{\text{SED}}^2)/2]$.

We have several priors whose product constitutes $p(\Theta | I)$. We use normal priors for the *Hipparcos* parallax (8.92 ± 1.05 mas; a proxy for d) and the stellar flux factor ξ (§6.3.1). We also apply a log-uniform prior to λ_0 , with limits of 1 nm–1 mm, as well as a uniform prior on γ , ranging from -4 to 4. The prior for the outer disk extent θ_1 is taken to be uniform from θ_0 to $200''$. With these likelihood and prior functions, we ran a total of six chains using the Metropolis-Hastings algorithm with the Gibbs sampler. Each chain contained 10^4 samples. The first 10^3 samples were discarded, as the candidate transition function proposal variance for each parameter was adjusted during this “burn-in” period. We expect the Markov chains have converged because no gross deviations exist when comparing the marginal distributions of each parameter across all chains.

In general, the convergence rate and outcome of fitting processes are dependent on starting conditions. Rather than input hand-picked parameters to the MCMC algorithm, we first apply a genetic algorithm (for global optimization) followed by a Levenberg-Marquardt least-squares fit (for local optimization) to find a model of the image with suitable parameters. During this process, the (nuisance) distance is fixed at 112 pc. Examination of the marginal distributions of each parameter shows that the posterior distribution in the region of the global maximum is smooth. As a check for other maxima, we drew 500 randomly distributed samples of Θ over a wide distribution, and performed a least-squares fit with each sample as the starting condition. All fits converged on the same maximum, which suggests the absence of lesser maxima in the posterior distribution.

Results

Using the ring model presented in §6.3.3, we fit the N' -band image, and in the SED the 25 and 60 μm points while respecting the 12 and 100 μm upper limits (Model I). Confidence intervals for the marginal posterior parameter distributions are given in Table 6.1. We are able to obtain a reasonable fit to the image, though the model tends to overpredict the 25 and 100 μm fluxes (Fig. 6.2). With the parameters that maximize the posterior, the χ^2 for the image is 912 (with 32² pixels), while the χ^2 for the *IRAS* SED is 3.3 (with 2 data points and 2 upper limits).

The marginal distributions for the position angle and inclination are approximately normal, with $\text{PA} = 44^\circ.4 \pm 1^\circ.3$ and $i = 90^\circ.0 \pm 2^\circ.4$. The PA is marginally inconsistent with the direction of the inner scattered light disk, though this should not be taken as evidence of separate disks since we did not calibrate the detector orientation. We note that the range of allowed inclinations may be affected by our choice of disk scale height.

The SED data at $\geq 25 \mu\text{m}$ constrain the values of the outer radius θ_1 and density power-law index γ . From the marginal parameter distribution, we find $\theta_1 \gtrsim 30''$, which is further than the scattered light disk has been detected (15''; Kalas 2005). The model also requires $\gamma \simeq 0$, which places a large amount of cool material in the outer disk. With $\lambda_0 \simeq 0.2 \mu\text{m}$, giving $a_{\text{min}} \ll 1 \mu\text{m}$, we can infer this to

Table 6.1. Best-Fit Model Parameters

parameter	Model I	Model II	Notes
PA	$44.5^{+2.6}_{-2.5}$	44.5 ± 2.5	...
i	90.0 ± 4.7	90.0 ± 4.8	...
ξ	1.02 ± 0.03	1.03 ± 0.03	$\times 7.22 \times 10^{-20}$
γ	0.07 ± 0.22	$-2.1^{+2.2}_{-1.7}$	^a
θ_0	$0'.54^{+0.05}_{-0.07}$	$0'.65^{+0.06}_{-0.09}$...
θ_1	$> 33''$	$> 1''.8$...
$\log_{10}(\tau_0)$	$-2.57^{+0.24}_{-0.30}$	$-1.94^{+0.27}_{-0.49}$...
$\log_{10}(\lambda_0/1\mu\text{m})$	$-0.65^{+0.21}_{-0.27}$	$-0.41^{+0.15}_{-0.22}$...
Dependent or fixed parameters:			
h_0	$10(d/112\text{ pc})\text{ AU}$...
η	0		...
ϖ_0	61^{+20}_{-13} AU	73^{+23}_{-16} AU	...
ϖ_1	$> 3700\text{ AU}$	$> 210\text{ AU}$...
$T(\varpi_0)$	171^{+31}_{-19} K	142^{+21}_{-11} K	...

^a Lower-limit in Model II set by prior.

Note. — 95% confidence intervals for marginal posterior distributions. PA, position angle; i , inclination; $\xi = (R_*/d)^2$, stellar flux parameter; γ , surface density power law index; $\theta_{0,1}$, disk inner/outer edges, angular units; τ_0 vertical optical depth to absorption at inner edge; λ_0 , effective grain size; h_0 , scale height at inner edge; η , scale height power law (cf. Eq. 6.2); $\varpi_{0,1}$, inner/outer edges, spatial units; $T(\varpi_0)$, dust temperature at inner edge.

be the same population giving a blue R -[F110W] color, expected for small grains approaching the Rayleigh regime (Kalas 2005). We note that Rayleigh grains scatter light quasi-isotropically, in the sense that the first moment of the scattering phase function ($g \equiv \langle \cos \theta \rangle$) is zero. For an edge-on, wedge-shaped disk ($\eta = 1$) of a power-law distribution of isotropic scatterers, the midplane surface brightness profile at projected distance b is $\propto b^{\gamma-1}$. Under these assumptions, Model I predicts a brightness profile power law index of ~ -1 , which is shallower than the measured indices (-2.7 to -3.7; Schneider et al. 2005; Kalas 2005). This suggests that the long-wavelength SED is not produced by a relatively flat distribution out to large radii, but rather by a separate population of grains. Similar populations have been invoked for other systems (e.g. in β Pic and AU Mic; Backman et al. 1992; Fitzgerald et al. 2007a).

The large spatial extent of Model I and its inconsistency with the scattered light profile power law suggest that we amend the model with an additional grain population. One possibility would be to maintain a distribution of small grains, similar to Model I, to produce the N' -band image and $25 \mu\text{m}$ flux, and add larger, cooler grains that reproduce the $60 \mu\text{m}$ flux but contribute little to the shorter-wavelength emission. This would require additional parameters; modeling a single ring of large grains requires the ring distance and the grains' size and number. In the interest of computational simplicity, we choose not to explicitly parameterize the larger grains in Model II. Instead, we implicitly allow for this population by relaxing the SED fit, requiring only that the $60 \mu\text{m}$ flux from the grain population producing the spatially resolved emission does not exceed the *IRAS* measurement. The unmodeled population is presumed to supplement the small grain emission to match the observed $60 \mu\text{m}$ flux. The larger grains are assumed to emit little at $25 \mu\text{m}$. In effect, we treat the $60 \mu\text{m}$ detection as an upper limit.

After running the MCMC chains with the same procedure as before, we find that Model II reproduces the N' -band image and the $25 \mu\text{m}$ flux. With the parameters that maximize the posterior, the χ^2 for the image is 902, while the χ^2 for the *IRAS* SED is 0.4 (with 1 data point and 3 upper limits). One drawback to our decision to avoid explicitly parameterizing the large grains in this model is that it precludes

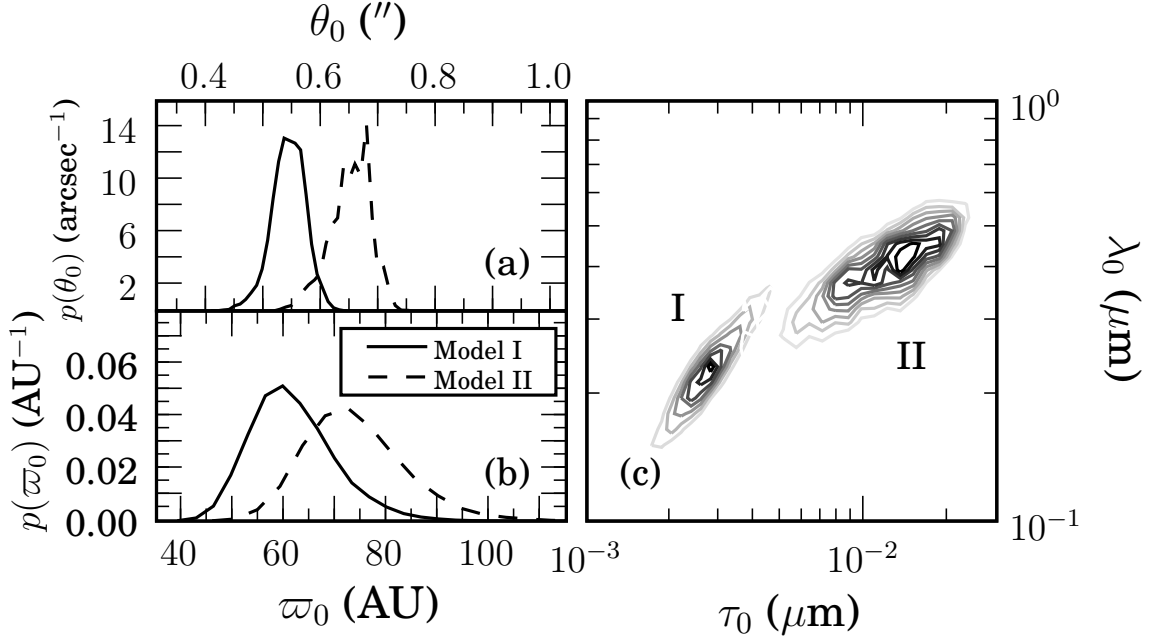


Figure 6.4 Marginal posterior distributions of a subset of model parameters. Panels (a) and (b) give the probability density of location of the inner disk edge in angular (θ_0) and physical (ϖ_0) units, respectively. The ordinates of these plots are matched assuming a distance of 112 pc, and the differences evident between the distributions highlights the value of the joint estimation of all parameters. Panel (c) shows the joint marginal posterior distribution for effective grain size λ_0 and vertical optical depth to absorption at the inner edge τ_0 .

rigorous comparison of the goodness-of-fit to Model I.² However, we expect that when combined with scattered-light data, this model will be favored because of its ability to include surface density gradients with $\gamma < 0$.

Model II produces less stringent requirements on γ than from Model I, favoring steeper dropoff, though flat distributions are not excluded. The distributions of the inner radii, in terms of both angular (θ_0) and physical (ϖ_0) variables, are given in Figures 6.4a and 6.4b.

To give a basic example of possible parameters for the unmodeled large grain

²This is usually done by comparing the “evidence” for each model, through the ratio $\int p(\mathcal{D}, \Theta_{\text{I}} | \text{Model I}, I) d\Theta_{\text{I}} / \int p(\mathcal{D}, \Theta_{\text{II}} | \text{Model II}, I) d\Theta_{\text{II}}$, with a possible additional factor representing prior preference for one model over the other (e.g. Sivia 2006, Ch. 4).

component, we added the flux from a single ring of large grains at 80 AU to the best-fit Model II. We found that 10^{29} cm^2 of $\lambda_0 = 85 \mu\text{m}$ grains were able to reproduce to $60 \mu\text{m}$ flux without strongly affecting the $25 \mu\text{m}$ component from the small grains. These large grains have a temperature of 50 K according to Eq. 6.4. These large-grain parameters are only a single sample in a range of possibilities, and we note that they are expected to be strongly covariant without additional observations of the far-IR and sub-mm flux.

In both models, the effective grain size λ_0 and the fiducial optical depth τ_0 are covariant. This is evident in their marginal joint distributions, shown in Figure 6.4c. The relaxation of the far-IR SED requirement allows for a broader range for these parameters in Model II. We stress that joint estimation of parameters is frequently necessary in disk models. For example, in scattered-light modeling of AU Mic, Graham et al. (2007) revealed a strong degeneracy between scattering asymmetry and the surface density power law, which was broken by the independent constraint from polarization measurements.

In principle, the choice of the prior $p(\Theta|I)$ can affect the distributions of parameters given in Table 6.1. A parameter's distribution is sensitive to the prior if it is not dominated by the likelihood term in Eq. 6.6. We explored the sensitivity to choice of prior by comparing the marginal distributions of each parameter with its prior. In general, both Models I & II show similar sensitivity to priors. In each model, the marginal posterior distribution of ξ is roughly Gaussian in shape, however its mean is offset from the mean of the Gaussian prior. In this case, both the likelihood and prior play a significant role in shaping the posterior distribution. The marginal posterior distribution of the distance d is completely dominated by the prior derived from the *Hipparcos* parallax. This is unsurprising, since we did not use a prior for the stellar radius or luminosity that might serve to constrain the distance. The marginal posterior for the outer radius θ_1 largely follows the flat prior (out to $200''$), though it has an inner cutoff set by the likelihood function. Thus the lower limits listed in Table 6.1 are relatively insensitive to the prior. The marginal posterior of γ is well-constrained by the likelihood function in Model I, however in Model II the prior affects the posterior. In the latter model, the distribution shows an upper-limit

cutoff near $\gamma = 0$ and a peak near $\gamma = -2$. However, the distribution is smooth down to the lower cutoff set by the prior at $\gamma = -4$. Therefore the uniform prior for γ plays a role in shaping the posterior distribution in Model II, and the likelihood function is only able to exclude values in the upper end of the range. For all other variables, the likelihood function is sharply peaked compared to the relatively flat priors; therefore their results are insensitive our choice of prior.

6.4 Discussion

The spatial locations and inferred sizes of the thermally emitting grains are largely consistent with the dust seen in scattered light. Schneider et al. (2005) find that the scattered-light disk is symmetric for $0''.5 < \theta < 1''.7$, which overlaps with the symmetric mid-IR emission we measure in §6.3.2. The inner edge of the warm dust ring ($\theta_0 \simeq 0''.5\text{--}0''.7$) corresponds to the outer boundary of the scattered-light brightness asymmetry seen inward of $0''.5$. A comparison of the NE and SW *F110W* surface brightness profiles shows the SW ansa is ~ 2 times brighter than the NE at $0''.5$. Integrating the disk light in each ansa from $\theta > 0''.3$, Schneider et al. find the total NE (SW) emission to be 1.67 ± 0.57 mJy (3.14 ± 0.57 mJy), which corresponds to a NE-SW fractional flux difference of -0.31 ± 0.18 . In comparison to the scattered light, in the N' -band image we do not find an increasing brightness trend for the SW ansa inward of $0''.6$, nor do we find evidence for asymmetry in this region. How can the emission appear asymmetric in scattered light, but symmetric in thermal emission? One possibility is that the grains responsible for the scattered-light asymmetry reside inward of the warm ring. In this case, they must have properties that differ from the majority of grains in the inner disk, which scatter light in the symmetric component. If the asymmetrically distributed grains have a significantly higher albedo or larger average size, they may not be apparent in the thermal emission. Future observations of scattered light at different wavelengths may constrain such changes in grain properties with position. Another possibility is that the asymmetry is produced by a density enhancement at sufficient distance from the star such that its grains do not produce significant N' -band emission relative to

the warm ring.

For $\lambda_0 \simeq 0.1\text{--}0.5\ \mu\text{m}$ and reasonable assumptions on grain composition and size distribution (§6.3.3), we find $a_{\text{min}} \sim \lambda_0/6 \simeq 0.02\text{--}0.1\ \mu\text{m}$. As noted in §6.3.3, in the *R* and *F110W* bands, submicron grains will scatter blue as their sizes approach the Rayleigh regime, consistent with the blue color of dust scattered light inferred by Kalas (2005). This lends support to the contention that the scattered-light images and thermal image presented here are probing similar populations of grains. Simultaneous modeling of the scattered light and thermal emission, deferred for future work, has the potential to strongly constrain grain sizes, locations, and composition for the bulk of the inner disk.

These observations are a stepping stone to understanding the nature of the disk and source of its structure. However, we lack direct evidence for the age of the system, which complicates such analysis. Based on the stellar distance and galactic space motion, Kalas (2005) argues for an age ~ 30 Myr based on the system’s possible association with the Gould Belt or recent star formation in the Taurus-Aurigae association. As we will show in the following calculations, this age indicates that the grains in the inner disk are likely not primordial and must be replenished. In the next subsection, we seek to estimate orders of magnitude for processes governing grain production and removal for the sizes and spatial locations in the innermost disk.

6.4.1 Grain Dynamics

Assuming the radiative coupling efficiency averaged over the stellar spectrum $Q_{\text{rad}} = 2$, a grain density of $2\ \text{g cm}^{-3}$, and $M_* = 1.8 M_{\odot}$, the fiducial radiation pressure blow-out size is $a_{\text{blow}} \sim 3\ \mu\text{m}$ (Burns et al. 1979). In the absence of forces other than radiation and gravity, grains smaller than this size are removed from the system on the free-fall timescale, $\sim 10^4$ yr. At first glance, this would imply that production of submicron grains must be extremely rapid. However, our conversion from λ_0 to the geometric size a_{min} is quite uncertain, and may be too small by a factor of ~ 30 (if the grains are weakly absorbing and have a size distribution steeper than $dn \propto a^{-3.5} da$; Backman et al. 1992). Another possibility, which maintains

consistency with submicron scattered-light grains, is that drag forces can increase the residence time of the grains undergoing ejection. Finally, we note that a_{blow} is not a strict lower limit to the steady-state size distribution. As noted by Burns et al. (1979), very small grains (sizes much less than the peak wavelength of stellar radiation) couple inefficiently to the radiation field, such that $Q_{\text{rad}} \ll 1$ and the radiation force cannot overcome gravity. For such small grains, composition and porosity can play a crucial role in the residence time due to their effects on the optical constants. For example, Grigorieva et al. (2007) show in their Fig. 1 that around an A5V star, silicate grains are blown out regardless of size or porosity. In contrast, the smallest icy grains can remain bound. Compact icy grains have a blow-out size of $3 \mu\text{m}$, whereas a_{blow} for grains with 80% porosity drops to $0.7 \mu\text{m}$. Because of their small Q_{rad} , the radiation pressure on 80% porous, icy grains smaller than $0.05 \mu\text{m}$ is insufficient to overcome gravity. This cutoff size decreases to $\sim 0.02 \mu\text{m}$ for more compact icy grains. We conclude that our model grain sizes may be compatible with the steady-state size distribution arising from radiation pressure. and note that this mechanism provides a natural separation between a population of small ($a \lesssim 0.05 \mu\text{m}$) grains and a population of grains larger than a_{blow} .

Collisions may play a significant role in the lifetimes of grains in the inner disk, as fragments from a catastrophically dispersed grain can be rapidly removed via radiation pressure. For a low-eccentricity disk of single-size particles, the timescale between mutual collisions is $t_{\text{coll}} \sim (\Omega \tau_{\perp}^{\text{geo}})^{-1}$, where Ω is the orbital frequency and $\tau_{\perp}^{\text{geo}}$ is the geometric vertical optical depth. We find $t_{\text{coll}} \sim 6 \times 10^4 (r/60 \text{ AU})^{3/2} (\tau_{\perp}^{\text{geo}}/10^{-3})^{-1} \text{ yr}$. Calculation of this timescale from our models is complicated by the unknown absorption efficiency, as $\tau_{\perp}^{\text{geo}}(\varpi_0) = \tau_0/Q_{\text{abs}}$. We also note that the timescale for *destructive* collisions is likely different from the above t_{coll} , and it must account for the unknown grain size and velocity distributions. The presence of a gas disk can damp relative velocities, increasing the timescale for destructive collisions. These damping forces can also cause grains to settle in the midplane, causing the disk to be very thin in vertical extent (e.g. Garaud et al. 2004). Observations of the disk scale height may constrain the presence of gas and its effect on collisional timescales. Our models in §6.3.3 show that the mid-IR image is consistent with an edge-on, vertically un-

resolved disk. More work is needed in modeling scattered-light images (at higher spatial resolution) to determine if the apparent disk thickness is the result of vertical extent or inclination effects. Alternately, it may be possible to constrain the gas density through modeling of the dust density's radial structure, as has been done for β Pic (Th ebault & Augereau 2005). Regardless, future dynamical models of the inner disk must make a detailed accounting grain-grain collisions.

Drag forces can decrease the periastra of grain orbits, filling the inner disk with material. Assuming circular orbits, the Poynting-Robertson drag timescale at radius r is $t_{\text{PR}} \sim 10^6 (a/1 \mu\text{m}) (\rho/2 \text{ g cm}^{-3}) (r/60 \text{ AU})^2 (Q_{\text{rad}}/2)^{-1} \text{ yr}$. This is significantly longer than $t_{\text{coll}} \lesssim 10^5 \text{ yr}$, suggesting P-R drag is dynamically unimportant for the radii of warm dust emission (though it may allow some mid-IR emitting dust in systems without planets; see Wyatt 2005). The detection of a potentially massive gas disk by Redfield (2007) suggests that gas drag may affect the grains in this system. As noted above, the role of gas drag in the inner disk is difficult to estimate due to our ignorance of the gas disk's density distribution and physical state, and no physical features (such as sharp outer edges of dust rings or midplane settling) currently provide such indications (e.g. Takeuchi & Artymowicz 2001; Besla & Wu 2007).

An interesting physical result from our models are the warm temperatures of the effective grains at the inner rim of the dust annulus [$T(\varpi_0) \simeq 130\text{--}200 \text{ K}$]. At these temperatures, the sublimation of water ice in small grains is efficient ($t_{\text{sub}} \lesssim 1 \text{ yr}$), suggesting no water is present in grains at this distance from the star. However, this process is a strong function of temperature (cf. Eq. 16 of Backman & Paresce 1993), and therefore stellar distance (Eq. 6.4). At a distance of $r = 2\varpi_0$, a $0.2 \mu\text{m}$ water ice grain has $t_{\text{sub}} \sim 1 \text{ Myr}$. This raises the possibility that, rather than being the location of grain creation and outward diffusion, the inner edge of the warm dust disk is the destruction site for icy inspiraling grains. For this to be the case, drag forces must overcome radiation pressure and destructive collisions for a significant population of icy grains.

The inference of the physical processes responsible for the disk structure (and that govern its evolution) are unclear. Direct spectroscopic evidence of the stellar age

is still needed. Furthermore, the spatial distribution of the gas disk is an important direction for future observations. This system is attractive for the direct detection of gas emission, similar to observations of β Pic (Thi et al. 2001; Olofsson et al. 2001; Brandeker et al. 2004). The next modeling steps should combine the available data, including the resolved scattered light, thermal emission, and SED. More detailed calculations can reveal the processes responsible for the disk structure, in a manner similar to that developed for AU Mic by Strubbe & Chiang (2006).

6.4.2 Conclusions

We have (1) spatially resolved the thermal emission from the warm inner disk around HD 32297 in the N' band, (2) found that the stellar SED is inconsistent with the temperature and luminosity of A0; rather, we favor a cooler, less-luminous star, (3) found that the observed N' emission with the stellar PSF subtracted suggests a symmetric, optically thin ring model, (4) modeled the thermal emission (including *IRAS* SED data) with an annulus consisting of a single population of efficiently absorbing, inefficiently radiating grains, (5) determined that a separate population producing the $60\ \mu\text{m}$ emission improves the fit to the SED and the consistency with the scattered light disk, and (6) identified the possibility that ice sublimation may play a significant role in the destruction of grains in the warm inner disk.

Bibliography

- Aime, C., Borgnino, J., Martin, F., Petrov, R., & Ricort, G. 1986, *JOSA*, 3, 1001
- Aime, C. & Soummer, R. 2004, *ApJ*, 612, L85
- Alibert, Y., Mordasini, C., Benz, W., & Winisdoerffer, C. 2005, *A&A*, 434, 343
- Ardila, D. R., Golimowski, D. A., Krist, J. E., Clampin, M., Williams, J. P., Blakeslee, J. P., Ford, H. C., Hartig, G. F., & Illingworth, G. D. 2004, *ApJ*, 617, L147
- Artymowicz, P. 1988, *ApJ*, 335, L79
- Augereau, J. C. & Beust, H. 2006, *A&A*, 455, 987
- Augereau, J. C., Nelson, R. P., Lagrange, A. M., Papaloizou, J. C. B., & Mouillet, D. 2001, *A&A*, 370, 447
- Avila, R., Masciadri, E., Vernin, J., & Sánchez, L. J. 2004, *PASP*, 116, 682
- Backman, D. E. & Paresce, F. 1993, in *Protostars and Planets III*, 1253–1304
- Backman, D. E., Witteborn, F. C., & Gillett, F. C. 1992, *ApJ*, 385, 670
- Barrado y Navascués, D., Stauffer, J. R., Song, I., & Caillault, J.-P. 1999, *ApJ*, 520, L123
- Bauman, B. J., Gavel, D. T., Waltjen, K. E., Freeze, G. J., Hurd, R. L., Gates, E. L., Max, C. E., Olivier, S. S., & Pennington, D. M. 2002, *Proc. SPIE*, 4494, 19
- Besla, G. & Wu, Y. 2007, *ApJ*, 655, 528

- Biller, B. A., Close, L., Lenzen, R., Brandner, W., McCarthy, D. W., Nielsen, E., & Hartung, M. 2004, *Proc. SPIE*, 5490, 389
- Bloemhof, E. E. 2003, *ApJ*, 582, L59
- Bloemhof, E. E., Dekany, R. G., Troy, M., & Oppenheimer, B. R. 2001, *ApJ*, 558, L71
- Boccaletti, A., Labeyrie, A., & Ragazzoni, R. 1998, *A&A*, 338, 106
- Bordé, P. J., Traub, W. A., Kern, B. D., Trauger, J. T., & Kuhnert, A. C. 2006, in Presented at the Society of Photo-Optical Instrumentation Engineers (SPIE) Conference, Vol. 6265, *Space Telescopes and Instrumentation I: Optical, Infrared, and Millimeter*. Edited by Mather, John C.; MacEwen, Howard A.; de Graauw, Mattheus W. M.. *Proceedings of the SPIE*, Volume 6265, pp. 62651C (2006).
- Born, M. & Wolf, E. 1999, *Principles of Optics*, 7th edn. (Cambridge: Cambridge University Press)
- Brandeker, A., Liseau, R., Olofsson, G., & Fridlund, M. 2004, *A&A*, 413, 681
- Bryden, G., Beichman, C. A., Trilling, D. E., Rieke, G. H., Holmes, E. K., Lawler, S. M., Stapelfeldt, K. R., Werner, M. W., Gautier, T. N., Blaylock, M., Gordon, K. D., Stansberry, J. A., & Su, K. Y. L. 2006, *ApJ*, 636, 1098
- Burns, J. A., Lamy, P. L., & Soter, S. 1979, *Icarus*, 40, 1
- Burrows, A., Marley, M., Hubbard, W. B., Lunine, J. I., Guillot, T., Saumon, D., Freedman, R., Sudarsky, D., & Sharp, C. 1997, *ApJ*, 491, 856
- Cagigal, M. P. & Canales, V. F. 2001, *Opt. Eng.*, 40, 2690
- Canales, V. F. & Cagigal, M. P. 1999a, *J. Opt. Soc. Am. A*, 16, 2550
- . 1999b, *Appl. Opt.*, 38, 766
- Cannon, A. J. & Pickering, E. C. 1993, *Henry Draper Catalogue and Extension (Cannon+ 1918-1924; ADC 1989)*

- Carpenter, J. M., Wolf, S., Schreyer, K., Launhardt, R., & Henning, T. 2005, *AJ*, 129, 1049
- Chen, C. H., Li, A., Bohac, C., Kim, K. H., Watson, D. M., van Cleve, J., Houck, J., Stapelfeldt, K., Werner, M. W., Rieke, G., Su, K., Marengo, M., Backman, D., Beichman, C., & Fazio, G. 2007, *ArXiv e-prints*, 705
- Chen, C. H., Patten, B. M., Werner, M. W., Dowell, C. D., Stapelfeldt, K. R., Song, I., Stauffer, J. R., Blaylock, M., Gordon, K. D., & Krause, V. 2005, *ApJ*, 634, 1372
- Chen, C. H., Sargent, B. A., Bohac, C., Kim, K. H., Leibensperger, E., Jura, M., Najita, J., Forrest, W. J., Watson, D. M., Sloan, G. C., & Keller, L. D. 2006, *ApJS*, 166, 351
- Clampin, M. 2005, in *Nearby Resolved Debris Disks*, ed. I. Kamp & M. Meixner, 7–+
- Cohen, M., Walker, R. G., Carter, B., Hammersley, P., Kidger, M., & Noguchi, K. 1999, *AJ*, 117, 1864
- Cutispoto, G., Messina, S., & Rodonò, M. 2003, *A&A*, 400, 659
- Czechowski, A. & Mann, I. 2007, *ApJ*, 660, 1541
- Dainty, J. C. 1974, *MNRAS*, 169, 631
- Dainty, J. C., Hennings, D. R., & Odonnell, K. A. 1981, *J. Opt. Soc. Am. A*, 71, 490
- Dent, W. R. F., Walker, H. J., Holland, W. S., & Greaves, J. S. 2000, *MNRAS*, 314, 702
- Dohnanyi, J. S. 1969, *J. Geophys. Res.*, 74, 2431
- Dominik, C. & Decin, G. 2003, *ApJ*, 598, 626
- Draine, B. T. & Li, A. 2001, *ApJ*, 551, 807

- Elias, J. H., Frogel, J. A., Matthews, K., & Neugebauer, G. 1982, *AJ*, 87, 1029
- Fernández, R., Brandeker, A., & Wu, Y. 2006, *ApJ*, 643, 509
- Fitzgerald, M. P. & Graham, J. R. 2006, *ApJ*, 637, 541
- Fitzgerald, M. P., Kalas, P. G., Duchêne, G., Pinte, C., & Graham, J. R. 2007a, *ApJ* in press
- Fitzgerald, M. P., Kalas, P. G., & Graham, J. R. 2007b, *ApJ* in press
- Fitzpatrick, E. L. 2004, in *ASP Conf. Ser. 309: Astrophysics of Dust*, ed. A. N. Witt, G. C. Clayton, & B. T. Draine, 33–56
- Foo, G., Palacios, D. M., & Swartzlander, Jr., G. A. 2005, *Optics Letters*, 30, 3308
- Ford, E. B. 2005, *AJ*, 129, 1706
- Ford, V. G., Hull, A. B., Shaklan, S. B., Levine, M. B., White, M. L., Lowman, A. E., & Cohen, E. J. 2003, *Proc. SPIE*, 5170, 1
- Fortney, J. J., Marley, M. S., Hubickyj, O., Bodenheimer, P., & Lissauer, J. J. 2005, *Astronomische Nachrichten*, 326, 925
- Fraquelli, D. A., Schultz, A. B., Bushouse, H., Hart, H. M., & Vener, P. 2004, *PASP*, 116, 55
- Fried, D. L. 1966, *JOSA*, 56, 1372
- Garaud, P., Barrière-Fouchet, L., & Lin, D. N. C. 2004, *ApJ*, 603, 292
- Give'On, A., Kasdin, N. J., Vanderbei, R. J., & Avitzour, Y. 2006, *Journal of the Optical Society of America A*, 23, 1063
- Gliese, W. & Jahreiss, H. 1995, *VizieR Online Data Catalog*, 5070, 0
- Goldreich, P., Lithwick, Y., & Sari, R. 2004, *ARA&A*, 42, 549

- Golimowski, D., John Krist, J., Chen, C., Stapelfeldt, K., Ardila, D., Clampin, M., Schneider, G., Silverstone, M., Ford, H., & Illingworth, G. 2007, in Proceedings of the conference In the Spirit of Bernard Lyot: The Direct Detection of Planets and Circumstellar Disks in the 21st Century. June 04 - 08, 2007. University of California, Berkeley, CA, USA. Edited by Paul Kalas., ed. P. Kalas
- Golimowski, D. A., Ardila, D. R., Krist, J. E., Clampin, M., Ford, H. C., Illingworth, G. D., Bartko, F., Benítez, N., Blakeslee, J. P., Bouwens, R. J., Bradley, L. D., Broadhurst, T. J., Brown, R. A., Burrows, C. J., Cheng, E. S., Cross, N. J. G., Demarco, R., Feldman, P. D., Franx, M., Goto, T., Gronwall, C., Hartig, G. F., Holden, B. P., Homeier, N. L., Infante, L., Jee, M. J., Kimble, R. A., Lesser, M. P., Martel, A. R., Mei, S., Menanteau, F., Meurer, G. R., Miley, G. K., Motta, V., Postman, M., Rosati, P., Sirianni, M., Sparks, W. B., Tran, H. D., Tsvetanov, Z. I., White, R. L., Zheng, W., & Zirm, A. W. 2006, *AJ*, 131, 3109
- Golimowski, D. A., Durrance, S. T., & Clampin, M. 1993, *ApJ*, 411, L41
- Goodman, J. W. 1975, *Laser Speckle and Related Phenomena*, ed. J. C. Dainty (Berlin: Springer)
- . 1985, *Statistical Optics* (New York: Wiley)
- . 2005, *Introduction to Fourier Optics* (Englewood, CO: Roberts & Co.)
- Gorlova, N., Rieke, G. H., Muzerolle, J., Stauffer, J. R., Siegler, N., Young, E. T., & Stansberry, J. H. 2006, *ApJ*, 649, 1028
- Graham, J. R., Kalas, P. G., & Matthews, B. C. 2007, *ApJ*, 654, 595
- Greaves, J. S., Holland, W. S., Moriarty-Schieven, G., Jenness, T., Dent, W. R. F., Zuckerman, B., McCarthy, C., Webb, R. A., Butner, H. M., Gear, W. K., & Walker, H. J. 1998, *ApJ*, 506, L133
- Greaves, J. S., Holland, W. S., Wyatt, M. C., Dent, W. R. F., Robson, E. I., Coulson, I. M., Jenness, T., Moriarty-Schieven, G. H., Davis, G. R., Butner, H. M., Gear, W. K., Dominik, C., & Walker, H. J. 2005, *ApJ*, 619, L187

- Greaves, J. S., Wyatt, M. C., Holland, W. S., & Dent, W. R. F. 2004, MNRAS, 351, L54
- Greenberg, R., Hartmann, W. K., Chapman, C. R., & Wacker, J. F. 1978, Icarus, 35, 1
- Grigorieva, A., Artymowicz, P., & Thébault, P. 2007, A&A, 461, 537
- Guyon, O. 2004, ApJ, 615, 562
- . 2005, ApJ, 629, 592
- Guyon, O., Pluzhnik, E. A., Galicher, R., Martinache, F., Ridgway, S. T., & Woodruff, R. A. 2005, ApJ, 622, 744
- Haisch, Jr., K. E., Lada, E. A., & Lada, C. J. 2001, ApJ, 553, L153
- Hartig, G. F., Krist, J. E., Martel, A. R., Ford, H. C., & Illingworth, G. D. 2003, in Presented at the Society of Photo-Optical Instrumentation Engineers (SPIE) Conference, Vol. 4854, Future EUV/UV and Visible Space Astrophysics Missions and Instrumentation. Edited by J. Chris Blades, Oswald H. W. Siegmund. Proceedings of the SPIE, Volume 4854, pp. 532-543 (2003)., ed. J. C. Blades & O. H. W. Siegmund, 532–543
- Hartmann, W. K., Ryder, G., Dones, L., & Grinspoon, D. 2000, The Time-Dependent Intense Bombardment of the Primordial Earth/Moon System (Origin of the earth and moon, edited by R.M. Canup and K. Righter and 69 collaborating authors. Tucson: University of Arizona Press., p.493-512), 493–512
- Harvey, P. M., Smith, B. J., Difrancesco, J., Colome, C., & Low, F. J. 1996, ApJ, 471, 973
- Hauschildt, P. H., Allard, F., & Baron, E. 1999, ApJ, 512, 377
- Heap, S. R., Lindler, D. J., Lanz, T. M., Cornett, R. H., Hubeny, I., Maran, S. P., & Woodgate, B. 2000, ApJ, 539, 435

- Heckmann, O. 1975, AGK 3. Star catalogue of positions and proper motions north of -2.5 deg. declination (Hamburg-Bergedorf: Hamburger Sternwarte, 1975, edited by Dieckvoss, W.)
- Heinrichsen, I., Walker, H. J., & Klaas, U. 1998, MNRAS, 293, L78
- Hernández, J., Briceño, C., Calvet, N., Hartmann, L., Muzerolle, J., & Quintero, A. 2006, ApJ, 652, 472
- Hernández, J., Hartmann, L., Megeath, T., Gutermuth, R., Muzerolle, J., Calvet, N., Vivas, A. K., Briceño, C., Allen, L., Stauffer, J., Young, E., & Fazio, G. 2007, ApJ, 662, 1067
- Hines, D. C., Schneider, G., Metchev, S. A., Mamajek, E. E., Hillenbrand, L. A., Hollenbach, D., Carpenter, J. M., Meyer, M. R., Backman, D. E., Bouwman, J., Henning, T., Kim, J. S., Moro-Martin, A., Najita, J., Silverstone, M. D., Rodmann, J., & Wolf, S. 2007, in Proceedings of the conference In the Spirit of Bernard Lyot: The Direct Detection of Planets and Circumstellar Disks in the 21st Century. June 04 - 08, 2007. University of California, Berkeley, CA, USA. Edited by Paul Kalas., ed. P. Kalas
- Hinkley, S., Oppenheimer, B. R., Soummer, R., Sivaramakrishnan, A., Roberts, Jr., L. C., Kuhn, J., Makidon, R. B., Perrin, M. D., Lloyd, J. P., Kratter, K., & Brenner, D. 2007, ApJ, 654, 633
- Hobbs, L. M. 1974, ApJ, 191, 381
- Høg, E., Fabricius, C., Makarov, V. V., Urban, S., Corbin, T., Wycoff, G., Bastian, U., Schwekendiek, P., & Wicenec, A. 2000, A&A, 355, L27
- Holland, W. S., Greaves, J. S., Dent, W. R. F., Wyatt, M. C., Zuckerman, B., Webb, R. A., McCarthy, C., Coulson, I. M., Robson, E. I., & Gear, W. K. 2003, ApJ, 582, 1141

- Holland, W. S., Greaves, J. S., Zuckerman, B., Webb, R. A., McCarthy, C., Coulson, I. M., Walther, D. M., Dent, W. R. F., Gear, W. K., & Robson, I. 1998, *Nature*, 392, 788
- Holmes, E. K., Butner, H. M., Fajardo-Acosta, S. B., & Rebull, L. M. 2003, *AJ*, 125, 3334
- Housen, K. R. & Holsapple, K. A. 1999, *Icarus*, 142, 21
- Hufnagel, R. E. & Stanley, N. R. 1964, *Journal of the Optical Society of America* (1917-1983), 54, 52
- Ida, S. & Lin, D. N. C. 2005, *Progress of Theoretical Physics Supplement*, 158, 68
- Isobe, S. 1970, *PASJ*, 22, 429
- Jayawardhana, R., Fisher, S., Hartmann, L., Telesco, C., Pina, R., & Fazio, G. 1998, *ApJ*, 503, L79+
- Joy, A. H. & Abt, H. A. 1974, *ApJS*, 28, 1
- Jura, M., Malkan, M., White, R., Telesco, C., Pina, R., & Fisher, R. S. 1998, *ApJ*, 505, 897
- Kalas, P. 2005, *ApJ*, 635, L169
- Kalas, P., Fitzgerald, M. P., & Graham, J. R. 2007, *ApJ*, 661, L85
- Kalas, P., Graham, J. R., & Clampin, M. 2005, *Nature*, 435, 1067
- Kalas, P., Graham, J. R., Clampin, M. C., & Fitzgerald, M. P. 2006, *ApJ*, 637, L57
- Kalas, P. & Jewitt, D. 1995, *AJ*, 110, 794
- Kalas, P., Liu, M. C., & Matthews, B. C. 2004, *Science*, 303, 1990
- Keenan, P. C. 1983, *Bulletin d'Information du Centre de Donnees Stellaires*, 24, 19
- Kenyon, S. J. & Bromley, B. C. 2004, *AJ*, 127, 513

- Kim, J. S., Hines, D. C., Backman, D. E., Hillenbrand, L. A., Meyer, M. R., Rodmann, J., Moro-Martín, A., Carpenter, J. M., Silverstone, M. D., Bouwman, J., Mamajek, E. E., Wolf, S., Malhotra, R., Pascucci, I., Najita, J., Padgett, D. L., Henning, T., Brooke, T. Y., Cohen, M., Strom, S. E., Stobie, E. B., Engelbracht, C. W., Gordon, K. D., Misselt, K., Morrison, J. E., Muzerolle, J., & Su, K. Y. L. 2005, *ApJ*, 632, 659
- King, I. R. 1971, *PASP*, 83, 199
- Koerner, D. W., Ressler, M. E., Werner, M. W., & Backman, D. E. 1998, *ApJ*, 503, L83+
- Koerner, D. W., Sargent, A. I., & Ostroff, N. A. 2001, *ApJ*, 560, L181
- Krauss, O. & Wurm, G. 2005, *ApJ*, 630, 1088
- Krisciunas, K., Sinton, W., Tholen, K., Tokunaga, A., Golisch, W., Griep, D., Kaminski, C., Impey, C., & Christian, C. 1987, *PASP*, 99, 887
- Krist, J. E. 2004, *Proc. SPIE*, 5487, 1284
- Krist, J. E., Ardila, D. R., Golimowski, D. A., Clampin, M., Ford, H. C., Illingworth, G. D., Hartig, G. F., Bartko, F., Benítez, N., Blakeslee, J. P., Bouwens, R. J., Bradley, L. D., Broadhurst, T. J., Brown, R. A., Burrows, C. J., Cheng, E. S., Cross, N. J. G., Demarco, R., Feldman, P. D., Franx, M., Goto, T., Gronwall, C., Holden, B., Homeier, N., Infante, L., Kimble, R. A., Lesser, M. P., Martel, A. R., Mei, S., Menanteau, F., Meurer, G. R., Miley, G. K., Motta, V., Postman, M., Rosati, P., Sirianni, M., Sparks, W. B., Tran, H. D., Tsvetanov, Z. I., White, R. L., & Zheng, W. 2005, *AJ*, 129, 1008
- Krist, J. E. & Hook, R. 2004, *The Tiny Tim User's Guide, Version 6.3* (Baltimore: STScI)
- Krivova, N. A., Krivov, A. V., & Mann, I. 2000, *ApJ*, 539, 424
- Kuchner, M. J. & Holman, M. J. 2003, *ApJ*, 588, 1110

- Labeyrie, A. 1970, *A&A*, 6, 85
- . 1995, *A&A*, 298, 544
- Lafrenière, D., Marois, C., Doyon, R., Nadeau, D., & Artigau, É. 2007a, *ApJ*, 660, 770
- Lafrenière, D., Doyon, R., Nadeau, D., Artigau, É., Marois, C., & Beaulieu, M. 2007b, *ApJ*, 661, 1208
- Lagrange, A.-M., Beust, H., Mouillet, D., Deleuil, M., Feldman, P. D., Ferlet, R., Hobbs, L., Lecavelier Des Etangs, A., Lissauer, J. J., McGrath, M. A., McPhate, J. B., Spyromilio, J., Tobin, W., & Vidal-Madjar, A. 1998, *A&A*, 330, 1091
- Lallement, R., Welsh, B. Y., Vergely, J. L., Crifo, F., & Sfeir, D. 2003, *A&A*, 411, 447
- Lamzin, S. A. 2000a, *Astronomy Letters*, 26, 589
- . 2000b, *Astronomy Reports*, 44, 323
- Leach, R. W. & Low, F. J. 2000, *Proc. SPIE*, 4008, 337
- Lecavelier Des Etangs, A., Vidal-Madjar, A., & Ferlet, R. 1996, *A&A*, 307, 542
- Lenzen, R., Close, L., Brandner, W., Biller, B., & Hartung, M. 2004, *Proc. SPIE*, 5492, 970
- Lestrade, J.-F., Wyatt, M. C., Bertoldi, F., Dent, W. R. F., & Menten, K. M. 2006, *A&A*, 460, 733
- Li, A. & Greenberg, J. M. 1998, *A&A*, 331, 291
- Lien, D. J. 1990, *ApJ*, 355, 680
- Linsky, J. L., Bornmann, P. L., Carpenter, K. G., Hege, E. K., Wing, R. F., Giampapa, M. S., & Worden, S. P. 1982, *ApJ*, 260, 670
- Liou, J.-C. & Zook, H. A. 1999, *AJ*, 118, 580

- Liseau, R., Brandeker, A., Fridlund, M., Olofsson, G., Takeuchi, T., & Artymowicz, P. 2003, *A&A*, 402, 183
- Liu, M. C. 2004, *Science*, 305, 1442
- Liu, M. C., Matthews, B. C., Williams, J. P., & Kalas, P. G. 2004, *ApJ*, 608, 526
- Lloyd, J. P., Liu, M. C., Macintosh, B. A., Sevenson, S. A., Deich, W. T., & Graham, J. R. 2000, *Proc. SPIE*, 4008, 814
- Lloyd, J. P. & Sivaramakrishnan, A. 2005, *ApJ*, 621, 1153
- Loredo, T. 1992, in *Statistical Challenges in Modern Astronomy*. Springer-Verlag., ed. E. Feigelson & G. Babu
- Low, F. J., Smith, P. S., Werner, M., Chen, C., Krause, V., Jura, M., & Hines, D. C. 2005, *ApJ*, 631, 1170
- Lyot, B. 1939, *MNRAS*, 99, 580
- Macintosh, B., Graham, J., Palmer, D., Doyon, R., Gavel, D., Larkin, J., Oppenheimer, B., Saddlemyer, L., Wallace, J. K., Bauman, B., Evans, J., Erikson, D., Morzinski, K., Phillion, D., Poyneer, L., Sivaramakrishnan, A., Soummer, R., Thibault, S., & Veran, J.-P. 2006, *Proc. SPIE*, 6272
- Macintosh, B. A., Bauman, B., Wilhelmsen Evans, J., Graham, J. R., Lockwood, C., Poyneer, L., Dillon, D., Gavel, D. T., Green, J. J., Lloyd, J. P., Makidon, R. B., Olivier, S., Palmer, D., Perrin, M. D., Sevenson, S., Sheinis, A. I., Sivaramakrishnan, A., Sommargren, G., Soummer, R., Troy, M., Wallace, J. K., & Wishnow, E. 2004, *Proc. SPIE*, 5490, 359
- Mansuripur, M. 2002, *Classical Optics and its Applications* (Cambridge: Cambridge University Press)
- Marcy, G., Butler, R. P., Fischer, D., Vogt, S., Wright, J. T., Tinney, C. G., & Jones, H. R. A. 2005, *PThPS*, 158, 24

- Marengo, M., Backman, D., Megeath, T., Fazio, G., Wilner, D., Stapelfeld, K., Werner, M., Su, K., Rieke, G., & Jura, M. 2005, in *Protostars and Planets V*, 8566–+
- Marley, M. S., Fortney, J. J., Hubickyj, O., Bodenheimer, P., & Lissauer, J. J. 2007, *ApJ*, 655, 541
- Marois, C., Doyon, R., Nadeau, D., Racine, R., Riopel, M., Vallée, P., & Lafrenière, D. 2005, *PASP*, 117, 745
- Marois, C., Doyon, R., Racine, R., & Nadeau, D. 2000, *PASP*, 112, 91
- Marois, C., Lafrenière, D., Doyon, R., Macintosh, B., & Nadeau, D. 2006, *ApJ*, 641, 556
- Marois, C., Racine, R., Doyon, R., Lafrenière, D., & Nadeau, D. 2004, *ApJ*, 615, L61
- Marsh, K. A., Velusamy, T., Dowell, C. D., Grogan, K., & Beichman, C. A. 2005, *ApJ*, 620, L47
- Masciadri, E., Mundt, R., Henning, T., Alvarez, C., & Barrado y Navascués, D. 2005, *ApJ*, 625, 1004
- Masciadri, E. & Raga, A. 2004, *ApJ*, 611, L137
- Mathioudakis, M. & Doyle, J. G. 1991, *A&A*, 244, 433
- Mathis, J. S. & Whiffen, G. 1989, *ApJ*, 341, 808
- Matthews, B. C., Greaves, J. S., Holland, W. S., Wyatt, M. C., Barlow, M. J., Bastien, P., Beichman, C. A., Biggs, A., Butner, H. M., Dent, W. R. F., Di Francesco, J., Dominik, C., Fissel, L., Friberg, P., Gibb, A. G., Halpern, M., Iverson, R. J., Jayawardhana, R., Jenness, T., Johnstone, D., Kavelaars, J., Marshall, J. L., Phillips, N., Schieven, G., Snellen, I. A. G., Walker, H. J., Ward-Thompson, D., Weferling, B., White, G. J., Yates, J., & Zhu, M. 2007, *ArXiv e-prints*, 707

- Metchev, S. A., Eisner, J. A., Hillenbrand, L. A., & Wolf, S. 2005, *ApJ*, 622, 451
- Meyer, M. R., Backman, D. E., Weinberger, A. J., & Wyatt, M. C. 2007, in *Protostars and Planets V*, ed. B. Reipurth, D. Jewitt, & K. Keil, 573–588
- Meyer, M. R., Hillenbrand, L. A., Backman, D., Beckwith, S., Bouwman, J., Brooke, T., Carpenter, J., Cohen, M., Cortes, S., Crockett, N., Gorti, U., Henning, T., Hines, D., Hollenbach, D., Kim, J. S., Lunine, J., Malhotra, R., Mamajek, E., Metchev, S., Moro-Martín, A., Morris, P., Najita, J., Padgett, D., Pascucci, I., Rodmann, J., Schlingman, W., Silverstone, M., Soderblom, D., Stauffer, J., Stobie, E., Strom, S., Watson, D., Weidenschilling, S., Wolf, S., & Young, E. 2006, *PASP*, 118, 1690
- Moerchen, M. M., Telesco, C. M., Packham, C., & Kehoe, T. J. J. 2007a, *ApJ*, 655, L109
- Moerchen, M. M., Telesco, C. M., De Buizer, J. M., Packham, C., & Radomski, J. T. 2007b, *ApJL* in press
- Moffat, A. F. J. 1969, *A&A*, 3, 455
- Monroe, T., Pilachowski, C. A., & Grady, C. 2007, in *American Astronomical Society Meeting Abstracts*, Vol. 210, American Astronomical Society Meeting Abstracts, 75.07–+
- Moór, A., Ábrahám, P., Derekas, A., Kiss, C., Kiss, L. L., Apai, D., Grady, C., & Henning, T. 2006, *ApJ*, 644, 525
- Moro-Martín, A. & Malhotra, R. 2005, *ApJ*, 633, 1150
- Moro-Martín, A., Wolf, S., & Malhotra, R. 2005, *ApJ*, 621, 1079
- Mouillet, D., Lagrange, A.-M., Beuzit, J.-L., & Renaud, N. 1997, *A&A*, 324, 1083
- Murray-Clay, R. A. & Chiang, E. I. 2005, *ApJ*, 619, 623
- Neuhäuser, R., Guenther, E. W., Alves, J., Huélamo, N., Ott, T., & Eckart, A. 2003, *Astronomische Nachrichten*, 324, 535

- O'Brien, D. P. & Greenberg, R. 2003, *Icarus*, 164, 334
- Obukhov, A. M. 1949, *Izv. Akad. Nauk. SSSR, Ser. Geogr. Geofiz.*, 13, 59
- Okamoto, Y. K., Kataza, H., Honda, M., Yamashita, T., Onaka, T., Watanabe, J.-i., Miyata, T., Sako, S., Fujiyoshi, T., & Sakon, I. 2004, *Nature*, 431, 660
- Olofsson, G., Liseau, R., & Brandeker, A. 2001, *ApJ*, 563, L77
- Ozernoy, L. M., Gorkavyi, N. N., Mather, J. C., & Taidakova, T. A. 2000, *ApJ*, 537, L147
- Pan, M. & Sari, R. 2005, *Icarus*, 173, 342
- Pantin, E., Lagage, P. O., & Artymowicz, P. 1997, *A&A*, 327, 1123
- Perrin, M. D., Sivaramakrishnan, A., Makidon, R. B., Oppenheimer, B. R., & Graham, J. R. 2003, *ApJ*, 596, 702
- Perryman, M. A. C., Lindegren, L., Kovalevsky, J., Hoeg, E., Bastian, U., Bernacca, P. L., Cr ez e, M., Donati, F., Grenon, M., van Leeuwen, F., van der Marel, H., Mignard, F., Murray, C. A., Le Poole, R. S., Schrijver, H., Turon, C., Arenou, F., Froeschl e, M., & Petersen, C. S. 1997, *A&A*, 323, L49
- Persson, S. E., Murphy, D. C., Krzeminski, W., Roth, M., & Rieke, M. J. 1998, *AJ*, 116, 2475
- Pinte, C., M enard, F., Duch ene, G., & Bastien, P. 2006, *A&A*, 459, 797
- Plavchan, P., Jura, M., & Lipsky, S. J. 2005, *ApJ*, 631, 1161
- Pollack, J. B., Hubickyj, O., Bodenheimer, P., Lissauer, J. J., Podolak, M., & Greenzweig, Y. 1996, *Icarus*, 124, 62
- Quillen, A. C. 2006, *MNRAS*, 372, L14
- Racine, R. 1996, *PASP*, 108, 372

- Racine, R., Walker, G. A. H., Nadeau, D., Doyon, R., & Marois, C. 1999, *PASP*, 111, 587
- Redfield, S. 2007, *ApJ*, 656, L97
- Roberge, A., Weinberger, A. J., Redfield, S., & Feldman, P. D. 2005, *ApJ*, 626, L105
- Robinson, R. D., Linsky, J. L., Woodgate, B. E., & Timothy, J. G. 2001, *ApJ*, 554, 368
- Roddier, F. 1981, *Prog. Optics*, 19, 281
- Roddier, F., Gilli, J. M., & Lund, G. 1982, *JOpt*, 13, 263
- Roques, F., Scholl, H., Sicardy, B., & Smith, B. A. 1994, *Icarus*, 108, 37
- Rouan, D., Riaud, P., Boccaletti, A., Clénet, Y., & Labeyrie, A. 2000, *PASP*, 112, 1479
- Scaddan, R. J. & Walker, J. G. 1978, *Appl. Opt.*, 17, 3779
- Schneider, G., Silverstone, M. D., & Hines, D. C. 2005, *ApJ*, 629, L117
- Schneider, G., Silverstone, M. D., Hines, D. C., Augereau, J.-C., Pinte, C., Ménard, F., Krist, J., Clampin, M., Grady, C., Golimowski, D., Ardila, D., Henning, T., Wolf, S., & Rodmann, J. 2006, *ApJ*, 650, 414
- Schneider, G., Smith, B. A., Becklin, E. E., Koerner, D. W., Meier, R., Hines, D. C., Lowrance, P. J., Terrile, R. J., Thompson, R. I., & Rieke, M. 1999, *ApJ*, 513, L127
- Sheehy, C. D., McCrady, N., & Graham, J. R. 2006, *ApJ*, 647, 1517
- Shvonski, A. J., Monroe, T., & Pilachowski, C. A. 2006, in *Bulletin of the American Astronomical Society*, Vol. 38, *Bulletin of the American Astronomical Society*, 914–+
- Sicilia-Aguilar, A., Hartmann, L., Calvet, N., Megeath, S. T., Muzerolle, J., Allen, L., D'Alessio, P., Merín, B., Stauffer, J., Young, E., & Lada, C. 2006, *ApJ*, 638, 897

- Siegler, N., Muzerolle, J., Young, E. T., Rieke, G. H., Mamajek, E. E., Trilling, D. E., Gorlova, N., & Su, K. Y. L. 2007, *ApJ*, 654, 580
- Silverstone, M. D. 2000, PhD thesis, Univ. California, Los Angeles
- Sivaramakrishnan, A., Koresko, C. D., Makidon, R. B., Berkefeld, T., & Kuchner, M. J. 2001, *ApJ*, 552, 397
- Sivaramakrishnan, A., Lloyd, J. P., Hodge, P. E., & Macintosh, B. A. 2002, *ApJ*, 581, L59
- Sivia, D. S. 2006, *Data Analysis: A Bayesian Tutorial*, 2nd edn. (New York: Oxford University Press)
- Skrutskie, M. F., Cutri, R. M., Stiening, R., Weinberg, M. D., Schneider, S., Carpenter, J. M., Beichman, C., Capps, R., Chester, T., Elias, J., Huchra, J., Liebert, J., Lonsdale, C., Monet, D. G., Price, S., Seitzer, P., Jarrett, T., Kirkpatrick, J. D., Gizis, J. E., Howard, E., Evans, T., Fowler, J., Fullmer, L., Hurt, R., Light, R., Kopan, E. L., Marsh, K. A., McCallon, H. L., Tam, R., Van Dyk, S., & Wheelock, S. 2006, *AJ*, 131, 1163
- Song, I., Weinberger, A. J., Becklin, E. E., Zuckerman, B., & Chen, C. 2002, *AJ*, 124, 514
- Soummer, R. 2005, *ApJ*, 618, L161
- Soummer, R. & Aime, C. 2004, *Proc. SPIE*, 5490, 495
- Soummer, R., Ferrari, A., Aime, C., & Jolissaint, L. 2007, *ArXiv e-prints*, 706
- Stapelfeldt, K., Krist, J., Bryden, G., & Chen, C. 2007, in *Proceedings of the conference In the Spirit of Bernard Lyot: The Direct Detection of Planets and Circumstellar Disks in the 21st Century*. June 04 - 08, 2007. University of California, Berkeley, CA, USA. Edited by Paul Kalas., ed. P. Kalas, 47–+
- Stapelfeldt, K. R., Holmes, E. K., Chen, C., Rieke, G. H., Su, K. Y. L., Hines, D. C., Werner, M. W., Beichman, C. A., Jura, M., Padgett, D. L., Stansberry,

- J. A., Bendo, G., Cadien, J., Marengo, M., Thompson, T., Velusamy, T., Backus, C., Blaylock, M., Egami, E., Engelbracht, C. W., Frayer, D. T., Gordon, K. D., Keene, J., Latter, W. B., Megeath, T., Misselt, K., Morrison, J. E., Muzerolle, J., Noriega-Crespo, A., Van Cleve, J., & Young, E. T. 2004, *ApJS*, 154, 458
- Stauffer, J. R., Rebull, L. M., Carpenter, J., Hillenbrand, L., Backman, D., Meyer, M., Kim, J. S., Silverstone, M., Young, E., Hines, D. C., Soderblom, D. R., Mamajek, E., Morris, P., Bouwman, J., & Strom, S. E. 2005, *AJ*, 130, 1834
- Stevenson, D. J. 1982, *Planet. Space Sci.*, 30, 755
- Strubbe, L. E. & Chiang, E. I. 2006, *ApJ*, 648, 652
- Su, K. Y. L., Rieke, G. H., Misselt, K. A., Stansberry, J. A., Moro-Martin, A., Stapelfeldt, K. R., Werner, M. W., Trilling, D. E., Bendo, G. J., Gordon, K. D., Hines, D. C., Wyatt, M. C., Holland, W. S., Marengo, M., Megeath, S. T., & Fazio, G. G. 2005, *ApJ*, 628, 487
- Su, K. Y. L., Rieke, G. H., Stansberry, J. A., Bryden, G., Stapelfeldt, K. R., Trilling, D. E., Muzerolle, J., Beichman, C. A., Moro-Martin, A., Hines, D. C., & Werner, M. W. 2006, *ApJ*, 653, 675
- Sylvester, R. J., Dunkin, S. K., & Barlow, M. J. 2001, *MNRAS*, 327, 133
- Sylvester, R. J., Skinner, C. J., Barlow, M. J., & Mannings, V. 1996, *MNRAS*, 279, 915
- Takeuchi, T. & Artymowicz, P. 2001, *ApJ*, 557, 990
- Tamura, M., Fukagawa, M., Kimura, H., Yamamoto, T., Suto, H., & Abe, L. 2006, *ApJ*, 641, 1172
- Telesco, C. M., Fisher, R. S., Wyatt, M. C., Dermott, S. F., Kehoe, T. J. J., Novotny, S., Mariñas, N., Radomski, J. T., Packham, C., De Buizer, J., & Hayward, T. L. 2005, *Nature*, 433, 133

- Tera, F., Papanastassiou, D. A., & Wasserburg, G. J. 1974, *Earth and Planetary Science Letters*, 22, 1
- Thatte, N., Abuter, R., Tecza, M., Nielsen, E. L., Clarke, F. J., & Close, L. M. 2007, *MNRAS*, 378, 1229
- Thébault, P. & Augereau, J.-C. 2005, *A&A*, 437, 141
- Thi, W. F., Blake, G. A., van Dishoeck, E. F., van Zadelhoff, G. J., Horn, J. M. M., Becklin, E. E., Mannings, V., Sargent, A. I., van den Ancker, M. E., & Natta, A. 2001, *Nature*, 409, 60
- Thommes, E. W. & Lissauer, J. J. 2003, *ApJ*, 597, 566
- Thompson, G. I., Nandy, K., Jamar, C., Monfils, A., Houziaux, L., Carnochan, D. J., & Wilson, R. 1978, *Catalogue of stellar ultraviolet fluxes. A compilation of absolute stellar fluxes measured by the Sky Survey Telescope (S2/68) aboard the ESRO satellite TD-1*
- Torres, C. A. O. & Ferraz Mello, S. 1973, *A&A*, 27, 231
- Trauger, J. T., Hull, T., Stapelfeldt, K., Backman, D., Bagwell, R. B., Brown, R. A., Burrows, A., Burrows, C. J., Ealey, M. A., Ftaclas, C., Heap, S. R., Kasdin, J., Lunine, J. I., Marcy, G. W., Redding, D. C., Traub, W. A., Woodgate, B. E., Sahai, R., & Spergel, D. 2003, *Proc. SPIE*, 4854, 116
- Véran, J.-P., Rigaut, F., Maître, H., & Rouan, D. 1997a, *J. Opt. Soc. Am. A*, 14, 3057
- Véran, J.-P., Rigaut, F. J., Maître, H., & Rouan, D. 1997b, *Proc. SPIE*, 3126, 81
- Valenti, J. A., Fallon, A. A., & Johns-Krull, C. M. 2003, *ApJS*, 147, 305
- van der Blik, N. S., Prusti, T., & Waters, L. B. F. M. 1994, *A&A*, 285, 229
- Vernin, J., Caccia, J.-L., Weigelt, G., & Mueller, M. 1991, *A&A*, 243, 553

- Vidal-Madjar, A., Lagrange-Henri, A.-M., Feldman, P. D., Beust, H., Lissauer, J. J., Deleuil, M., Ferlet, R., Gry, C., Hobbs, L. M., McGrath, M. A., McPhate, J. B., & Moos, H. W. 1994, *A&A*, 290, 245
- Voshchinnikov, N. V., Il'in, V. B., Henning, T., & Dubkova, D. N. 2006, *A&A*, 445, 167
- Voshchinnikov, N. V. & Mathis, J. S. 1999, *ApJ*, 526, 257
- Wahhaj, Z., Koerner, D. W., Backman, D. E., Werner, M. W., Serabyn, E., Ressler, M. E., & Lis, D. C. 2005, *ApJ*, 618, 385
- Wahhaj, Z., Koerner, D. W., Ressler, M. E., Werner, M. W., Backman, D. E., & Sargent, A. I. 2003, *ApJ*, 584, L27
- Wahhaj, Z., Koerner, D. W., & Sargent, A. I. 2007, *ApJ*, 661, 368
- Weidenschilling, S. J., Spaute, D., Davis, D. R., Marzari, F., & Ohtsuki, K. 1997, *Icarus*, 128, 429
- Weinberger, A. J., Becklin, E. E., & Zuckerman, B. 2003, *ApJ*, 584, L33
- Williams, J. P. & Andrews, S. M. 2006, *ApJ*, 653, 1480
- Williams, J. P., Najita, J., Liu, M. C., Bottinelli, S., Carpenter, J. M., Hillenbrand, L. A., Meyer, M. R., & Soderblom, D. R. 2004, *ApJ*, 604, 414
- Wilner, D. J., Dowell, C. D., Holman, M. J., & Kuchner, M. J. 2003, in *Bulletin of the American Astronomical Society*, Vol. 35, *Bulletin of the American Astronomical Society*, 1415–+
- Wilner, D. J., Holman, M. J., Kuchner, M. J., & Ho, P. T. P. 2002, *ApJ*, 569, L115
- Wyatt, M. C. 2003, *ApJ*, 598, 1321
- . 2005, *A&A*, 433, 1007
- . 2006, *ApJ*, 639, 1153

- Wyatt, M. C. & Dent, W. R. F. 2002, MNRAS, 334, 589
- Wyatt, M. C., Dermott, S. F., Telesco, C. M., Fisher, R. S., Grogan, K., Holmes, E. K., & Piña, R. K. 1999, ApJ, 527, 918
- Wyatt, M. C., Greaves, J. S., Dent, W. R. F., & Coulson, I. M. 2005, ApJ, 620, 492
- Wyatt, M. C., Smith, R., Greaves, J. S., Beichman, C. A., Bryden, G., & Lisse, C. M. 2007a, ApJ, 658, 569
- Wyatt, M. C., Smith, R., Su, K. Y. L., Rieke, G. H., Greaves, J. S., Beichman, C. A., & Bryden, G. 2007b, ApJ, 663, 365
- Wyatt, S. P. & Whipple, F. L. 1950, ApJ, 111, 134
- Zuckerman, B. 2001, ARA&A, 39, 549
- Zuckerman, B. & Becklin, E. E. 1993, ApJ, 414, 793
- Zuckerman, B., Forveille, T., & Kastner, J. H. 1995, Nature, 373, 494
- Zuckerman, B. & Song, I. 2004, ApJ, 603, 738
- Zuckerman, B., Song, I., Bessell, M. S., & Webb, R. A. 2001, ApJ, 562, L87